Constraining the halo mass function and the physical properties of Lyman-alpha emitting galaxies with strong gravitational lensing observations

Elisa Ritondale

München 2019

Constraining the halo mass function and the physical properties of Lyman-alpha emitting galaxies with strong gravitational lensing observations

Elisa Ritondale

Dissertation
an der Fakultät der Physik
der Ludwig–Maximilians–Universität
München

vorgelegt von
Ritondale
aus Napoli (Italien)

München, den 31/05/2019

Erstgutachter: Prof. Dr. Simon White
Zweitgutachter: Prof. Dr. Jochen Weller
Tag der mündlichen Prüfung: 23/07/2019

Contents

List of Figures

List of Tables

Zusammenfassung

In dieser Doktorarbeit verwenden wir den starken Gravitationslinseneffekt als Mittel um empirische Grenzen für die Werte verschiedener astrophysikalischer Grössen abzuleiten.

Eines der Hauptziele ist es bei der Analyse der BELLS GALLERY (BG), den Vergrösserungseffekt von Gravitationslinsen auszunutzen. Die BG stellt die erste verfügbare Stichprobe von siebzehn Lyman-alpha Quellen (LAEs, abgeleitet vom engl. Lyman-alpha emitters) bei einer Rotverschiebung $2 < z < 3$ bereit, welche von ellitpischen Galaxien (ETGs, abgeleitet vom engl. early-type galaxies) mit einer Rotverschiebung von $z = 0.5$ über den Linseneffekt abgebildet werden. Diese Analyse ist insbesondere im Kontext von Untersuchungen der kosmischen Reionisierung relevant. LAEs sind besonders selten im lokalen Universum, sie stellen aber die Mehrheit der Stern-bildenden Populationen bei einer $z > 5$ Rotverschiebung von dar. Gegeben der grossen Menge von ionisierenden Photonen, welche diese Galaxien emittieren, wird angenommen, dass sie der Grund für die Reionisierung des Universums sind. Unter der Verwendung einer komplett bayesianischen und gitter-basierten Analysetechnik modellieren wir die Massenverteilungen der Gravitationslinsen und rekonstruieren die Oberflaechenhelligkeitsverteilungen der LAEs im UV-Kontinuum, alles unter der Verwendung eines pixellierten Quellen modells. Wir charakterisieren die physikalischen und morphologischen Eigenschaften dieser stark ionisierenden Quellen, indem wir den Vergröesserungseffekt der Gravitationslinsen (typischerweizse $\mu \simeq 20$) ausnutzen. Wir stellen mithilfe der Rekonstruktion der Emmissionen im ultra-violletten Bereich fest, dass mehr als die Haelfte der rekonstruierten LAEs aus mehreren kompakten und diffusen Komponenten im Abstand von 0.4 bis 4 kpc bestehen. Die Sternentstehungsraten der LAEs liegen zwischen 0.3 und 8.5 $M_\odot$ yr^{-1} und ihre Gesamtgrösse is variabel ausgedehnt mit Hauptachsen, welche von 0.2 bis 1.8 kpc (und im Median 561 pc) reichen. Diese Morphologie ist konsistent mit scheibenartigen Strukturen der Sternentstehung für mehr als die haelfte der Stichprobe. Das wichtigste im Bezug auf das erste Hauptziel ist, dass unsere Resultate mit den Ergebnissen von Gravitationslinsen unabhaengigen Studien konsistent sind, jedoch erlaubt der Vergrössungseffekt der Gravitationslinsen bisher unerreichten Zugriff auf die detailierten Strukturen, welche in diesen Quellen präsent sind. Das zweite Hauptziel dieser Arbeit ist die Erforschung der Natur der Dunklen Materie. Im speziellen verwenden wir eine Stichprobe von 17 Systemen aus Gravitationslinsen um die Menge von Dunkle Materie Halos am unteren Ende der Massenverteilung zu bestimmen. Hier betrachten wir Halos, die sich in der Linsengalaxie und entlang der Sichtline befinden. Wir fordern eine Evidenzveränderung von $\Delta \log$ Evidenz = 50 als Detektionskriterium (etwa 10σ, wenn approximiert durch eine Normalverteilung) und berichten darauf basierend keine signifikante Detek-

tion. Wir erstellen eine Karte, welche die niedriegste detektierbare Masse in jedem Pixel in der Linsenebene angibt unter Einbezug der genannten Detektionsgrenze. Mithilfe dieser Sensitivitaetsfunktion berechnen wir die vorhergesagte Anzahl von detektierbaren haloes entlang der Sichtline unter der Annahme von kalter dunkler Materie (CDM, abgeleitet vom engl. cold dark matter). Wir erhalten $\mu_l = 1.17 \pm 1.08$, was in Einklang mit unserer Nicht-Detektion von Halos ist. Unter der Annahme einer hoeheren Sensitivitaet, welche eine Detektionsgrenze von $\Delta \log$ Evidenz = 12 (etwa 5σ) ermöglicht, steigt der Erwartungswert von detektierbaren Haloes entlang der Sichtlinie auf $\mu_l^{5\sigma} = 9.0 \pm 3.0$. Aufgrund der derzeitigen Datengrundlage finden wir keine Detektionen auf dem Level dieser Sensitivität, was eine Wahrscheinlichkeit des CDM modells von $P_{\rm CDM}^{5\sigma}(n_{\rm det} = 0)$=0.0001 implizieren würde. Eine solch niedriges Detektionslimit führt jedoch zu vielen falschen Nicht-Detektionen and aus diesem Grund is das Fehlen von Detektionen unzuverlässig und Bedarf einer erhöhten Sensitivität der daten, um entweder bestätigt oder widerlegt zu werden. Wenn wir die BG Stichprobe mit einer Teilauswahl von 11 Gravitationslinsen des SLACS katalogs kombinieren, können wir die parameter eines vorher angenommenen dunkle materie modells, welchem sterile Neutrinos zugrunde liegen, eingrenzen. Wir bestimmen eine Obergrenze der Halbmoden-Masse von $\log(M_{\rm hm}) < 12.26$ auf dem 2σ Level. Dies ist konsistent mit resonant produzierten sterilen neutrinos, welche Massen$m_s < 0.8$ keV besitzen, und gilt fuer beliebige werte der Leptonen asymmetrie auf dem 2-σ level. Diese Grenzen sind schwaecher als bei anderen astrophysikalischen Untersuchungen, wie zum beispiel dem Zaehlen von Satelliten in der Milchstrasse und Analysen des Lyman-alpha Waldes, jedoch stellen sie robustere Grenzen dar, insofern sie nicht von (manchmal nur schwach eingegrenzten) baryonischen Prozessen beeinflusst werden. Zuletzt praesentieren wir neue empirische Befunde dafuer, dass Linsengalaxien durch komplexe Massenverteilungen charakterisiert werden sollten, welche möglicherweise nicht voll und ganz durch standardmässige nalytische Massenmodelle repräsentiert werden können. Hierzu modellieren wir das Gravitationslinsensystem SDSS J0755+3445 mithilfe von verschienden Makromodellen der Massenverteilung mit aufsteigender Komplexität der Modellierung. Ausgehend von der klassischen Annahme eines einzigen elliptischen Profils in der Form eines Potenzgesetzes, zeigen wir, dass dieses zu einer guten Beschreibung der durch die Linse abgebildeten Emissionen, aber gleichzeitig auch zu einer intrinsischen Quellenstruktur führt, welche teilweise unfokusiert ist und einen ausgedehnten "Tail" mit positiven und negativen Ausschlägen besitzt. Eine geringe erweiterung der komplexität durch ein doppeltes Potenz-gesetz verbessert die rekonstruktion nur marginal. Die Analyse mit einer pixellierten form des Gravitationspotentials enthüllt die Preasenz einer diffusen Massenstruktur auf einem geringen Evidenzlevel, welche - wenn berücksichtigt - zu einer fokusierten rekonstruktion der Quelle führt. Wir schlussfolgern, dass es diese diffuse Massenstruktur ist, welche für die falschen Detektionen von dunkle materie Substrukturen verantwortlich ist, auch wenn diese eine starke statistische Evidenz besitzen. Desweiteren finden wir, dass diese Struktur zu einer Veränderung der geschätzten morphologischen und physikalischen Eigenschaften der rekonstruierten Quellen führt, darunter Veränderungen der Grösse und des geschätzten Strahlungsflusses um bis zu 20 Prozent. Unsere Ergebnisse demonstrieren wie dunkle materie halos in der Linsengalaxie und entlang der Sichtlinie möglicherweise nicht die einzigen Quellen von Anomalien im Strahlungsfluss oder in der Astrometrie bei Beobachtungen von Quasaren über Gravitationslinsen darstellen, und dass andere Formen der Komplexität explizit getested werden sollten. Wir

schliessen daraus, dass ein gutes Verständnis der wahren Massenverteilung einer Linsengalaxie bei der Modellierung fundamental ist, sowohl für eine zuverlässige Inferenz der Menge von dunkler materie in (sub)strukturen, als auch bei der Bestimmung von physikalischen Eigenschaften der abgebildeten Hintergrundquelle.

Abstract

In this thesis, we use strong gravitational lensing as a tool to derive constraints on different astrophysical quantities. One of the main goal is making use of the magnification provided by lensing to study the first available sample of seventeen Lyman-alpha emitters (LAEs) at redshift $2< z <3$ gravitationally lensed by massive early-type galaxies (ETGs) at a mean redshift of 0.5, from the BELLS GALLERY sample. This analysis is particularly relevant in the context of reionisation studies. In fact, LAEs are particularly rare in the local Universe but represent the majority of the star-forming population at redshift $z > 5$. Given the substantial amount of ionising photons that these galaxies emit, they are thought to be responsible for the reionisation of the Universe. Using a fully Bayesian grid-based technique, we model the gravitational lens mass distributions and reconstruct the UV-continuum surface brightness of the LAEs using pixellated source models. Taking advantage of the lensing magnification (typically $\mu \simeq 20$), we characterise the physical and morphological properties of these highly ionising sources. Briefly, from reconstructing the ultra-violet continuum emission, we find that more than half of the reconstructed LAEs are composed of several compact and diffuse components, separated by 0.4 to 4 kpc. Their star-formation rates range from 0.3 to 8.5 $M_\odot$ yr^{-1} and their total size is extended, with major-axis ranging from 0.2 to 1.8 kpc (median 561 pc). This morphology is consistent with disk-like structures of star-formation for more than half of the sample. Most importantly, our inference is consistent with what found by non-lensed studies, but the magnification allows us to access the detailed structure of these sources with unprecedented precision.

Moreover we present new observational evidence that gravitational lens galaxies can be characterised by complex mass distributions, which may not be fully captured by standard analytical assumptions. We model the gravitational lens system SDSS J0755+3445 with different assumptions of increasing complexity on the lensing potential. Starting from the classical assumption of a single elliptical power-law, we show that this leads to a good description of the lensed emission, but results in an intrinsic source structure which is partly unfocused and has an extended tail with a positive and negative beating. A slightly more complicated double power-law model produces only a marginal improvement. A pixellated gravitational imaging analysis reveals the presence of a low-level diffuse mass structure, which also provides a physical and focused source distribution. We find that this diffuse mass structure is responsible for the false detection of dark-matter subhaloes in the form of spherical NFW mass components with strong statistical evidence. Moreover, it causes a change in the estimated morphological and physical properties of the reconstructed source, changing sizes and flux estimates by up to a factor of 22 per cent. Our results demonstrate how subhaloes and line-of-sight haloes may not be the only source of flux-ratio

and astrometric anomalies in gravitationally lensed quasars and galaxies, and that other forms of complexity should be explicitly tested. We conclude that a good knowledge of the lens true mass distribution is fundamental to make reliable inference on the amount of dark matter (sub)structure in lens galaxies, as well as the physical properties of the background sources. The second main goal of this thesis is to investigate the nature of dark matter. In particular, we use our sample of seventeen strong gravitational lens systems to quantify the amount of low-mass dark matter haloes within the lensing galaxies and along their lines of sight. Based on a detection criterion of Δ log Evidence = 50 (i.e. 10σ under the approximation of statistical Gaussian errors), we report no significant detection in any of the lenses. We compute the map of the lowest detectable halo mass in each pixel in the lens plane, adopting the same detection threshold. Using this sensitivity function, we calculate the predicted number of detectable cold dark matter (CDM) line-of-sight haloes to be $\mu_l = 1.17 \pm 1.08$, in agreement with our null detection. Assuming a sensitivity that is improved to the level implied by a Δ log Evidence = 12 (roughly 5σ) detection threshold, the expected number of detectable line-of-sight haloes rises to $\mu_l = 9.0 \pm 3.0$. The current data find zero detections at this sensitivity level, which would imply a probability of the CDM framework of $P^{5\sigma}_{\rm CDM}(n_{\rm det} = 0)$=0.0001. However, we find that such a low detection threshold leads to false negatives in almost almost 40 per cent of the cases and therefore, the current lack of detections is unreliable and requires an improved quality of the data to be confirmed.
Combining the BELLS GALLERY sample with a sample of 11 SLACS lenses, we constrain the parameters of an assumed sterile neutrino dark-matter model. The half-mode mass is constrained to be $\log(M_{\rm hm}) < 12.26$ at the 2-σ level. The latter is consistent with resonantly produced sterile neutrino masses $m_s < 0.8$ keV at any value of the lepton asymmetry at the 2-σ level. These constraints are weaker than the ones derived with other astrophysical probes, such as the count of satellites in the Milky Way and the Lyman-alpha forest, but they are more robust as they are not affected by poorly constrained baryonic processes.

Chapter 1

Introduction

Strong gravitational lensing is a powerful tool with diverse cosmological and astrophysical applications. In recent years, it has been used for many purposes such as studying the baryonic and dark matter distribution in galaxies (e.g. Treu & Koopmans 2002; Kochanek & Dalal 2004; Oldham & Auger 2018) and galaxy clusters (e.g. Postman et al. 2012; Zitrin et al. 2011), investigating the resolved properties of high-redshift galaxies (e.g. Leethochawalit et al. 2016; Patrício et al. 2016; Ritondale et al. 2019a), measuring the Hubble constant (e.g. Suyu et al. 2018), as well as mapping the dark matter distribution on sub-galactic scales (Dalal & Kochanek 2002a; Vegetti et al. 2010b, 2012, 2014; Nierenberg et al. 2014; Hezaveh et al. 2016; Vegetti et al. 2018; Hsueh et al. 2019; Ritondale et al. 2019b).
In this thesis, we use the phenomenon of strong gravitational lensing to derive constraints on the nature of dark matter and investigate the morphological and physical properties of a sample of high-redshift Lyman-α emitting galaxies. In the following, we give a brief introduction on the gravitational lensing theory, its regimes and its possible applications.

1.1 Gravitational Lensing

Gravitational lensing is the astrophysical phenomenon occurring when the path that photons emitted by a background source travel across the Universe is bent as a consequence of the curvature of spacetime caused by any intervening objects with a non-zero mass. With the advent of General Relativity, Albert Einstein introduced the deflection of photons from straight-line motion in his theory, solving the geodesic for the photon path in the gravitational field of the lens mass. In his treatise "The foundation of the general theory of Relativity" (Einstein 1916) he computed a deflection angle $\hat{\boldsymbol{\alpha}}$ of

$$\hat{\boldsymbol{\alpha}} = \frac{4GM}{\boldsymbol{\xi} c^2}\,, \tag{1.1}$$

where G is the gravitational constant, M the mass of the lens and ξ is the so-called impact parameter, corresponding to the minimum distance of approach between the mass and the photon. Later Einstein computed the exact magnification of a pair of unresolved images produced in the

sky by a foreground stellar object acting on a very distance source (Einstein 1936). His work was pushed further by Zwicky when a year later he proved that the creation of multiple and resolved images of a source was possible if the deflecting object was an intervening galaxy (Zwicky 1937). The intense search for a lensing event following the publication of Zwicky's paper led in 1979 to the first observation of gravitational lensing by Walsh et al. (1979) who observed the multiple images of the "Twin Quasar". The high redshift quasar Q0957+561 is lensed by a foreground galaxy and projected in two images 6.1″ apart, appearing therefore as a black hole binary system. Since its theorisation and discovery, gravitational lensing has proven to be a powerful research tool in many aspects of astrophysics and cosmology, from making possible the discovery of exoplanets to probing the Hubble constant and the rate of expansion of the Universe with the best precision to date. Moreover, as a consequence of lensing, the flux of background objects such as quasars and galaxies is magnified and distorted and appears in multiple images or arcs in the same plane of the sky as the lens. Depending on the mass of the deflector and the relative position of the lens and the source, gravitational lensing is broadly classified into three regimes:

- **Strong lensing**: it occurs when the deflectors are particularly massive, for example, galaxies or clusters of galaxies with masses above 10^{11} $M_{\odot}$. In this case, the flux of the background source is mostly magnified and distorted, and it appears in the sky as arcs or rings, depending on the relative position of the source and the lens and the mass distribution of the latter. In case the source is extended and perfectly aligned with an axisymmetric lens, the light rays can travel through any direction around the lens, and the lensing images appear in the form of a perfect ring, so-called Einstein ring. The radius of this ring is called the Einstein radius R_{ein}, and it is proportional to the square root of the mass that it encloses. Even in the case in which the source is not perfectly aligned with the lens or the latter is not exactly axisymmetric, the source will still be magnified and distorted in images appearing as arcs or double pairs, depending on the focus of the lens system. Strong lensing is widely used to study in detail the matter content of galaxies (Kochanek & Dalal 2004; Auger et al. 2010; Vegetti et al. 2010b, 2012; Bolton et al. 2012; Sonnenfeld et al. 2013; Nierenberg et al. 2014; Hezaveh et al. 2016; Vegetti et al. 2018; Ritondale et al. 2019b; Hsueh et al. 2019) and galaxy clusters (e.g. Zitrin et al. 2011; Postman et al. 2012), investigate the resolved properties of high-redshift galaxies (e.g. Leethochawalit et al. 2016; Patrício et al. 2016; Ritondale et al. 2019a; Spingola et al. 2019), as well as perform high precision measure of the cosmological parameters (e.g. Suyu et al. 2018).

- **Weak lensing**: In this case, the system configuration does not allow for the formation of multiple images and the background sources only appear distorted and elongated. The weakness of this effect makes it impossible to be detected for individual objects, but it can be statistically used to constrain the large scale structure of the Universe as well as the outer mass profile of galaxy clusters and galaxies by stacking a large number of distorted sources (e.g. Bartelmann & Schneider 2001; Hoekstra et al. 2012; Meneghetti et al. 2010; Giocoli et al. 2014).

- **Microlensing**: the effect of microlensing cannot be visually detected because the image distortion is so small that it cannot be resolved. The only way microlensing can be de-

tected is by observing the change in flux of a source over time, i.e. by monitoring its light curve: its variability is a clue of the presence of a lens transiting and magnifying its surface brightness. This lensing regime has frequently been used to detect planets orbiting in front of stars (e.g. Mao & Paczynski 1991; Bond et al. 2004; Nikolaus & Hundertmark 2018).

1.1.1 Strong gravitational lensing and its formalism

Strong gravitational lensing is the physical phenomenon lying at the basis of this thesis, where the images of background galaxies strongly lensed by intervening massive galaxies along their line of sight, are used to study the detailed mass distribution of the deflectors as well as the morphological and physical properties of the background sources.

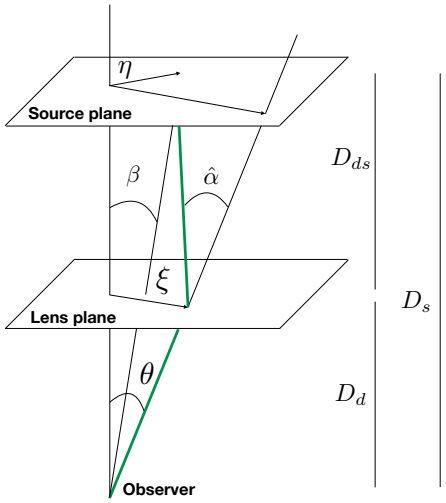

Figure 1.1: Representation of strong lensing in the thin lens approximation. The path travelled by the photons emitted by the background source follows the green line.

A typical strong lensing configuration is shown in Figure 1.1, where it can be seen that due to the presence of the deflector, the light coming from the source arrives to the observer as if it was emitted at the angular position $\boldsymbol{\theta}$. The optical axis is defined to be perpendicular to the lens and source planes and passing through the observer. Then, under the small angle approximation, which allows one to write a physical size as an angular size times the distance, one can write the positions with respect to the optical axis in the lens and source planes $\boldsymbol{\xi}$ and $\boldsymbol{\eta}$ as a function of the respective angular coordinates $\boldsymbol{\theta}$ and $\boldsymbol{\beta}$ as

$$\boldsymbol{\xi} = D_l\boldsymbol{\theta}, \boldsymbol{\eta} = D_s\boldsymbol{\beta}\,, \tag{1.2}$$

where D_l and D_s are the angular diameter distances from the observer to the lens and to the source, respectively. Observing the configuration in Figure 1.1 it is easy to write the following

relation between the positions in the source and in the lens plane, the so-called *lens equation*

$$\boldsymbol{\eta} = \frac{D_s}{D_l}\boldsymbol{\xi} - D_{ls}\hat{\boldsymbol{\alpha}}(\boldsymbol{\xi})\,, \tag{1.3}$$

where D_{ls} is the angular diameter distance between the lens and the source. By substituting the conversion in angular coordinates in equation (1.2), one can re-write equation (1.3) as follows

$$\boldsymbol{\beta} = \boldsymbol{\theta} - \boldsymbol{\alpha}(\boldsymbol{\theta})\,, \tag{1.4}$$

where the scaled deflection angle $\boldsymbol{\alpha}(\boldsymbol{\theta})$ is given by

$$\boldsymbol{\alpha}(\boldsymbol{\theta}) = \frac{D_{ls}}{D_s}\hat{\boldsymbol{\alpha}}(D_l\boldsymbol{\theta})\,. \tag{1.5}$$

Let us consider a general gravitational field originated by an extended mass distribution with mass density $\rho(\boldsymbol{\xi})$. For a light ray passing through it with spacial trajectory (ξ_1, ξ_2, z) the formula for the deflection angle in equation (1.1) will become:

$$\hat{\boldsymbol{\alpha}}(\boldsymbol{\xi}) = \frac{4G}{c^2}\int d^2\xi' \int dz'\rho(\xi_1', \xi_2', z')\frac{\boldsymbol{\xi} - \boldsymbol{\xi}'}{|\boldsymbol{\xi} - \boldsymbol{\xi}'|^2}\,. \tag{1.6}$$

Assuming that the thickness of the mass distribution causing the lensing is negligible with respect to the angular diameter distances between the lens and the source and the observer and the lens, one can apply the so-called *thin lens approximation*, and equation (1.6) can be re-written as

$$\hat{\boldsymbol{\alpha}}(\boldsymbol{\xi}) = \frac{4G}{c^2}\int d^2\xi'\Sigma(\xi_1', \xi_2')\frac{\boldsymbol{\xi} - \boldsymbol{\xi}'}{|\boldsymbol{\xi} - \boldsymbol{\xi}'|^2}\,. \tag{1.7}$$

$\Sigma(\xi_1', \xi_2')$ is the projected surface mass density of the deflector as a function of the two-dimensional position on the lens plane (ξ_1', ξ_2'), and it is defined as

$$\Sigma(\xi_1', \xi_2') \equiv \int dz'\rho(\xi_1', \xi_2', z')\,. \tag{1.8}$$

Using equation (1.5), one can re-write the scaled deflection angle $\boldsymbol{\alpha}(\boldsymbol{\theta})$ as

$$\boldsymbol{\alpha}(\boldsymbol{\theta}) = \frac{1}{\pi}\int d^2\theta'\kappa(\boldsymbol{\theta}')\frac{\boldsymbol{\theta} - \boldsymbol{\theta}'}{|\boldsymbol{\theta} - \boldsymbol{\theta}'|^2}. \tag{1.9}$$

where $\kappa(\boldsymbol{\theta})$ is the projected dimensionless surface mass density also called convergence, given by

$$\kappa(\boldsymbol{\theta}) = \frac{\Sigma\,(D_l\boldsymbol{\theta})}{\Sigma_{cr}} \tag{1.10}$$

with

$$\Sigma_{cr} = \frac{c^2}{4\pi G}\frac{D_s}{D_l D_{ls}}\,. \tag{1.11}$$

The latter is the critical surface mass density of the lens, a quantity which characterises a specific lens system and is a function of the angular diameter distances of the lens and the source. Generally, for extended objects the condition $\Sigma\left(D_l\boldsymbol{\theta}\right) > \Sigma_{cr}$ has to hold for some value of θ for strong lensing to occur. Equivalently, the condition $\kappa(\boldsymbol{\theta}) > 1$ needs to be satisfied, and this is also used as a criterion to distinguish between the strong and weak lensing regimes.

Observing that $\nabla ln\left|\boldsymbol{\theta}\right| = \boldsymbol{\theta}/\left|\boldsymbol{\theta}^2\right|$, the scaled deflection angle can be re-written as

$$\boldsymbol{\alpha}(\boldsymbol{\theta}) \equiv \nabla\psi(\boldsymbol{\theta})\,, \tag{1.12}$$

where we have defined the lensing potential ψ as

$$\psi(\boldsymbol{\theta}) = \frac{1}{\pi}\int d^2\theta'\kappa(\boldsymbol{\theta'})ln\left|\boldsymbol{\theta} - \boldsymbol{\theta'}\right| \tag{1.13}$$

and corresponds to the function describing the gravitational potential generated by the presence of the lensing mass and the consequent curvature of spacetime (Schneider 2005). Since in equation (1.12) we have defined the deflection angle as the gradient of the lensing potential, we can also write equation (1.4) in terms of $\nabla\psi(\boldsymbol{\theta})$ and the lensing equation becomes

$$\boldsymbol{\beta} = \boldsymbol{\theta} - \nabla\psi(\boldsymbol{\theta})\,. \tag{1.14}$$

Thus, in this form, it directly links the positions of the images on the lens plane to the first derivative of the lensing potential.

Two of the most interesting characteristics of gravitational lensing are the distortion and the consequent magnification that affect the background source structure. In particular, the distortion occurs because light rays coming from different parts of the source are bent differentially, and this effect is stronger for more extended sources. However, if the dimensions of the source can be considered small compared to the scales at which the mass distribution of the deflector varies, the lensing equation can be locally linearised, and one can describe the distortion as the following Jacobian matrix

$$\mathbf{A}(\boldsymbol{\theta}) = \frac{\partial\boldsymbol{\beta}}{\partial\boldsymbol{\theta}} = \left[\delta_{ij} - \frac{\partial^2\psi\boldsymbol{\theta}}{\partial\theta_i\partial\theta_j}\right], \tag{1.15}$$

where θi corresponds to the i^{th} component of the angular coordinate $\boldsymbol{\theta}$ on the lens plane. Therefore, the Jacobian matrix can be written as the second derivative of the lensing potential and, recalling equation (1.13), it must also be related to the convergence $\kappa(\boldsymbol{\theta})$. Once defined the vector $\boldsymbol{\gamma} = (\gamma_1, \gamma_2)$ as the *shear*, one can show that

$$\mathbf{A}(\boldsymbol{\theta}) = \frac{\partial\boldsymbol{\beta}}{\partial\boldsymbol{\theta}} = \begin{bmatrix} 1-\kappa-\gamma_1 & -\gamma_2 \\ -\gamma_2 & 1-\kappa+\gamma_1 \end{bmatrix}. \tag{1.16}$$

The role played by the convergence and the shear is evident in the last equation: the convergence causes an isotropic distortion of the source structure by a constant value while the shear is responsible of stretching it in preferential directions, and, therefore, elongating its structure.

The *magnification tensor* is given by the inverse of the Jacobian matrix $\mathbf{M} = \mathbf{A}^{-1}$ and the magnification is estimated with

$$\mu = \det(\mathbf{M}) = \frac{1}{\det(\mathbf{A})} = \frac{1}{(1-\kappa)^2 - \gamma^2}\,. \tag{1.17}$$

Since gravitational lensing conserves the surface brightness, the magnification will accordingly re-scale the surface area and the flux of the background source on the lens plane. The positions in the lens plane where μ diverges form the so-called *critical curves* while the corresponding positions on the source planes lie on the *caustic curves*. In particular, the radial and tangential eigenvalues of the magnification define two curves on the lens plane where infinitely magnified images lie, the *tangential* and *radial critical curve*. The closer to the caustic curves a source lies, the more amplified will be its images. This feature provided by gravitational lensing is extremely useful to unveil the high-redshift Universe with a precision that would otherwise be prohibitive. Acting as a natural telescope, lensing allows us to study the detailed morphology and physical properties of high-redshift sources.
In this thesis, we use the magnification to study the detailed surface brightness distribution, the structure and the star formation rate of the first homogeneous sample of lensed Lyman-α emitting galaxies ad redshift z $\sim$ 2.5.

1.2 Lyman-α emitters as a probe of Reionization

An important phase in the history of the Universe is the Epoch of Reionization (from $z \sim 10$ to $z \sim 6$) during which the intergalactic medium evolves from being mainly neutral to completely ionised (e.g. Barkana & Loeb 2001; Ciardi & Ferrara 2005). However, uncertainties related to the nature of the reionising sources, such as for example their numbers, star formation rates and the escape fraction of ionising photons, have hampered a clear understanding of this important epoch and in particular of its final stages (e.g. Xu et al. 2014; Furlanetto & Oh 2016). Lyman alpha photons and, and consequently, Lyman alpha emitting galaxies are believed to play a critical role in the reionising process, as they are characterised by high optical depths to neutral hydrogen. Therefore, constraining the luminosity function, escape fractions and star formation rates of these galaxies, especially at high redshift, is an important ingredient to better understand the Epoch of Reionization (Erb et al. 2016; Nakajima et al. 2018). However, as galaxies become increasingly faint with redshift, many of these sources are too faint to be detected and studied in details. Until the launch of the *James Webb Space Telescope*, which will directly unveil the properties of the high-redshift Universe, the best strategy to study this highly ionising population of galaxies is by focusing on the lower redshift ranges.
At redshift $2 < z < 3$, well-studied LAEs from wide-field surveys are typically at the bright end of this parameter space, being L^* galaxies with $M^* \sim 10^9$ $M_\odot$ and typical SFRs of about a few to 100 $M_\odot$ year^{-1} (e.g. Gawiser et al. 2006; Erb et al. 2014). Investigations of lower-SFR objects have generally been limited to quantifying the properties of strong optical lines (e.g. Trainor et al. 2015, 2016), although deep narrow-band imaging has also uncovered a large population of both low-mass and low SFR LAEs (e.g. Shimakawa et al. 2017). For example, it has been recently

shown that low-SFR LAEs, with similar characteristics to the local-Universe *green peas* (M^* as low as 10^7 $M_\odot$ and SFR of about 1 to 100 $M_\odot$ year^{-1}), have strong optical emission line (Hα and [O III]) properties that are consistent with optically-selected star-forming galaxies of the same stellar masses at $z \sim 2$ (Hagen et al. 2016). However, it is not possible to directly determine the gas metallicity, density, and kinematics of these galaxies without substantial investments in telescope time. Finally, high-resolution imaging studies find that LAEs are typically compact, with no evidence for strong evolution in size with redshift (e.g. Venemans et al. 2005; Malhotra et al. 2012; Paulino-Afonso et al. 2018). Their Lyman-α halo, which is typically more extended than the UV-continuum by a factor of 10 in average, has also been found not to evolve with cosmic time (Leclercq et al. 2017). However, such studies are currently limited by the angular resolution of the observations.
Strong gravitational lensing can be used to overcome these limitations. In practice, however, most of the strongly lensed galaxies at $z \sim 2$ with moderate star formation are not LAEs (e.g. Hainline et al. 2009; Rhoads et al. 2014; Stark et al. 2013), and at present, the properties of only a few lensed LAEs could be investigated in detail (Christensen et al. 2012; Vanzella et al. 2016; Patrício et al. 2016). Recently, new *Hubble Space Telescope* (*HST*) V-band observations of LAE galaxies selected from the Baryon Oscillation Spectroscopic Survey (BOSS) have revealed a sample of strongly lensed systems at $\langle z \rangle \sim 2.5$. Thanks to the lensing magnification we can probe the detailed structure of these galaxies at scales around 100 pc, which are below the native resolution of the telescope (Shu et al. 2016a; Ritondale et al. 2019a). This analysis and the derived results are reported in detail in Chapter 2.

1.3 Dark Matter

The nature of dark matter is one of the most fundamental yet still unsolved problems in modern physics and astrophysics. In the following, we briefly summarise the observational evidence for the presence of dark matter and our current understanding of its properties. We then show how dark matter affects the formation and evolution of structure across cosmic time and how strong gravitational lensing provides a clean and robust probe of the physics of the dark matter particles.

1.3.1 Observational evidence of the presence of dark matter

Over the course of several decades, a considerable amount of evidence for the existence of dark matter has been obtained, and we now know that as much as 75 per cent of the matter content of the Universe is made of this unknown elusive component (Bosma 1981; Rubin et al. 1985; Frenk & White 2012; Planck Collaboration et al. 2018). The idea of dark matter, as a significant amount of non-luminous matter, was first proposed by Zwicky (1933) to explain the orbits of galaxies within the Coma galaxy cluster. Later on, the presence of dark matter was proven to be fundamental to explain the reciprocal approach of the Milky Way and Andromeda, otherwise impossible if their masses would only be equal to their measured stellar mass Kahn & Woltjer (1959), as well as the large velocities of stars and gas observed in the outer disk of M31 (Rubin

et al. 1978). Further observational evidence in favour of dark matter at the scale of galaxies and galaxy clusters was then obtained from strong and weak gravitational lensing observations (e.g. Broadhurst 1995; Clowe et al. 2006; Harvey et al. 2015). At larger scales, the existence of dark matter is manifested in the distribution of structure in the Universe (e.g. Percival et al. 2001; Eisenstein et al. 2005; Frenk & White 2012) and the observed magnitude of the fluctuations in the Cosmic Microwave Background (CMB, Planck Collaboration et al. 2016, 2018).

1.3.2 Dark matter candidates

The particle nature of dark matter has not been constrained yet, but broadly speaking we know from observations of the large scale structure, microlensing surveys, the CMB power-spectrum as well as constraints from big-bang nucleosynthesis that it has to be stable, non-baryonic and non-relativistic (e.g. Davis et al. 1982; White et al. 1983; Fields 2011). It should be noted that none of the particles which are part of the Standard Model satisfies these properties, and that, therefore, new physics is required to explain the dark matter problem. From an astrophysical perspective, dark matter is generally divided into three broad categories, i.e. cold, warm and hot, depending on the free-streaming velocities of the dark matter particles in the early Universe. Below, we summarise the general properties of these three groups, relative observational constraints and possible particle candidates. We stress that dark matter does not have to be uniquely made by one of these three categories and that depending on the production mechanism, mixed models are certainly possible.

Cold Dark Matter

The term cold dark matter refers to a form of dark matter which is collisionless, weakly interacting and has negligible velocities at early times. The emergence of CDM as the favourite dark model mainly stems from the success of CDM N-body simulations in correctly reproducing observations of the Universe large scale structure as progressively unveiled by redshift surveys (e.g. Springel 2005; Planck Collaboration et al. 2017).
From the point of view of particle physics, among the most appealing cold dark matter candidates are weakly interacting massive particles (WIMPs). WIMPs have been initially introduced as an extension of the particle Standard Model, they are thermally produced, have masses ranging from 1 MeV to 100 TeV, negligible thermal velocities at early times and are collisionless at scales smaller than $\sim$ 1 kpc (e.g. Baer et al. 2015; Ringwald 2016). Moreover, they naturally lead to the correct dark matter relic density, the so-called WIMP-miracle. Most importantly, the typical WIMP detection rates are accessible by current detectors, making this model directly and observably testable (Roszkowski et al. 2018). In the last three decades, the experimental search for the cold dark matter particle has seen an intense activity and has significantly improved the knowledge of the properties of WIMPs. A plethora of experiments aims at directly observing the signal from dark matter particles with three main strategies: looking for the production of DM particles in hadron colliders (e.g. Kahlhoefer 2017), the products of its annihilation in overdense regions (e.g. Gaskins 2016) and finally, the elastic scatter off nuclei of DM particles in Earth-based detectors (e.g. Zhang et al. 2019). The first strategy consists in actively producing neutral,

stable particles in large colliders by observing a considerable amount of energy missing in the decay chain of the detected and visible produced particles. In this case, the most advanced experiment is the Large Hydron Collider (LHC, Servant 2015), which however has not detected any signal compatible with WIMPs. The detection of the annihilation of DM instead, focuses on the search for products of dark matter annihilation in over-dense regions, such as, the detection of a gamma-ray excess in the centre of galaxies. These kinds of experiments have been performed by ground-based gamma-ray telescopes such as EGRET (Thompson et al. 1993) and the currently running Fermi-LAT (Atwood et al. 2009). The last category of experiments instead targets the detectable consequences of the scattering, such as scintillation of photons or ionisation of atoms in a test material or monitors the signal in detectors over the course of the year in order to detect any change due to earth travelling through the Galaxy halo. Often, the presence of one effect and the absence of another makes it possible to avoid the confusion of a signal coming from a WIMP with the signal coming from other nuclear activities such as α and β decay and nuclear recoils. Many detectors are currently running their experiments as the DAMA/LIBRA experiment (e.g. Bernabei et al. 2008), which looks for scintillation of photons in crystals to detect a dark matter particle with a mass between 10 and 100 GeV or the CoGeNT, CDMS-Si experiments which look for ionisation in low-temperature germanium detectors (e.g. Ahlen et al. 1987; CDMS Collaboration et al. 2013). However, despite the many efforts in these direct detection experiments, no significant excess above the background signal has been statistically observed, and therefore as of today, WIMPs still remain undetected, and the evidence for the existence of dark matter remains indirect. The lack of WIMP detection has sparked renewed attention in alternative dark matter models as well as alternative theories of gravity.

Warm Dark Matter

Warm dark matter either thermally or non-thermally produced includes classes of particles which have non-negligible, but sub-relativistic, velocities at the epoch of matter-radiation equality. They have masses of a few keV, and they are therefore much lighter than CDM particles. Possible candidates include the gravitino (e.g. Nilles 1984; Steffen 2006) and resonantly produced sterile neutrinos (e.g. Shi & Fuller 1999; Boyarsky et al. 2012).

In particular, resonantly produced sterile neutrinos (SN) have gained increasing attention, following the possible detection of a 3.5 keV line in the outskirts of the Perseus cluster, other nearby galaxy clusters (Bulbul et al. 2014), the Andromeda galaxy (Boyarsky et al. 2014) and the Milky Way centre (Boyarsky et al. 2015). Sterile neutrino dark matter is a two-parameter dark matter model described by the interplay of the lepton asymmetry at early times, and the mass of the sterile neutrino particle m_s (e.g. Boyarsky et al. 2009; Lovell et al. 2017a,b; Iršič et al. 2017; Robles et al. 2017). These particles originate at high energy from oscillations of active neutrinos and the probability of these events is directly proportional to the exceeding number of leptons over anti-leptons, i.e. L6. The level of lepton asymmetry (with L6=0, corresponding to the lack of asymmetry) strongly affects the primordial velocity distribution of these particles; specifically, at fixed neutrino masses higher values of L6 produce higher momentum particle and therefore warmer dark matter models. It should be stressed that the relation between L6 and the particle velocities is, however, non-monotonic, and we refer to Lovell et al. (2016) for more details. As a

result, different combinations of sterile neutrino mass and lepton asymmetry lead to dark matter models that can be cooler or warmer and induce, therefore, different levels of suppression in the matter density power-spectrum (see below for more details).

In addition to having possibly been detected, sterile neutrino particles also constitute a well-established extension of the Standard Model, called the three sterile neutrino model or minimal Standard Model (νMSM). By only adding three new particles this framework can not only explain the detection of the 3.5 keV line as the X-ray decay of a sterile neutrino of mass 7.1 keV, but it is also effective in the production of baryons and neutrino oscillations. Moreover, the νMSM model provides excellent opportunities to be observationally tested by X-rays observatories, since any sterile neutrino with mass $m_s > 2$ keV can be detected through its decay in X-rays, and the parameters that characterise the X-ray signal also determine the formation of structure in the Universe. The emission line is in fact directly linked to the mass of the sterile neutrino and by extension to the cut-off in the linear power spectrum of the dark matter distribution.

Hot Dark Matter

Hot dark matter candidate particles have low masses ranging from a few up to a few tens of eV and therefore decouple from the hot plasma at later times. The most obvious particle candidate are neutrinos. Hot dark matter has been ruled out as a viable form of dark matter by observations of the large scale structure such as those obtained by the CfA, the SDSS and 2dF galaxy surveys (Davis et al. 1982; Stoughton et al. 2002; Percival et al. 2001). Due to its relativistic velocity, hot dark matter would have freely streamed out of density perturbations and would have washed out any fluctuation at scales smaller than super-clusters.

1.3.3 Dark matter and structure formation

To first approximation, the distribution of matter in the Universe is fairly well described by a non-static viscous fluid in which three different and competing effects determine its hydrodynamical evolution: radiation pressure, gravity and the Hubble flow expansion. Under these conditions, random density fluctuations around a mean value can develop, and over-dense regions can significantly grow thanks to the pulling effect of gravity. Introducing the *relative density contrast* $\delta(\mathbf{r}, t) = [\rho(\mathbf{r}, t) - \overline{\rho}(t)] / \overline{\rho}(t)$ where $\overline{\rho}(t)$ is the background density of the Universe, it can be shown that, in the non-relativistic and linear regime, the growth of density perturbations over time is described by the following differential equation

$$\frac{d^2\delta}{dt^2} + 2\frac{\dot{a}}{a}\frac{d\delta}{dt} = \left[4\pi G\overline{\rho}(t) - \frac{\sigma_v^2(t)\,k^2}{a^2}\right]\delta\,, \tag{1.18}$$

where a is the scale factor, $\dot{a}/a$ is the rate of expansion of the Universe, σ_v is the dark matter velocity dispersion and k is the wave-number of the density perturbations. For the density perturbations to grow in time the right-hand side of this equation must be greater than zero, which leads to the Jeans mass as the critical value of mass above which perturbations will not be damped

$$M_J(t) = \frac{4\pi}{3}\left[\frac{\pi\sigma_v^2(t)}{4G\overline{\rho}(t)}\right]^{3/2}\rho_m(t)\,, \tag{1.19}$$

where ρ_m is the dark matter density. The background density of the Universe and the density of the dark matter both determine the Jeans mass and, together with the dark matter velocity dispersion, they affect its evolution across cosmic time. In the radiation dominated era of the early Universe, dark matter is still relativistic and being neutral, it does not interact with radiation. At this stage, the Jeans mass is still growing, until it reaches a constant value when the dark matter becomes non-relativistic. Later, at the epoch of matter-radiation equality, the evolution of the background density changes and as a consequence, the Jeans mass significantly drops. As soon as a mass scale becomes Jeans stable, the perturbations below that level will be damped. This means that the free streaming scale of the dark matter particle can also be defined as the maximum value of the Jeans mass across cosmic time, given that its thermal velocity at early times determines the length that it can travel before the era of matter-radiation equality. However, if at the time of matter-radiation equality the dark matter is relativistic, collapse and structure formation are prevented by the pressure of the dark matter itself until its velocity has dropped below relativistic levels. Equation (1.19) can then be used to understand how cold, warm and hot dark matter affect the formation of structures in the Universe, with the increasing free-streaming velocities leading to the suppression of structures at progressively larger scales. In practice, one has to solve the Einstein-Boltzmann equations to determine how the effect of particle free streaming will affect the matter density power-spectrum and consequently, the shape of the halo mass function.

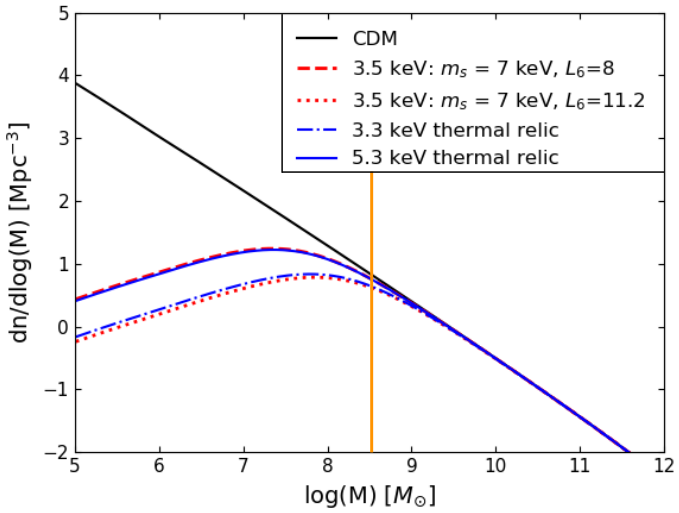

Figure 1.2: The differential halo mass function, i.e. the number density of haloes as a function of their mass for different dark matter models. The orange vertical line shows the mass value below which dark matter haloes start being completely dark. (Despali et al. 2016).

In Fig. 1.2 we show the differential halo mass function for the CDM model (black solid line), sterile neutrino models for different values of Lepton asymmetry and neutrino mass (red lines dotted and dashed lines) and two thermal relic models of different mass (blue solid and dashed line). This is a robust prediction of both models, and as we will discuss in the following section

and more in detail in the remaining part of this thesis, it offers a great opportunity to use strong gravitational lensing observations to constrain the nature of dark matter.

1.3.4 Strong gravitational lensing as a probe of dark matter

Strong gravitational lensing, being sensitive only to gravity, has played an essential role in revealing the presence of dark matter in galaxies and galaxy clusters. In this section, we discuss how strong gravitational lensing observations can be used to detect the large amount of low-mass dark-matter haloes that are predicted by the CDM model and thereby distinguish among competing dark matter models that lead to different predictions for the low-mass-end of the halo mass function. In particular, the strength of gravitational lensing in this respect is that it allows to detect dark matter haloes via their gravitational effect on the lensing observable and it is therefore independent of their baryonic content.

Flux Ratio anomalies

The analysis of flux-ratio anomalies consists in using the difference between the predicted and the measured fluxes of the multiple images of strongly gravitationally lensed quasars in order to detect the presence of low-mass dark-matter haloes. This idea was firstly suggested by (Mao & Schneider 1998), who argued that these measurements allow one to constrain the dark matter mass fraction of the lensing galaxy that is contained in subhaloes. In the following twenty years, many studies have strengthened this hypothesis from a theoretical perspective (e.g. Bradač et al. 2002). However, to avoid contamination from dust and microlensing such approach is limited to the analysis of radio-loud quasars, of which only a few are currently available (however, see Nierenberg et al. 2014, for the possibility of significantly increasing the samples size by focusing on narrow-line observations). Focusing on a sample of seven radio-loud systems Dalal & Kochanek (2002a) have derived the first statistical constraints on the dark matter mass fraction in subhaloes and found it to be larger than what is predicted by the CDM paradigm. This result has sparked a two-decade-long debate on the origin of flux ratio anomalies, with line-of-sight haloes (Chen et al. 2003; Metcalf 2005) and complex lens mass distribution (Möller et al. 2003; Inoue & Takahashi 2012) among the suggested alternatives. For example, Quadri et al. (2003) found that the observational signatures of baryonic components on flux ratios are not negligible, and affect 10 to 30 per cent of quadruply lensed quasars. More recently, Xu et al. (2012, 2015), from the analysis of high-resolution numerical simulations, have shown that the observed level of flux-ratio anomalies is larger than what can be obtained from CDM subhaloes and have also suggested the presence of complex baryonic structures in the lensing mass distribution as a possible solution. From an observational perspective, Hsueh et al. (2016, 2017) have found that the observed flux-ratio anomalies in two quadruply imaged quasars, which were previously attributed to subhaloes, could instead largely be explained by the presence of an unmodelled edge-on disk. Similarly, from the Illustris simulation (Vogelsberger et al. 2014), Hsueh et al. (2018) have found that the probability of finding flux-ratio anomalies increased by 10 to 20 per cent due to the presence of baryonic structures and disks. Gilman et al. (2017) have obtained a similar result from the analysis of simulated lens systems, based on *Hubble Space Telescope*

(*HST*) observations of low-redshift galaxies. These results, have demonstrated the importance of deep-imaging observations in order to have a precise measurement of the contribution of baryonic structures to the measured flux ratios. Besides subhalos and baryonic structures, recently Gilman et al. (2019) have shown that the perturbation caused by dark haloes along the line of sight is also significant in causing flux-ratio anomalies and that this gives further constraining power in terms of inference on the halo mass function (see also Metcalf 2005).
Recently, Hsueh et al. (2019) have analysed a sample of seven lensed quasars with significant overlap with the sample studied by Dalal & Kochanek (2002a). They find a total mass fraction in substructure of $f_{\rm sub} = 0.011^{+0.007}_{-0.005}$, consistent with CDM simulations at 1σ level. Moreover, assuming a thermal relic warm dark matter, they derive constraints on the dark matter particle mass which is found to be $m_{\rm wdm} > 3.8$keV. This result is in agreement with the current constraints coming from the Lyman-α forest (Iršič et al. 2017).

Lensed arcs and Einstein rings

As an alternative to the analysis of lensed quasars and their flux ratios, Koopmans (2005) and Vegetti & Koopmans (2009) have introduced a new method, the so-called *gravitational imaging* technique, whereby low-mass haloes are detected via their localized effect on the surface brightness distribution of magnified arcs and Einstein rings.
The *gravitational imaging* technique is at the basis of this thesis, therefore, we refer to the following chapters for a detailed description of the method. Here, we briefly summarise the current status on this field.
Vegetti et al. (2010b, 2012) have reported the first two detections of distant low-mass haloes. One discovered as a distant low-mass faint galaxy that would otherwise be undetectable, while the other, with a mass as small as $\sim 2 \times 10^8 M_\odot$ is comparable to the the Sagittarius satellite in the Milky Way, but at much larger cosmological distance ($z \sim 0.9$). From a sample of 11 SLACS lenses Vegetti et al. (2014) have derived statistical constraints on the dark matter mass fraction in substructure and found it to be consistent with CDM predictions from both CDM-only and hydro-dynamical numerical simulations. Using high-resolution numerical simulations Despali et al. (2016) have shown that both the number and structure of subhaloes is significantly affected by non-linear accretion processes that among other things depend on the details of the stellar and AGN feedback implementation in the simulations. On the other hand, Despali et al. (2018) have shown that at least 50 percent of the detectable signal is related to the presence of isolated field haloes along the line of sight to the lensed objects, opening a new channel for a robust test of the CDM paradigm. Based on this result, Vegetti et al. (2018) have derived the first constraints on the low-mass end of the halo mass function beyond the Local Universe from a sample of 11 SLACS lenses. Their results are consistent with CDM, but do not rule out alternative WDM models due to the relatively limited sensitivity of the data and low redshift distributions for both the lenses (z$\sim$ 0.2) and the sources (z $\sim$ 0.6).
To date, there have been only three published detections of low-mass haloes from observations of gravitationally lensed arcs at the optical/IR and mm-wavelengths (Vegetti et al. 2010b, 2012; Hezaveh et al. 2016). Although these detections provide a robust proof-of-concept for the discovery of low-mass dark-matter haloes at cosmological distances, the real power of this technique

comes from the study of larger samples of gravitational lenses with higher angular resolution and higher redshift distributions. In the near future, the large number of galaxy-scale lenses that are expected to be discovered by upcoming surveys such as with Euclid, the LSST and the SKA, coupled with high-resolution follow-up with the E-ELT, and Very Long Baseline interferometric observations will allow us to measure the halo mass function at a new low-mass regime of $10^{6-7} M_{\odot}$ with significant precision and, therefore, provide an invaluable test of the CDM model.

This Thesis

In this thesis we build upon the work by Vegetti et al. (2014) and Vegetti et al. (2018) by focusing on a sample of seventeen gravitational lenses from the BOSS Emission-Line Lens Survey (BELLS) for GALaxy-Lyα EmitteR sYstems (BELLS GALLERY Shu et al. 2016a). The strength of our sample lies in the relative large redshift range probed by the lenses ($z \sim 0.5$) and the sources $z \sim 2.5$), which allows us to sample a much larger cosmological volume than previous studies. Our results are presented in Chapter 4 where we combine the detections and non-detections of low-mass haloes to derive new statistical constraints on the halo mass function and compare the results with predictions from the CDM paradigm and different sterile neutrino dark matter models. Throughout the whole thesis, we assume the following cosmology, $H_0 = 71$ km s^{-1} Mpc^{-1}, $\Omega_{\rm m} = 0.27$ and $\Omega_{\Lambda} = 0.73$.

Chapter 2

Resolving on 100 pc-scales the UV-continuum in Lyman-α emitters between redshift 2 to 3 with gravitational lensing

Published on MNRAS as:
Ritondale, E., Auger, M. W., Vegetti S., McKean J. P. (2019), 'Resolving on 100 pc scales the UV-continuum in Lyman-α emitters between redshift 2 and 3 with gravitational lensing', *MNRAS* 482, 4744 - 4762.

2.1 Introduction

In this chapter, we use strong gravitational lensing to go beyond the current limits in angular resolution and investigate the size and structure of LAE galaxies at redshift $2< z <3$ on 100–500 pc-scales. Our study focuses on the first statistically significant sample of strong gravitational lenses with high-redshift LAEs as their background sources that were selected from the BOSS Emission Line Lens Survey (BELLS) by Shu et al. (2016a). To summarise, 1.4×10^6 galaxy spectra from the BOSS survey of the Sloan Digital Sky Survey-III were inspected to search for Lyman-α emission lines at a higher redshift than the dominant early-type galaxy in the spectrum. From this search, Shu et al. (2016a) selected twenty-one highest quality targets with source redshifts between $z \sim 2$ to 3 for follow-up imaging with the *HST*. This selection method is based on the successful technique used by the Sloan Lens ACS Survey (SLACS) to find over eighty-five gravitational lensed star-forming galaxies at lower redshifts (e.g. Bolton et al. 2006; Auger et al. 2009).

We present the gravitational lens mass models for seventeen of the twenty-one lens candidates, as well as an analysis of the sizes and star formation rates of the reconstructed ultra-violet (UV) continuum emission from the LAE galaxies. The structure of the chapter is as follows. In Section 2.2, we present the high angular resolution *HST* observations of the rest-frame UV

continuum emission from the BELLS sample of seventeen candidate LAE galaxies, from which we select the fifteen sources that we will use for our analysis. In Section 2.3, we describe the lens modelling procedure, which is based on an entirely Bayesian grid-based approach. In this section, we also present the recovered lens models and reconstructed sources, and we compare them with the models obtained by Shu et al. (2016b), where appropriate (see also Cornachione et al. 2018). In Section 2.4, we investigate the intrinsic properties of the rest-frame UV continuum emission of the reconstructed sources. Finally, we compare with other samples of LAEs in the literature and discuss our results in Section 2.5.

2.2 Data

The BELLS sample was observed with the *HST* using the WFC3-UVIS camera and the F606W filter (λ_c = 5887 Å; $\Delta\lambda$ = 2182 Å) between 2015 November and 2016 May (GO: 14189; PI: Bolton). In total, twenty-one candidates from the Shu et al. (2016a) sample were spectroscopically selected from the BELLS GALLERY of the Sloan Digital Sky Survey-III (Shu et al. 2016a). The sample is both lens and source selected: 1.4×10^6 spectra were analysed to search for Lyman-α emission lines at a redshift higher than the foreground early-type-galaxy emission (Shu et al. 2016a). As the source redshifts are between $z \sim 2.1$ and 2.8 and given the transmission curve of the F606W filter, these observations probe the rest-frame UV emission from young massive stars between 1250 and 2230 Å.

The data were retrieved from the *HST* archive and processed using the ASTRODRIZZLE task that is part of the DRIZZLEPAC package. Cut-out images for each target are shown in Fig. 2.1. Out of the twenty-one candidates, three are revealed not to be strong gravitational lenses with multiple clear images of the same background galaxy: SDSS J0054+2944, SDSS J1116+0915 and SDSS J1516+4954. Moreover, SDSS J2245+0040 is also not included in our final sample due to the uncertain nature of the deflector, which has several prominent star-forming regions (the SDSS spectrum also shows [OII], Hβ, and [OIII] emission lines). Without additional multi-band information, it is difficult to confidently distinguish structures belonging to the lens galaxy and the lensed images of the background source. Therefore, the sample used for our analysis contains seventeen gravitational lens systems (see also discussion by Shu et al. 2016b). The details about the individual objects in our final sample and the *HST* data that we have used are summarised in Table 2.1.

2.3 Gravitational Lens Modelling

Each gravitational lens system has been modelled independently with two different implementations of the Bayesian pixelated technique developed by Vegetti & Koopmans (2009). In particular, the results presented in the following sections are based on a new version of this technique, which also fits for the light distribution from the foreground lensing galaxy. In this section we provide more details on the new features of this version, while we refer the reader to Vegetti & Koopmans (2009) and Vegetti et al. (2014) for a more detailed description of the original method,

Table 2.1: Details of the gravitationally lensed LAEs used for our analysis.

Name (SDSS)	z_{lens}	z_{src}	λ_{rest} [Å]	Exp. Time [s]
J002927.38+254401.7	0.587	2.450	1706	2504
J011300.57+025046.2	0.623	2.609	1631	2484
J020121.39+322829.6	0.396	2.821	1540	2520
J023740.63−064112.9	0.486	2.249	1812	2488
J074249.68+334148.9	0.494	2.363	1751	2520
J075523.52+344539.5	0.722	2.634	1620	2520
J085621.59+201040.5	0.507	2.233	1821	2496
J091807.86+451856.7	0.581	2.344	1730	2676
J091859.21+510452.5	0.581	2.404	1730	2676
J111027.11+280838.4	0.607	2.399	1732	2504
J111040.42+364924.3	0.733	2.502	1682	2540
J114154.71+221628.8	0.586	2.762	1565	2496
J120159.02+474323.1	0.563	2.126	1883	2624
J122656.45+545739.0	0.498	2.732	1578	2676
J152926.41+401548.8	0.531	2.792	1553	2580
J222825.76+120503.9	0.530	2.832	1536	2492
J234248.68−012032.5	0.527	2.265	1803	2484

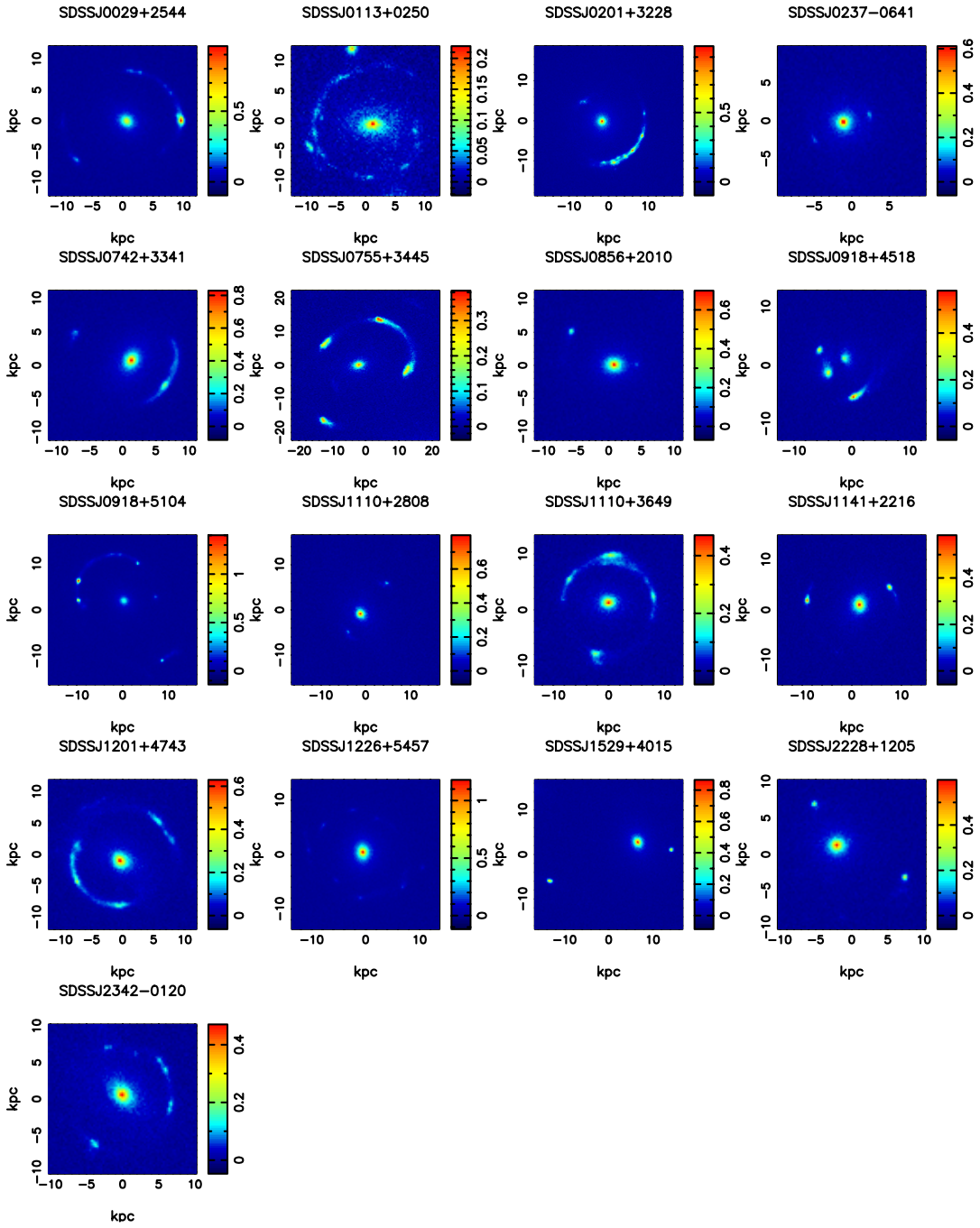

Figure 2.1: The *HST* WFC3-UVIS F606W imaging of each gravitational lens system. The surface brightness scale is in electrons s^{-1}. The lensing morphologies are quite varied, from nearly complete Einstein rings to very compact 2-image systems, with several examples of compound lenses (i.e. with multiple foreground galaxies causing the lensing, for example, SDSS J0918+4518).

and Vegetti et al. (2010a,b, 2012) for its application to high resolution optical and infrared imaging from the *HST*.

2.3.1 The Lens Model

We start by considering the observed surface brightness distribution $\boldsymbol{d}$ given by the combination of the lensed image $\boldsymbol{d}_s$ of an unknown extended background source $\boldsymbol{s}$ and the surface brightness distribution of the lensing galaxy $\boldsymbol{d}_l$. Both $\boldsymbol{d}$ and $\boldsymbol{s}$ are vectors representing the surface brightness distribution on a set of pixels in the lens (i.e. observed) plane and the source plane, respectively. The grid on the lens plane is defined by the native CCD pixelation of the data, while the grid on the source plane is defined by a magnification-adapted Delaunay tessellation (see Vegetti & Koopmans 2009, for more details). This approach provides a pixelated surface brightness distribution for the reconstructed source that is free from any parametrised assumptions, such as Sérsic or Gaussian light profiles, that may not adequately account for the clumpy nature of the rest-frame UV emission from the lensed sources.

We relate the relative positions of the pixels between the two planes via the lensing equation and the projected gravitational potential $\psi(x, \boldsymbol{\eta})$ of the lensing galaxy. The unknown parameters $\boldsymbol{\eta}$ defines the latter. Taking advantage of the fact that gravitational lensing conserves surface brightness and taking into account the observational noise $\boldsymbol{n}$ (assumed to be Gaussian and uncorrelated among data pixels), $\boldsymbol{d}$ and $\boldsymbol{s}$ can be related to each other via a set of linear equations,

$$\mathbf{B}\left[\mathbf{L} \mid (\boldsymbol{\Sigma_0} \ldots \boldsymbol{\Sigma_n}) \mid \mathbf{1}\right] \begin{pmatrix} \boldsymbol{s} \\ I_0 \\ . \\ . \\ . \\ I_n \\ b \end{pmatrix} + \boldsymbol{n} = \boldsymbol{d_s} + \boldsymbol{d_l} = \boldsymbol{d}. \tag{2.1}$$

Here, $\mathbf{B}$ is the blurring operator that expresses the effect of the point spread function (PSF). $\boldsymbol{\Sigma_i} I_i$ is the surface brightness distribution of the foreground gravitational lens(es). The latter is simultaneously modelled with the lens(es) mass distribution and is parametrized as elliptical Sérsic profiles each of normalization I_i, effective radius $R_{e,i}$, Sérsic index n_i and axis ratio q_i, such that,

$$S_i(x, y) = I_i \exp\left[-a_i\left(\left(\frac{\sqrt{q_i^2 x^2 + y^2}}{R_{e,i}}\right)^{1/n_i} - 1.0\right)\right] = I_i\, \Sigma_i(x, y)\ , \tag{2.2}$$

with $a_i = 1.9992\, n_i - 0.3271$. We refer to the Sérsic parameters (excluding the linearly determined normalizations I_i) collectively as $\boldsymbol{\eta_l}$. The last column of the response operator given in equation (2.1) represents a constant pedestal of amplitude b, expressing any residual sky background. Finally, $\mathbf{L}$ is the lensing operator and is related via the lens equation to the lens mass distribution. Here, the latter is parametrised with an external shear and an elliptical power-law profile of

dimensionless surface mass density κ, given by,

$$\kappa(x,y) = \frac{\kappa_0 \left(2 - \frac{\gamma}{2}\right) q^{\gamma-3/2}}{2\left(q^2\left(x^2 + r_c^2\right) + y^2\right)^{(\gamma-1)/2}}, \tag{2.3}$$

where κ_0 is the surface mass density normalisation, q is the axis ratio, γ is the radial slope and r_c the core-radius. In addition, the position angle of the elliptical mass distribution (θ), the shear strength (Γ) and positional angle (Γ_θ) are also free parameters of the model. We refer to the mass density parameters collectively as $\boldsymbol{\eta}$. The dimensionless surface mass density and the Einstein radius ($R_{\rm ein}$) are related to each other via

$$R_{\rm ein} = \left(\frac{\kappa_0 \left(2 - \frac{\gamma}{2}\right) q^{(\gamma-2)/2}}{3-\gamma}\right)^{1/(\gamma-1)}. \tag{2.4}$$

2.3.2 Lens modelling procedure

Redefining equation (2.1) as

$$\mathbf{Mr} + \mathbf{n} = \mathbf{d}, \tag{2.5}$$

we derive the maximum a posteriori model parameters (MAP) with a Simulated-Annealing technique by minimizing the penalty function,

$$P(\mathbf{r}, \boldsymbol{\eta}, \lambda \mid \mathbf{d}, \mathbf{H}) = ||\mathbf{Mr} - \mathbf{d}||_2^2 + \lambda^2 ||\mathbf{Hr}||_2^2, \tag{2.6}$$

where $\mathbf{H}$ and λ are respectively the form and (unknown) level of regularization for the source surface-brightness distribution and are mainly a form of prior on the level of smoothness of the background galaxy (see Suyu et al. 2006; Vegetti & Koopmans 2009). At each step of this optimisation scheme, the corresponding most probable source $\boldsymbol{s}$, sky background level b and the normalisation of each Sérsic component I_i are obtained by solving the linear system

$$\left(\mathbf{M^T C_d^{-1} M} + \lambda^2\, \mathbf{H^T H}\right)\mathbf{r} = \mathbf{M^T C_d^{-1} d}. \tag{2.7}$$

The main advantage of our modelling approach is that it explicitly accounts for any potential covariance in modelling of the foreground lens and background source surface-brightness; this is otherwise ignored if a model for the foreground light is estimated (e.g., by masking the pixels with significant flux from the lensed background source) and subtracted before performing the lens modelling.

This framework will provide a more robust determination of the surface brightness distribution of the background source, but it comes at the cost of significantly increasing the dimensionality of the non-linear parameter space, which is comprised of the foreground lens surface brightness and mass parameters, $\boldsymbol{\eta}_l$ and $\boldsymbol{\eta}$. To overcome this difficulty, the modelling procedure is performed in three steps. First we mask out the emission from the lens galaxy and, given the observed lensed surface brightness distribution $\boldsymbol{d}$, we optimize for the lens mass parameters $\boldsymbol{\eta} = \{\kappa_0, \theta, q, x, y, \gamma, \Gamma, \Gamma_\theta\}$ and the source regularization level. Then, using this as a starting point,

we parameterise the surface brightness distribution of the lens galaxy as a sum of multiple elliptical Sérsic profiles and optimise for the corresponding parameters, η_l. In the third and final step, we optimise simultaneously for the mass and the light distribution of the deflector and the source regularisation level.

Each lens system is modelled several times, allowing for different forms of regularisation (i.e. gradient or curvature) and different source plane grids. In the next section, we report the models with the highest Bayesian evidence. To quantify the uncertainties and probe any degeneracies among the model parameters, we use MultiNest (Feroz et al. 2013) to explore the parameter space within the prior volume. The latter is defined by uniform prior distributions on all parameters except for the source regularisation constant, for which we adopt a uniform prior in logarithmic space.

2.3.3 Lens modelling results

We present the inferred lens models and reconstructed sources in Fig. 2.2. The lens model parameters for each system are listed in Table 2.2 and the parameters for the Sérsic surface brightness distributions of the lensing galaxies are reported in Table 2.3.

The same systems have also been modelled by Shu et al. (2016b) (referred to as S16 in the following) under the assumption of a singular isothermal ellipsoid (SIE) mass distribution plus external shear. While our models allow for a varying slope, we don't find a significant departure from $\gamma = 2$. In general, our lens mass parameters are in a reasonable agreement with those reported by S16, with differences at the 10 percent level at most, except for SDSS J0201+3228, SDSS J0755+3445 and SDSS J0918+5104. We discuss these discrepancies in more detail below. In three other cases, SDSS J0237−0641, SDSS J1226+5457 and SDSS J2342−0120, the lens position angles differ by more than 10 percent but, since all these systems are well fitted by a circular mass distribution with axis ratios close to unity, this is just an apparent discrepancy.

We also find an agreement at the 4 percent level on the lens light parameters, except for the effective radii. This discrepancy is possibly related to a degeneracy between the effective radius and the Sérsic index, for which S16 do not report any values. We find that for SDSS J0237−0641 and SDSS J1226+5457 the light position angles differ by more than 4 percent, a discrepancy which is again explained by the roundness of the light profile.

From a qualitative comparison of the reconstructed sources, we notice that S16 report generally smoother and less compact sources than our reconstructions. This difference could be related to different choices of regularisation form and level. However, due to the lack of detailed information about the source regularisation in S16, it is not possible to draw strong conclusions on the origin of such a discrepancy, with the choice of masking also potentially playing an important role. In particular, six of the reconstructed sources are qualitatively different from the ones reported in S16, and a more detailed discussion of these discrepancies is given in the following subsections. We note that our two independent lensing codes lead to reconstructed sources that are consistent with each other.

In general, our models provide a better match, expressed in terms of image residuals, to the data. This result is particularly important to avoid the false detection of dark halos in the lens galaxies or along the line of sight. Nevertheless, in some cases, our source models do not

fully recover the data for pixels with a surface brightness much higher than that of neighbouring pixels. We do not believe that this is due to poor quality lens mass models, but is related instead to the regularisation imposed on the reconstructed source. Due to the pixelated nature of our source reconstruction technique, a prior on the smoothness of the source has to be imposed via equation (2.6). In practice, this is done by minimising either the gradient or the curvature of the surface brightness between neighbouring pixels on the source plane. While this allows us to avoid noise fitting and by-pass the ill-defined character of equation (2.1), it also makes it extremely challenging to recover the brightness of the brightest pixels where an extremely high dynamic range characterises the lensed images.

From the parameter space exploration, we find mean values that are consistent with our MAP parameters up to at most the 20 per cent level (see Tables 2.4 and 2.5). This difference often corresponds to a several σ discrepancy, which is related to the fact that the quoted errors are purely statistical and do not include the systematic uncertainty. We have estimated the latter by comparing the results obtained with the two different Bayesian techniques used for the modelling procedure and the results by Shu et al. (2016b), and found them to be at the 10 per cent level.

Apart from the usual degeneracies among some of the mass lens parameters (e.g. κ_0 and γ), we find no covariance between the lens light and mass parameters (e.g. see Fig. 2.4 for a typical case). This result is important as it implies that our mass models are robust against changes in the light model. This result is explicitly tested by re-modelling five systems after the lensing galaxy light has been fitted with a B-spline technique and subtracted from the data, inferring lens mass parameters consistent with our MAP parameters at the 10 percent level (see also Section 2.3.5). However, by comparing our results with those from S16, we find a certain level of degeneracy between the lens light parameters and the reconstructed sources in a way that also depends on the specific choice of masking and regularisation.

2.3.4 Specific cases

Here, we give comments on a few special systems and on those systems for which our results are significantly different from those obtained by S16.

SDSS J0029+2544

A particularly intense peak of surface brightness is visible in the images in the arc directly west from the lensing galaxy; this does not have a corresponding high-surface-brightness peak in the counter-image and is only partially recovered in our lens model. Multi-band observations would be required to identify its origin. While the image residuals and the mass parameters are in agreement with those reported by S16, our source has a different structure. In particular, our source is composed of one main component located on the cusp of the caustic and a second and fainter component lying on its left while in the source reconstructed by S16 the second component is much brighter. We believe the origin of this discrepancy to lie on the specific choice of masking and related regularisation effects. Finally, we infer light parameters that, except for the Sérsic effective radius (see discussion above), are in agreement with those reported by S16.

Table 2.2: The maximum a posteriori model parameters (MAP) for the gravitational lens mass models. The parameters of the mass density distribution reported are as follows: κ_0 is the normalization, θ is the position angle with respect to north, γ is the radial slope and q is the axis ratio. Γ and Γ_θ are respectively the magnitude and the position angle of the external shear (with respect to north).

Name (SDSS)	κ_0 [arcsec]	θ [deg]	q	γ	Γ	Γ_θ [deg]
J0029+2544	1.295	34.237	0.823	2.101	0.045	28.935
J0113+0250	1.226	81.671	0.730	2.046	0.001	184.002
	0.065	218.768	0.966	2.000		
	0.172	237.445	0.922	2.000		
J0201+3228	1.650	52.764	0.896	1.959	0.049	32.514
J0237−0641	0.687	39.575	0.881	1.914	0.008	237.567
J0742+3341	1.197	152.279	0.824	2.026	0.021	353.566
J0755+3445	1.926	105.347	0.533	1.898	0.230	31.865
J0856+2010	0.960	121.504	0.653	2.024	0.073	76.157
J0918+4518	0.444	41.410	0.843	2.036	0.086	82.185
	0.409	29.843	0.926	2.015		
J0918+5104	1.600	16.995	0.682	2.143	0.253	122.144
J1110+2808	0.992	41.672	0.892	2.016	0.020	317.727
J1110+3649	1.152	79.922	0.865	1.974	0.020	255.758
J1141+2216	1.281	150.356	0.751	1.983	0.003	14.071
J1201+4743	1.139	38.496	0.780	2.149	0.008	49.842
J1226+5457	1.351	72.448	0.970	2.055	0.153	161.277
J1529+4015	2.233	41.124	0.542	1.997	0.007	230.436
J2228+1205	1.290	176.851	0.923	1.966	0.034	3.539
J2342−0120	1.033	43.019	0.798	2.159	0.021	272.015

Table 2.3: The maximum a posteriori model parameters (MAP) for the Sérsic fits to the light of the lensing galaxies. For each system, we report for each lens and component (where multiple light profiles are fitted) the effective radius R_e, the Sérsic index n, the position angle ϕ (with respect to north) and the axis ratio f.

Name (SDSS)	lens	component	R_e [arcsec]	n	ϕ [deg]	f
J0029+2544			0.759	4.531	51.599	0.800
J0113+0250	1		1.277	3.472	85.330	0.583
	2		0.103	2.558	120.486	0.949
	3		0.292	2.574	206.409	0.579
J0201+3228		I	2.967	2.844	25.814	0.890
		II	0.241	5.557	149.106	0.915
J0237−0641			4.188	8.593	3.293	0.996
J0742+3341			2.057	6.356	149.261	0.708
J0755+3445			0.581	4.055	103.288	0.620
J0856+2010			0.950	4.752	94.637	0.784
J0918+4518	1	I	0.640	4.135	163.164	0.568
		II	0.059	3.871	176.439	0.630
	2		1.165	4.234	40.174	0.901
J0918+5104		I	0.485	2.817	42.549	0.878
		II	0.065	2.339	19.194	0.851
J1110+2808		I	0.675	3.468	56.278	0.780
		II	0.609	3.591	24.236	0.800
J1110+3649			0.889	5.625	88.740	0.756
J1141+2216		I	0.608	3.621	153.127	0.818
		II	0.249	3.640	151.045	0.822
J1201+4743		I	1.476	5.174	62.968	0.761
		II	1.132	5.336	52.551	0.750
J1226+5457			0.708	3.920	182.989	0.823
J1529+4015			1.630	5.945	19.098	0.805
J2228+1205			0.779	4.760	102.483	0.933
J2342−0120			2.123	5.903	43.973	0.655

Table 2.4: Mean values and relative errors for the lens mass models, derived using MultiNest. The uncertainties are purely statistical and do not include systematic errors. Note that for the two additional lenses in SDSS J0113+0250, the radial density slope was kept fixed at a value of $\gamma = 2$ (corresponding to a SIE) and therefore they are not reported here.

Name (SDSS)	κ_0 [arcsec]	θ [deg]	q	γ	Γ	Γ_θ [deg]
J0029+2544	1.320 ± 0.003	35 ± 4	0.94 ± 0.02	1.886 ± 0.002	0.05 ± 0.002	28 ± 2
J0113+0250	1.219 ± 0.005	80.6 ± 0.3	0.72 ± 0.01	2.08 ± 0.01	0.001 ± 0.0001	165 ± 14
	0.058 ± 0.003	236 ± 15	0.86 ± 0.05			
	0.176 ± 0.005	226 ± 9	0.82 ± 0.04			
J0201+3228	1.6604 ± 0.0001	53.5 ± 0.1	0.9105 ± 0.0005	1.8638 ± 0.0004	0.0489 ± 0.0002	34.91 ± 0.02
J0237−0641	0.7 ± 0.04	36 ± 0.9	0.8 ± 0.02	1.860 ± 0.04	0.007 ± 0.001	237.1 ± 3.3
J0742+3341	1.208 ± 0.005	151.9 ± 0.4	0.835± 0.007	1.98 ± 0.01	0.021 ± 0.001	352.6 ± 0.4
J0755+3445	1.86 ± 0.01	104.94 ± 0.05	0.531 ± 0.002	1.834 ± 0.01	0.232 ± 0.0005	30.18 ± 0.1
J0856+2010	1.093 ± 0.0004	100 ± 0.6	0.775 ± 0.001	1.820 ± 0.0004	0.072 ± 0.001	84.8 ± 0.7
J0918+4518	0.362 ± 0.005	47 ± 2	0.84 ± 0.03	2.15 ± 0.01	0.093 ± 0.003	78 ± 2
	0.48 ± 0.01	31 ± 3	0.938 ± 0.03	2.01 ± 0.01		
J0918+5104	1.560 ± 0.001	20.1 ± 0.1	0.703 ± 0.001	2.254 ± 0.002	0.267 ± 0.001	124.2 ± 0.03
J1110+2808	0.882 ± 0.004	45 ± 1	0.847 ± 0.007	2.210 ± 0.003	0.020 ± 0.002	320 ± 3
J1110+3649	1.116 ± 0.007	80.4 ± 0.3	0.79 ± 0.01	2.10 ± 0.01	0.016 ± 0.001	254 ± 1
J1141+2216	1.269 ± 0.004	155.8 ± 0.3	0.76 ± 0.01	1.92 ± 0.01	0.0034 ± 0.0002	14.1 ± 0.7
J1201+4743	1.147 ± 0.004	39.1 ± 0.3	0.799 ± 0.004	2.112 ± 0.006	0.010 ± 0.0005	42 ± 2
J1226+5457	1.355 ± 0.004	62.3 ± 0.4	0.915 ± 0.003	2.04 ± 0.02	0.162 ± 0.002	159.9 ± 0.1
J1529+4015	2.2 ± 0.01	37.1 ± 0.2	0.504 ± 0.01	2.00 ± 0.01	0.0075 ± 0.0004	222± 3
J2228+1205	1.266 ± 0.004	176.9 ± 0.2	0.899 ± 0.005	2.04 ± 0.01	0.033 ± 0.001	3.6 ± 0.2
J2342−0120	1.003 ± 0.001	40.8 ± 0.1	0.8765 ± 0.0004	2.0596 ± 0.001	0.0196 ± 0.0001	272.13 ± 0.05

Table 2.5: Mean values and relative errors for the lens light derived with MULTINEST. The uncertainties are purely statistical and do not include systematic errors.

Name (SDSS)	lens	component	R_e [arcsec]	n	ϕ [deg]	f
J0029+2544			0.74 ± 0.07	5 ± 0.3	51 ± 6	0.8 ± 0.1
J0113+0250	1		1.50 ± 0.03	3.70 ± 0.04	83.5 ± 0.6	0.59 ± 0.01
	2		0.102 ± 0.005	2.4 ± 0.2	125 ± 10	0.95 ± 0.02
	3		0.347 ± 0.003	2.08 ± 0.01	246.8 ± 0.7	0.49 ± 0.02
J0201+3228		I	2.79 ± 0.03	2.61 ± 0.02	27.56 ± 0.4	0.862 ± 0.004
		II	0.240 ± 0.004	5.49 ± 0.07	151.1 ± 1.6	0.88 ± 0.01
J0237−0641			4.7 ± 0.2	8.8 ± 0.2	3.3 ± 0.4	0.984 ± 0.008
J0742+3341			2.21 ± 0.04	6.5 ± 0.1	147.6 ± 0.5	0.705 ± 0.004
J0755+3445			0.62 ± 0.01	4.26 ± 0.05	102.012 ± 0.6	0.617 ± 0.006
J0856+2010			0.81 ± 0.02	4.44 ± 0.08	95.4 ± 0.6	0.779 ± 0.004
J0918+4518	1	I	0.56 ± 0.03	3.42 ± 0.08	164 ± 2	0.58 ± 0.03
		II	0.055 ± 0.002	3.14 ± 0.03	176.4 ± 0.4	0.61 ± 0.02
	2		1.34 ± 0.04	4.5 ± 0.1	40 ± 4	0.89 ± 0.02
J0918+5104		I	0.50 ± 0.01	2.90 ± 0.05	40 ± 2	0.882 ± 0.006
		II	0.071 ± 0.003	2.6 ± 0.1	19 ± 3	0.92 ± 0.04
J1110+2808		I	0.78 ± 0.02	4.03 ± 0.09	48 ± 2	0.65 ± 0.02
		II	0.70 ± 0.02	3.73 ± 0.04	21 ± 1	0.83 ± 0.01
J1110+3649			1.04 ± 0.02	6.05 ± 0.08	89 ± 1	0.756 ± 0.008
J1141+2216		I	0.65 ± 0.01	3.8 ± 0.05	153 ± 1	0.813 ± 0.007
		II	0.25 ± 0.01	3.7 ± 0.2	150 ± 2	0.79 ± 0.03
J1201+4743		I	1.72 ± 0.04	4.18 ± 0.03	62 ± 3	0.618 ± 0.007
		II	0.94 ± 0.03	5.34 ± 0.08	47 ± 1	0.737 ± 0.006
J1226+5457			0.69 ± 0.02	3.87 ± 0.06	181.3 ± 0.6	0.821 ± 0.004
J1529+4015			1.68 ± 0.05	6 ± 0.1	19.4 ± 0.5	0.805 ± 0.005
J2228+1205			0.83 ± 0.02	5.16 ± 0.06	102 ± 4	0.93 ± 0.01
J2342−0120			2.16 ± 0.03	6.02 ± 0.05	41.9 ± 0.5	0.652 ± 0.005

SDSS J0113+0250

This system is composed of three lenses, with the two secondary ones bending the arc respectively in the north and southeast direction. The third lens is located at a projected distance of approximately 2 arcsec from the main lens. For all three deflectors, the brightness profile is fitted using only one Sérsic component. The source has a particularly clumpy profile. Unlike S16, we find a significant improvement in terms of the Bayesian evidence and image residuals when the third lens is added to the mass distribution.

SDSS J0201+3228

Unlike S16, we infer a lens mass profile that is round, $q = 0.9$, rather than elliptical $q = 0.7$. For comparison, we have remodelled this dataset with an SIE profile of fixed axis ratio 0.7 and found that the rounder model is preferred by the Bayesian evidence, with a $\Delta \log E \simeq 900$. It should be stressed that both of our independent models based on our two codes disfavour an elliptical mass profile. Moreover, neither the surface brightness profile of the lens nor the lensing configuration from Fig. 2.1 suggests that this is an unusually elliptical lens. It may be that the difference in ellipticity between the S16 model and ours is counteracted by a difference in the external shear strength. However, we do not know with certainty, since S16 do not report the shear value for this lens. Finally, the lens galaxy light of this system was fitted using a sum of two Sérsic profiles.

The image-plane residuals for SDSS J0201+3228 are probably the worst case within the sample, with 4 knots of positive and negative emission that have normalised residuals around 2.5σ along the extended arc to the south-west. We note that the residuals in S16 are significantly worse for both their Sérsic and grid-based source models. The strong residuals may be due to either the complex source structure requiring an adaptive regularisation to account for both the smooth and compact structure (requiring a higher dynamic range) or a mismatch between the elliptical power-law model and the actual mass distribution of the deflector. In Chapter 3, we investigate more complex lens models for this system using grid-based corrections to the lensing potential, but we find that these do not improve the image residuals significantly. Therefore, any inference of the source properties for this object is left for a future analysis when multi-band data are available.

SDSS J0237−0641, SDSS J0856+2010, SDSS J1141+2216

For these three systems, our reconstructed sources appear significantly different from those presented by S16, both regarding their position with respect to the caustic and their shape. The models for SDSS J0237−0641 are comparable in terms of residuals, while our models for SDSS J0856+2010 and SDSS J1141+2216 seem to fit the data better as they present less significant residuals. The mass and light models are consistent for the three systems, except for the effective radii of the Sérsic model. For the system SDSS J1141+2216, a direct comparison with the Sérsic fitting results by S16 is not possible as we have parametrised the lens light distribution with two components rather than one. We believe the discrepancy among the sources to be related to the proximity of the lensing galaxies to the lensed emission, especially in SDSS J0237−0641. This configuration makes it harder to distinguish between lensed and lens

emission, and effectively introduces a degeneracy between the light model of the foreground lens and the surface brightness of the reconstructed source, which depends on the specific choice of masking. It should also be noted that these are all doubly-imaged systems; therefore the data provides us with relatively limited information to constrain the mass and the source model.

SDSS J0755+3445

The modelling of this quadruple image system was possible only through allowing for a strong external shear. In fact, this can already be inferred by noting that the image separation between the central part of the arc and the counter-image is significantly larger than the aperture of the arc, denoting the presence of an external element that perturbs the lensing configuration. Another component of the source is lensed in the two opposite and faint images located along the southwest-northeast diagonal. The galaxy to the southwest direction was found not to have any influence on the lens mass model and was therefore ignored in the modelling procedure.

The LAE source of this system was also reconstructed via the *gravitational imaging technique* (see VK09). We refer to Chapter 4 for a more detailed description of this procedure. We find that the diffused low-level pixellated convergence corrections which are added to the single power-law model result in a more compact source with a less pronounced tail as shown in Figure 2.3. We therefore conclude that a single power-law model is not representative of the mass distribution of the deflector and any inference of the source properties is left for a future analysis when multi-band data are available.

SDSS J0918+4518

Both the light and mass models of the lens are in disagreement with those reported by S16. The structure of the source is also significantly different, as expected from the divergent lens models. In particular, according to our model, both deflectors have approximately equal lensing strength and are both almost round with an axis ratio of $q \simeq 0.9$. Instead, one of the lenses in the model by S16 is strongly elliptical, with an axis ratio of $q = 0.132$, and has a different lensing strength. When using the lens parameters by S16 to model this system, we find that our model is preferred with a difference in Bayesian evidence of $\Delta \log E \simeq 200$. Moreover, our residuals are less prominent, and our results are consistent between our two independent lens modelling codes.

SDSS J0918+5104

We find that a large external shear had to be allowed to account for the general lensing configuration of this system and the displacement of the counter-image towards the southwest direction. We find that the foreground object to the west of the primary lens is not contributing significantly to the lensing signal, and we did not include its contribution into the final mass model. However, we had to take into account for its brightness distribution which was modelled with two Sérsic profiles, while only one component was necessary to account for the lens galaxy emission. Our mass model requires a stronger ellipticity and a stronger external shear in comparison with

the one presented by S16. We remodelled this dataset with an SIE profile of fixed axis ratio $q = 0.985$ and fixed shear strength $\Gamma = 0.18$, as determined by S16, and found that our model is preferred by the Bayesian evidence, with a $\Delta \log E \simeq 300$. Finally, we remark that our reconstructed source appears more compact and closer to the caustic. This result is probably due to the difference between the two mass models.

SDSS J1110+2808

The image residuals and the appearance of the source are consistent with the results presented by S16, and the lens models are in agreement at the 3 percent level. However, unlike S16, we find that the lens light profile is better fitted with two rather than one Sérsic component.

SDSS J1529+4015

This system is composed of two sources at two different redshifts, as can be seen from the different image separation of the two sets of arcs in Fig. 2.1. The first source corresponds to the two bright images on the opposite sides of the lens galaxy, and the other source is lensed into the faint arc on the right with the counter-image located below the bright image on the left. Since the second set of images is too faint to be used to reconstruct the lens model it is masked out of the data.

2.3.5 B-spline subtracted data

We find that for five systems, namely SDSS J0113+0250, SDSS J0918+4518, SDSS J1110+2808, SDSS J1141+2216 and SDSS J2342−0120, a simple Sérsic profile (with one or more components) does not provide a good fit to the complex light structure of the lens galaxy. However, as we are mainly interested in the lens mass parameters and the background source properties, we test their robustness by modelling a version of the data where the lens galaxy light has been previously fitted and subtracted using a B-spline method. In agreement with the results from MultiNest, we find no covariance between the mass and light parameters, and we recover lens mass parameters that are in agreement with those derived from the simultaneous fit of the lens mass and light. Moreover, since for these systems the Sérsic profiles provide a bad fit only to the central regions of the lens galaxy light, we find that also the reconstructed sources are consistent among the two different modelling approaches.

2.3.6 Testing for systematics in the source structure

Finally, we have quantified how the imposed regularisation can affect the compactness and morphology of the reconstructed source and our results. For this, we have performed a series of simulations by creating mock Gaussian sources of different sizes and lensing them through the best-fitting lens model for SDSS J0029+2544. These are then convolved with the *HST* PSF to create synthetic datasets, and reconstructed using the modelling procedure described in Section 2.3.1. We then compare the size of the original Gaussian source with the reconstructed

source that includes the effects of the regularisation. In all cases, we find that we robustly recover the properties of sources as small as 30 mas.

2.4 Intrinsic properties of LAEs

In this section, we present the inferred properties of the reconstructed LAE galaxies, including their morphologies, sizes, and SFR intensities.

2.4.1 Determining the intrinsic properties

An essential application of gravitational lensing is to study the high-redshift Universe in a way that is not easily possible without the magnification provided by the foreground lensing galaxy. Potentially, this could be problematic, especially for extended objects, where the magnification can significantly change over the extent of the source.

However, as our methodology already corrects for the distortion caused by the intervening gravitational lens (and the blurring caused by the PSF), our reconstructed sources are not affected by differential magnification. We note that due to the differing magnification over the source, there is an effective differential sensitivity and resolution across each object, although this is not an issue for our purposes. In fact we are interested in the global properties of these sources, rather than to their detailed structure. Therefore, we measure the intrinsic properties of the LAEs in the sample directly from their reconstructed UV surface brightness distributions.

To determine the star-forming properties of the sample, we use the standard methodology by assuming the rest-frame flux (F_λ) varies with some power-law, such that,

$$F_\lambda \propto \lambda^\beta \tag{2.8}$$

where β depends on the dust content of the galaxy and the age, metallicity and the initial mass function of the stellar population. As we have only one measurement of F_λ from the F606W imaging, it is not possible to calculate β for each object. Therefore, here we assume a typical value of $\beta = -1.5$ for LAEs at redshifts between 2 and 3 (Nilsson et al. 2009; Guaita et al. 2010). Note that as the central (rest-frame) wavelength of the data is close to the UV-reference wavelength of $\lambda_{\rm UV} = 1600$ Å (see Table 2.1), assuming a typical range of values of 0 to -2.5 for β (e.g. Nilsson et al. 2009; Blanc et al. 2011; Hashimoto et al. 2017) changes our derived values by at most 30 percent in the case of the integrated SFR of each object. If β is not constant across the source, due to either a complex dust distribution or if there are multiple stellar populations (the former is the more likely for these sources; Leitherer & Heckman 1995; Bouwens et al. 2009), then the uncertainties in the SFR intensity maps from this assumption may be more pronounced. As we will compare with other samples similarly observed (at lower intrinsic angular resolutions), this will not significantly affect our analysis either.

We compute the SFR of each LAE using,

$$\mathrm{SFR}\ [\mathrm{M}_\odot\ \mathrm{yr}^{-1}] = K_\nu \times L_\nu, \tag{2.9}$$

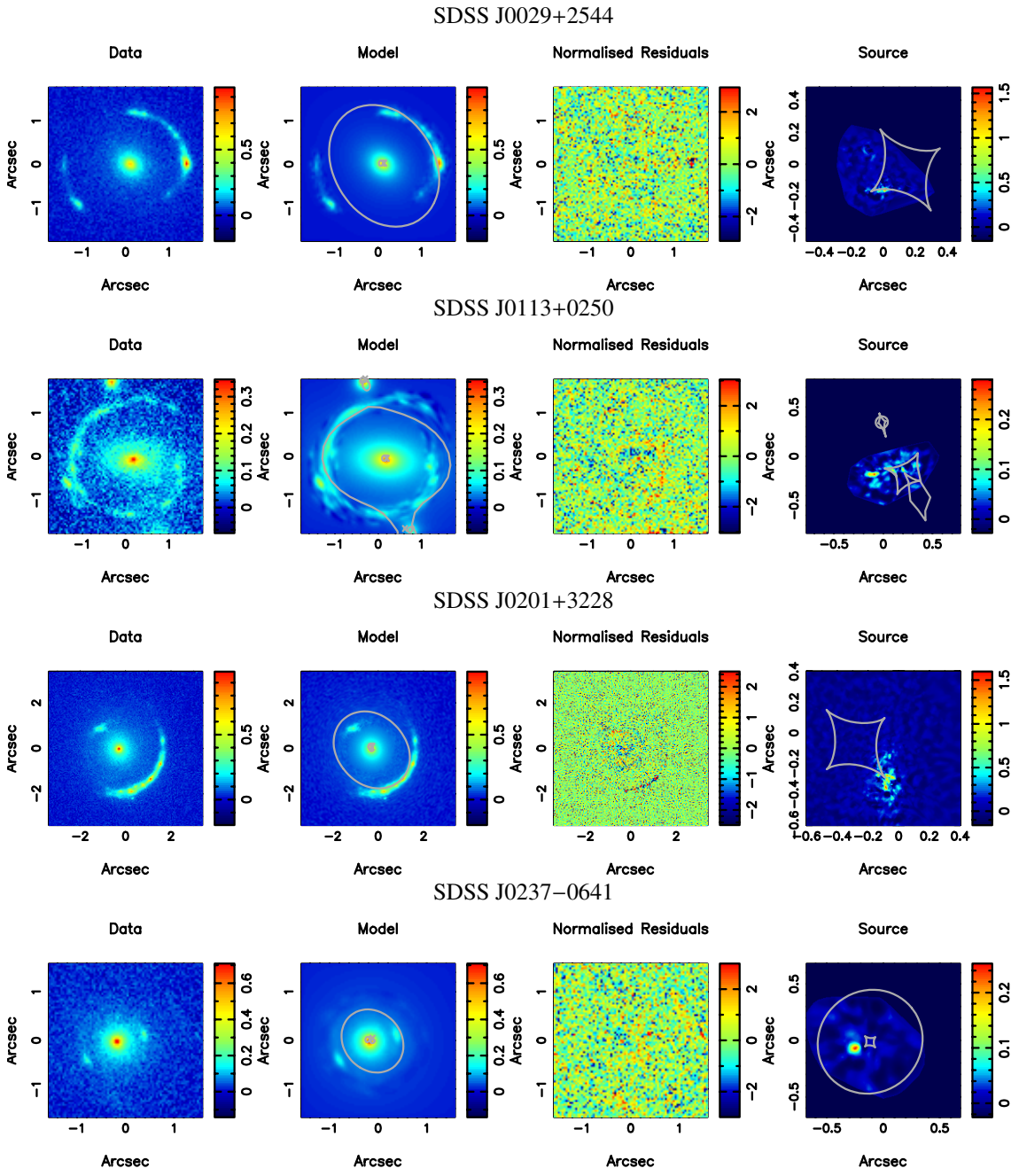

Figure 2.2: Models for the gravitational lens systems, given in the same order as in Table 2.2. Each row shows (left) the input *HST* F606W imaging, (middle-left) the reconstructed model for lens-plane surface brightness distribution of the gravitational lensing galaxy and the gravitationally lensed LAE galaxy, (middle-right) the normalized image residuals in units of σ, and (right) the reconstructed surface brightness distribution of the LAE galaxy. Shown in grey are the gravitational lens mass model critical curves in the lens-plane and the caustics in the source-plane.

SDSS J0742+3341

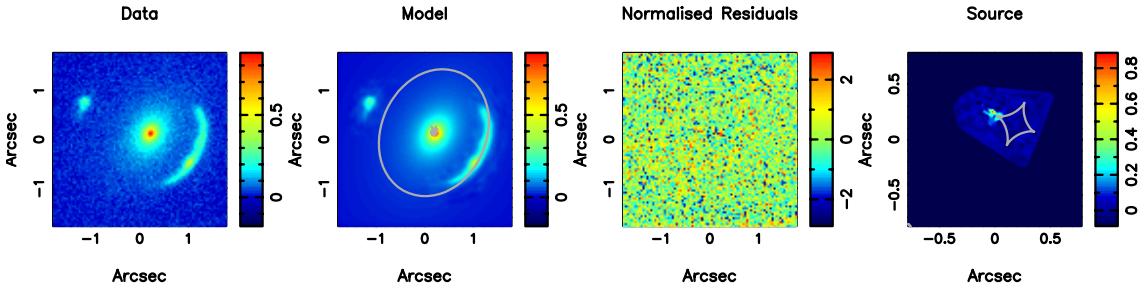

SDSS J0755+3445

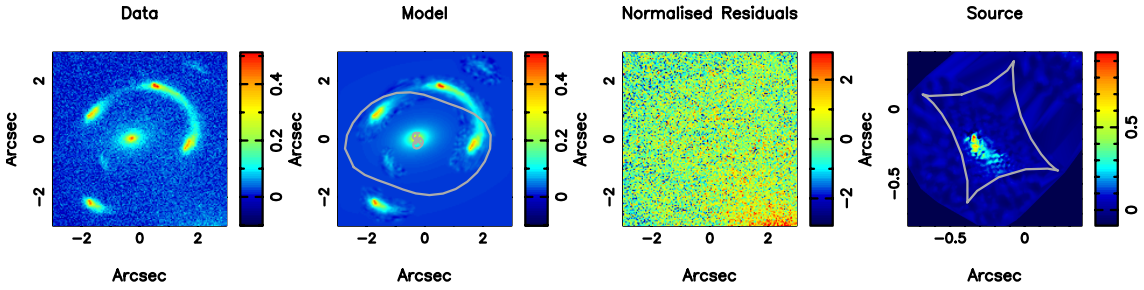

SDSS J0856+2010

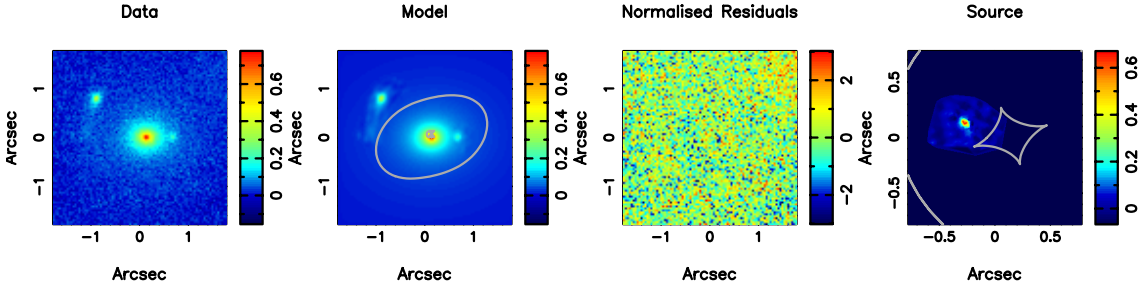

SDSS J0918+4518

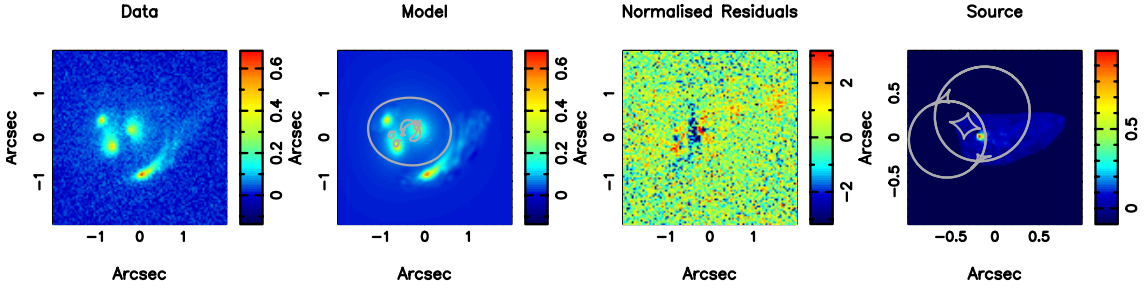

SDSS J0918+5104

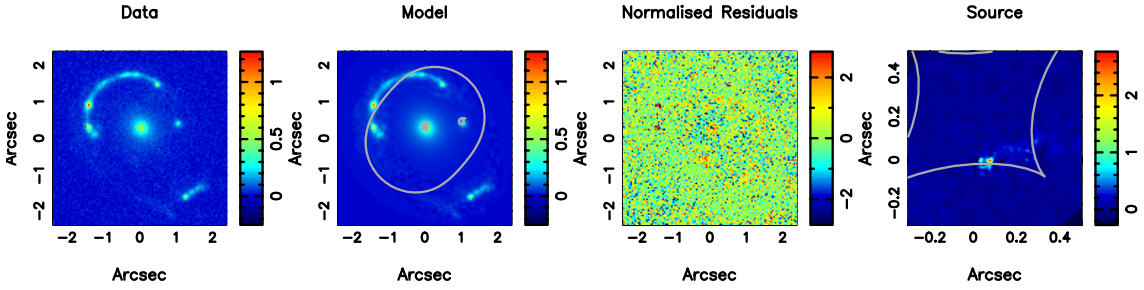

SDSS J1110+2808

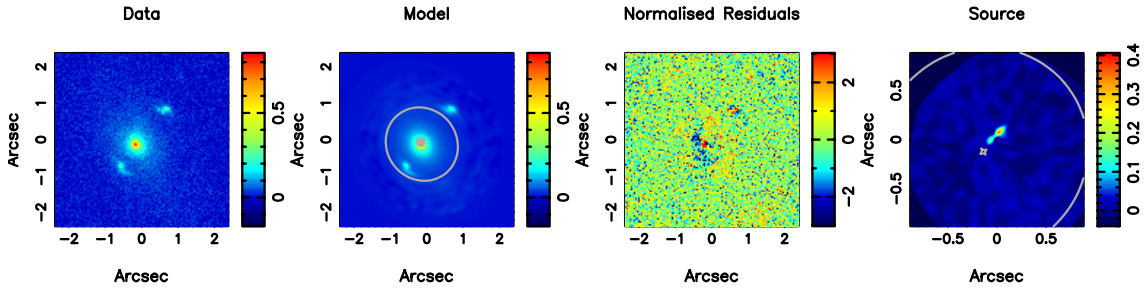

SDSS J1110+3649

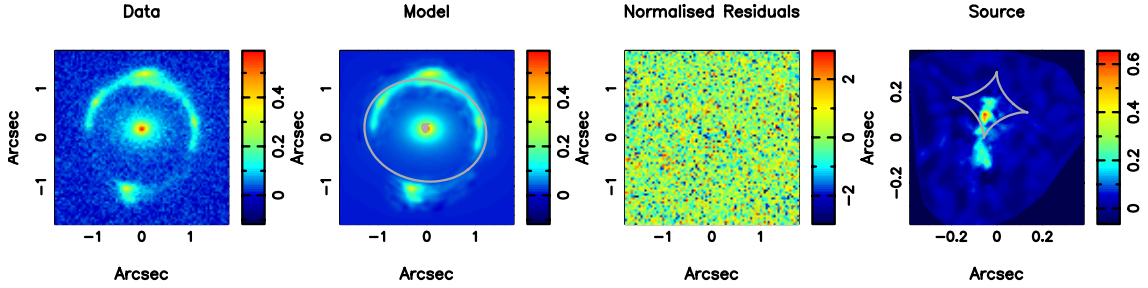

SDSS J1141+2216

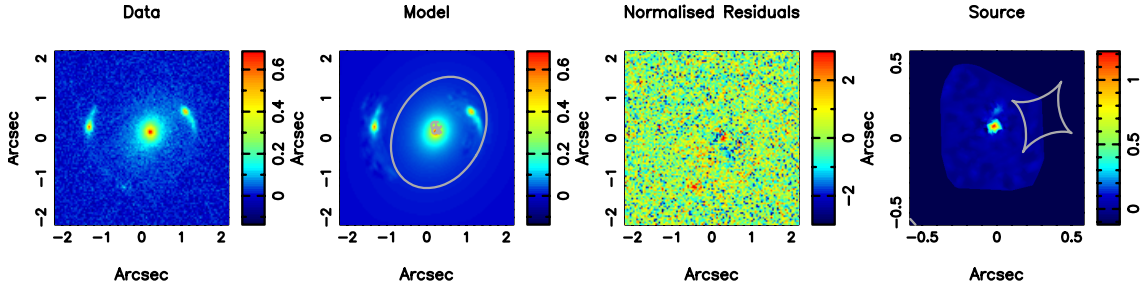

SDSS J1201+4743

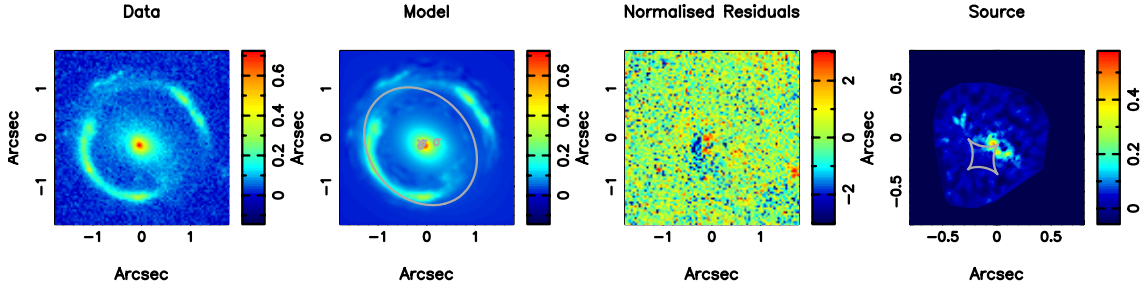

SDSS J1226+5457

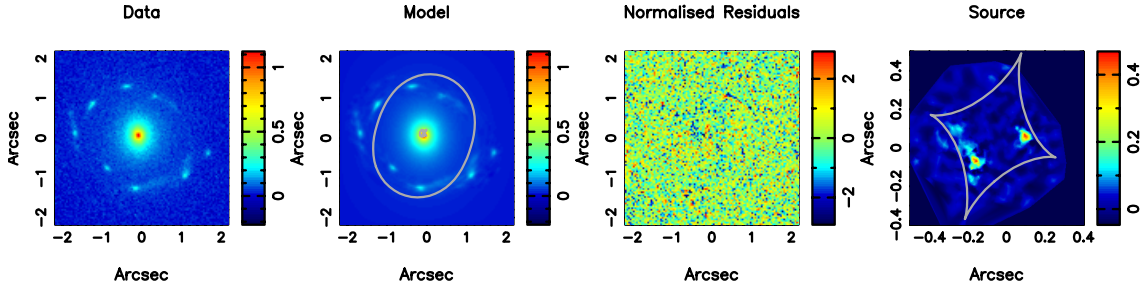

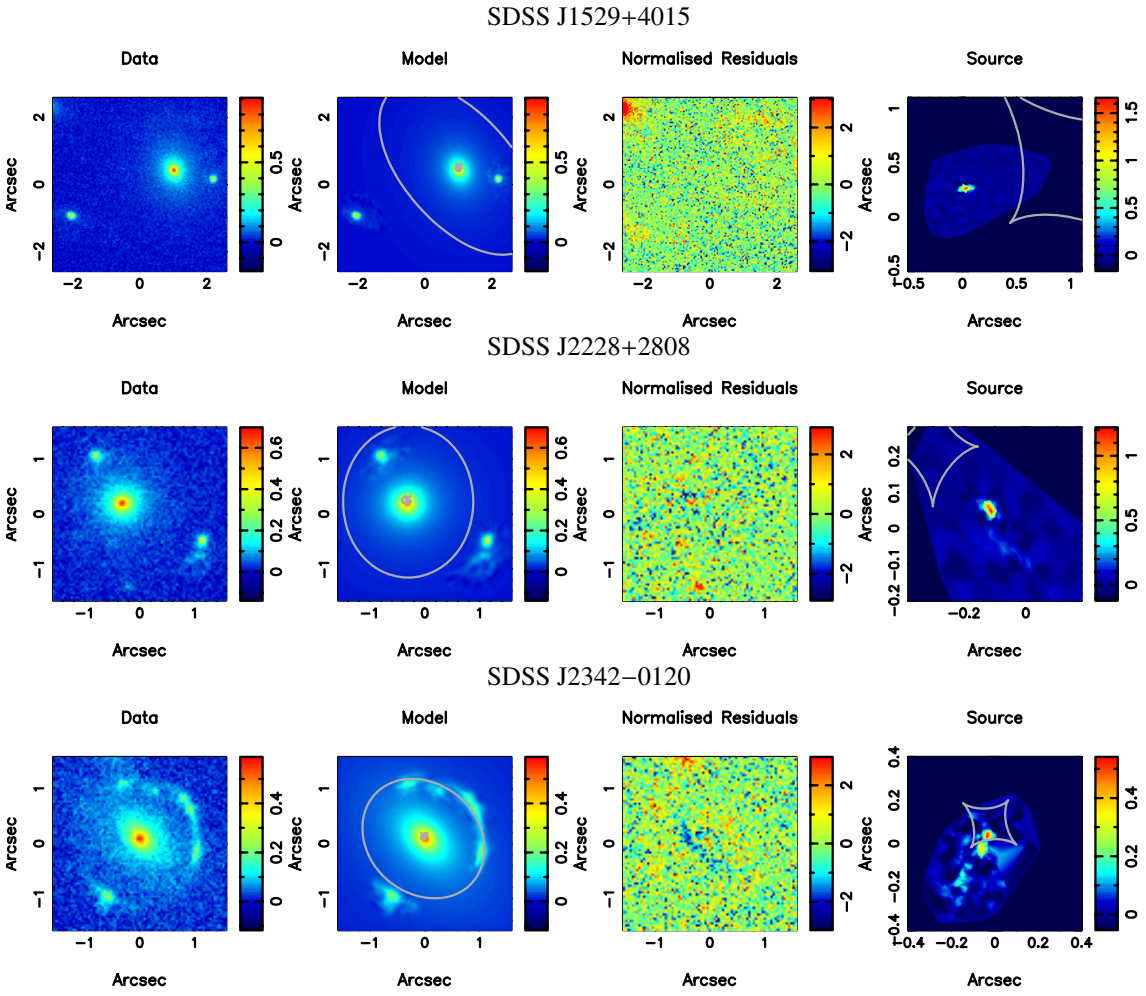
SDSS J1529+4015
Data
Model
Normalised Residuals
Source
Arcsec
SDSS J2228+2808
Data
Model
Normalised Residuals
Source
Arcsec
SDSS J2342−0120
Data
Model
Normalised Residuals
Source
Arcsec

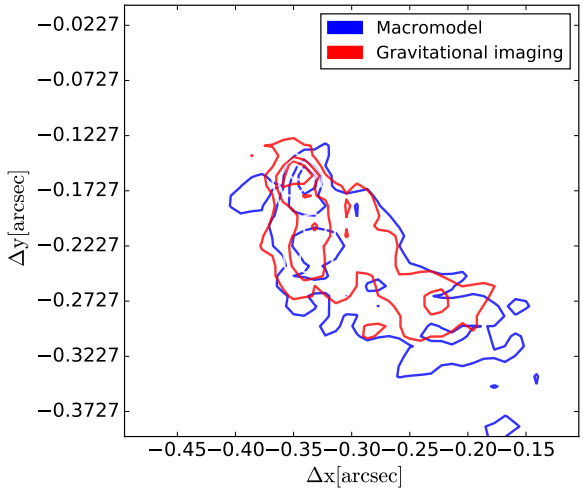

Figure 2.3: Reconstructed source structure for the lens system SDSS J0755+3445. The blue contours show the source structure inferred under the assumption of a single power-law mass model for the lens galaxy. The red contours show the reconstructed source when the system is modelled with the gravitational imaging technique.

where L_ν is expressed in units of erg s^{-1} Hz^{-1} and $K_\nu = 1.15\times10^{-28}$ is the FUV conversion factor (for the units given in equation (2.9)) between the spectral luminosity and ongoing SFR, adopted from Madau & Dickinson (2014). Our maps of the SFR intensity (M$_\odot$ yr^{-1} kpc^{-2}) of each object are shown in Fig. 2.5.

The reconstructed sources have a wide range of structures and morphologies, which we discuss in detail below. We note that Shu et al. (2016b) have quantified the lens model parameters and the properties of their sources by fitting elliptical Sérsic profiles to the reconstructed background galaxy surface brightness. They use pixellisation only for the multiple component sources in order to guess the number of Sérsic components needed to describe the source surface brightness. However, we have found that in general the sources have quite an irregular surface brightness distribution and we, therefore, choose to characterise all the sources in the sample in a less model-dependent manner always using the pixellated reconstructions.

Our modelling procedure described in Section 2.3 constrains the surface brightness at points on an *irregular grid* defined by the mapping of the positions of the observed pixels back to the unlensed source plane (see Vegetti & Koopmans 2009, for example). We quantify the structure of each source by finding the minimum best-fitting ellipse that encloses the points within this grid that have a signal-to-noise ratio larger than 3, and we report the mean major-axis size and ellipticity of each ellipse in Table 2.6. In addition we use the aperture defined by the ellipse to measure the integrated SFR of each object (note that as SDSS J1226+5457 is composed of two well-separated objects, we report separate values for each of these components). The mean SFR intensities are determined by dividing these by the area of each elliptical region. We also report the *peak* SFR intensity, which is robustly determined because gravitational lensing

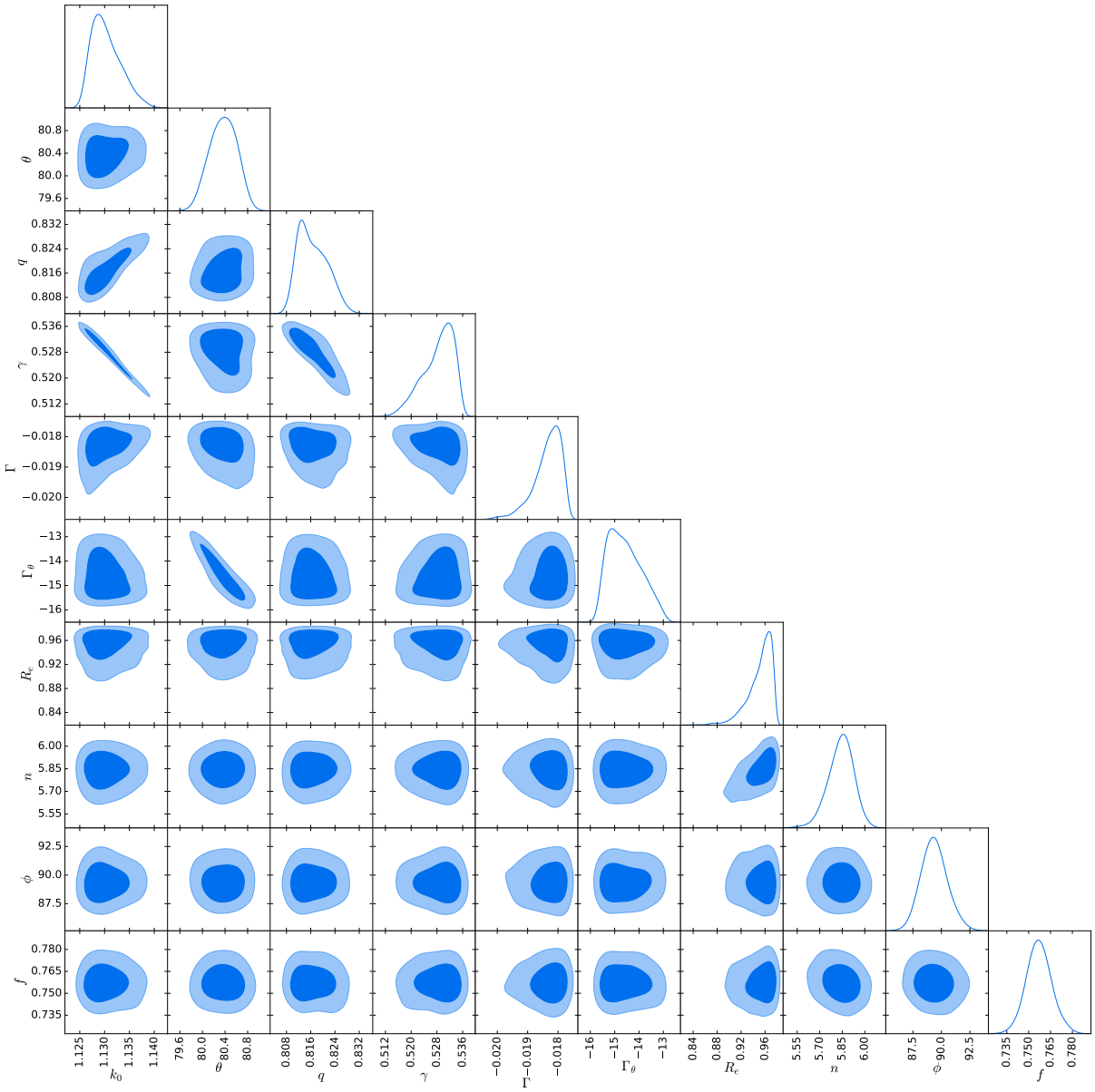

Figure 2.4: The posterior probability distribution for the mass and light parameters of the lens galaxy in SDSSJ 1110+3649. The contours for the 68% and 95% confidence level are shown. Apart from the usual degeneracies among the lens mass parameters, no degeneracy is found between the mass and light models.

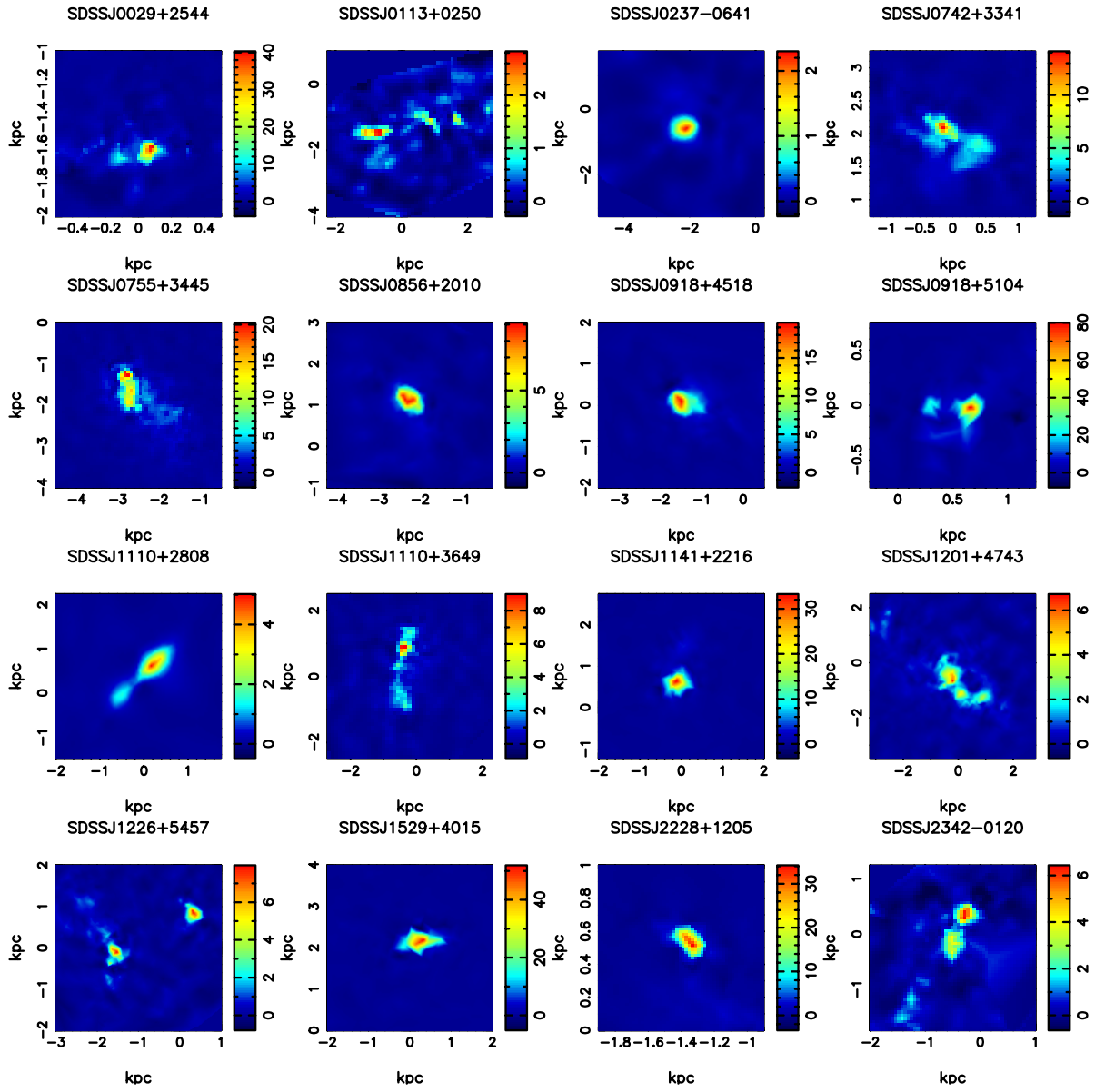

Figure 2.5: The star-formation rate intensity of each object, based on the source reconstructions from the grid-based gravitational lens modelling. The colour-scale for each object is in units of $M_\odot\ yr^{-1}\ kpc^{-2}$.

conserves the surface brightness and the multiple images allow for the effects of the PSF to be mitigated. Finally, we take one hundred random MCMC realisations of the lens mass model for each object and reconstruct the source in each case to quantify the errors on the morphological and physical properties of the source. We note that in some cases the zero uncertainties reported in Table 2.6 are due to insignificant changes from one MCMC realisation to the other. These properties are also presented in Table 2.6, except for two cases, SDSS J0201+3228 and SDSS J0755+3445. The residuals in the image plane and the extremely clumpy structure of the source of SDSS J0201+3228 suggest that multi-band data are needed to properly constrain the mass model and the source properties, as already discussed in Section 2.3.4. In the case of SDSS J0755+3445, we could not perform a MCMC to draw realisations and compute the errors for the reconstructed source since the lens model required pixellated potential corrections to obtain a good fit.

2.4.2 Source morphologies

From Fig. 2.5, it is clear that the reconstructions of the LAEs have a range of morphological features, with multiple regions that have both compact and diffuse star-formation spread over 0.4 to 4 kpc in projected separation. Except for the double component source SDSS J1226+5457, there tends to be a single dominant star-forming clump in each case. From Table 2.6 and Fig. 2.6, we see that the major-axis sizes vary from 220 pc in the most compact sources (including low magnification doubly imaged systems where this is likely an upper limit; SDSS J0237−0641 and SDSS J0856+2010) to around 1.5 to 1.8 kpc in the cases of the most extended structures (SDSS J0113+0250, SDSS J1110+3649 and SDSS J1201+4743). Note that in the most compact sources (major-axis < 330 pc), the intrinsic size is below the native pixel size of the UVIS camera on WFC3. This result highlights how gravitational lensing can be used to magnify structures in the high-redshift Universe; in fact, 10 out of 16 sources have major-axis sizes < 660 pc (equivalent to 2 native pixel sizes), and the median major-axis size of the sample is 561^{+13}_{-110} pc.

Also, almost all of the resolved sources have elongated structures that could be potentially interpreted as disks of star-formation. Again from Fig. 2.5, there is evidence that the multiple clumps of star-formation tend to be co-linear, as we would expect if there is a disk-like structure (Swinbank et al. 2009). However, some kinematic tracer, such as emission lines in the optical- and mm-regime, will be needed to confirm this. We find that the axial-ratios of the ellipses that are fitted to the surface brightness distributions have a range from 0.18 in the most elongated case of SDSS J0113+0250, to 0.91 for the almost circular case of SDSS J0918+4518. From Fig. 2.6, we find that the distribution in axial ratio is quite flat, with a median of $0.51^{+0.01}_{-0.01}$.

2.4.3 Star-formation rates and intensities

The derived SFRs from the UV-continuum for the LAEs in the sample vary by one order of magnitude, which gives some indication of the heterogeneous nature of the host galaxy properties. We recall that the objects in our sample were not selected based on their UV-continuum flux, but via the gravitational lensing of their Lyman-α emission, which may be affected by a varying Lyman-α escape fraction, slit-losses due to the finite size of the SDSS fibre and differential

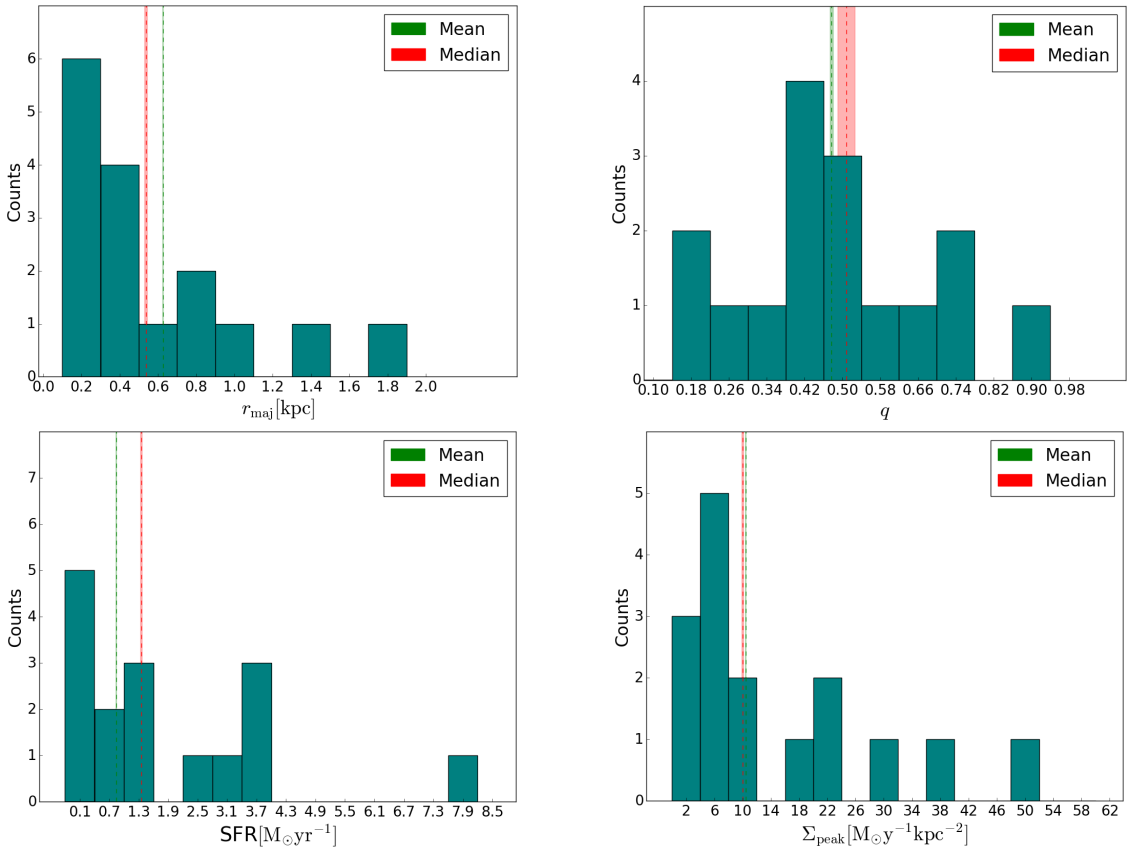

Figure 2.6: From top to bottom: the distribution of major-axis sizes, axial-ratios, star-formation rates and peak star-formation rates intensities for the sample, with the mean and median (and their uncertainties) shown for reference.

magnification. The lowest SFR in the sample is just 0.32 $M_\odot$ yr^{-1} for SDSS J0237−0641 and the largest SFR is 8.5 $M_\odot$ yr^{-1} for SDSS J1529+4015 (see Table 2.6). From Fig. 2.6, we find that the distribution of SFRs is clustered towards the lower end, with 10 out of 16 sources having a SFR less than just 2 $M_\odot$ yr^{-1}. The median SFR for the whole sample is $1.37^{+0.06}_{-0.07}$ $M_\odot$ yr^{-1}, which is comparable to the SFR of our own Milky Way.

Even though the galaxies are quite compact (median size of 561^{+13}_{-110} pc; see above), their low SFRs still result in a relatively low average SFR intensity across each galaxy. We find that the average SFR intensities vary from 0.4 to 17.6 $M_\odot$ yr^{-1} kpc^{-2}, while we find a median of $3.51^{+0.07}_{-0.06}$ $M_\odot$ yr^{-1} kpc^{-2}. Furthermore, as described above, the morphology of the galaxies are typically characterised by a dominant star-forming component. The peak SFR intensity of the sample varies from 2.1 to 54.1 $M_\odot$ yr^{-1} kpc^{-2} (see Table 2.6). However, from Fig. 2.6 we find that the distribution has a peak around 6 $M_\odot$ yr^{-1} kpc^{-2} with an extended flat tail out to high peak SFR intensities. There does not seem to be a strong correlation between whether the LAE galaxy is compact or extended (based on the size of the major axis), and the peak in the SFR intensity. Overall, the sample has a median peak SFR intensity of $10.1^{+0.5}_{-0.4}$ $M_\odot$ yr^{-1} kpc^{-2}.

2.5 Discussion

In this section, we discuss our results and compare the properties of the gravitationally lensed sample of LAEs investigated here with the large samples of non-lensed objects that have been studied thus far with different methods (e.g. narrowband imaging and spectroscopy). We also compare with the small number of lensed LAEs that have been studied.

2.5.1 Morphology

Current morphological studies of hundreds of non-lensed LAEs at moderate to high redshifts ($z \sim 2$ to 6) have been mainly limited by the angular resolution of the available imaging for both the line and continuum emitting regions, which could potentially bias the interpretation of data. For example, the UV-continuum morphologies have typically been classified as either single, marginally resolved components, or those with evidence for multiple components that are well separated on the sky. For those marginally resolved cases, studies have found that the de-convolved half-light radii of the single component LAEs are typically between 0.45 and 2 kpc in size, with a median half-light radius of 0.85 kpc (Hagen et al. 2016; Kobayashi et al. 2016; Paulino-Afonso et al. 2018). In addition, there is strong evidence for a lack of evolution in the size of LAEs with redshift, suggesting that there is a characteristic scale for the stellar continuum emission within LAEs (Malhotra et al. 2012; Blanc et al. 2011). However, as the lower size limit approaches the pixel-scale of the imaging instruments on the *HST*, it is not clear how robust this conclusion is. Also, there are examples of LAEs with multiple individual UV-continuum components (with a similar size to those discussed above), but separated up to 4 kpc in projection (Swinbank et al. 2009; Kobayashi et al. 2016). In these cases, it is thought that the separate components are in the process of merging/interacting, which results in the triggering of star formation in the spatially distinct regions. However, these types of LAEs are somewhat rare,

Table 2.6: The derived AB F606W magnitude, major-axis size, flatness, star formation rate, mean star-formation-rate intensity, and peak star-formation-rate intensity for each LAE. Note that the SFR properties assume a continuum slope of $\beta = -1.5$. We expect the SFR to change by at most 30 percent for a typical range of β. The zero uncertainties are due to insignificant changes from one MCMC realisation to the other.

Name (SDSS)	m_{AB} [mag]	r_{maj} [kpc]	q	SFR [$M_\odot$ yr^{-1}]	$< \Sigma >$ [$M_\odot$ yr^{-1} kpc^{-2}]	Σ_{peak} [$M_\odot$ yr^{-1} kpc^{-2}]
J0029+2544	$27.05^{+0.22}_{-0.13}$	$0.410^{+0.040}_{-0.044}$	$0.57^{+0.05}_{-0.06}$	$0.96^{+0.12}_{-0.18}$	$3.33^{+0.54}_{-0.65}$	$30.85^{+3.11}_{-2.95}$
J0113+0250	$27.30^{+0.08}_{-0.06}$	$1.842^{+0.230}_{-0.321}$	$0.18^{+0.02}_{-0.01}$	$0.79^{+0.04}_{-0.06}$	$0.42^{+0.13}_{-0.04}$	$2.13^{+0.28}_{-0.24}$
J0237−0641	$28.18^{+0.11}_{-0.18}$	$0.224^{+0.012}_{-0.011}$	$0.81^{+0.02}_{-0.02}$	$0.32^{+0.06}_{-0.02}$	$2.50^{+0.08}_{-0.03}$	$4.22^{+0.11}_{-0.09}$
J0742+3341	$26.40^{+0.06}_{-0.03}$	$0.556^{+0.011}_{-0.010}$	$0.50^{+0.01}_{-0.03}$	$1.70^{+0.05}_{-0.10}$	$3.48^{+0.02}_{-0.09}$	$13.46^{+0.23}_{-1.40}$
J0856+2010	$27.30^{+0.03}_{-0.01}$	$0.242^{+0.002}_{-0.012}$	$0.58^{+0.01}_{-0.01}$	$0.71^{+0.00}_{-0.02}$	$6.69^{+0.38}_{-0.05}$	$11.54^{+0.21}_{-0.05}$
J0918+4518	$25.37^{+0.04}_{-0.02}$	$0.460^{+0.013}_{-0.008}$	$0.91^{+0.02}_{-0.04}$	$4.25^{+0.11}_{-0.15}$	$6.96^{+0.16}_{-0.12}$	$19.07^{+0.43}_{-0.44}$
J0918+5104	$25.94^{+0.02}_{-0.02}$	$0.372^{+0.005}_{-0.004}$	$0.66^{+0.01}_{-0.01}$	$2.63^{+0.06}_{-0.06}$	$9.21^{+0.09}_{-0.13}$	$54.10^{+0.52}_{-0.30}$
J1110+2808	$26.67^{+0.02}_{-0.01}$	$0.960^{+0.010}_{-0.017}$	$0.20^{+0.01}_{-0.01}$	$1.34^{+0.02}_{-0.02}$	$2.35^{+0.03}_{-0.05}$	$7.43^{+0.17}_{-0.13}$
J1110+3649	$25.57^{+0.02}_{-0.05}$	$1.520^{+0.032}_{-0.016}$	$0.31^{+0.01}_{-0.00}$	$3.79^{+0.21}_{-0.08}$	$1.69^{+0.01}_{-0.01}$	$8.94^{+0.15}_{-0.15}$
J1141+2216	$25.70^{+0.05}_{-0.03}$	$0.633^{+0.019}_{-0.021}$	$0.43^{+0.01}_{-0.01}$	$3.57^{+0.15}_{-0.16}$	$6.55^{+0.05}_{-0.07}$	$22.24^{+0.11}_{-0.05}$
J1201+4743	$25.36^{+0.01}_{-0.02}$	$1.067^{+0.014}_{-0.012}$	$0.55^{+0.01}_{-0.02}$	$4.09^{+0.08}_{-0.04}$	$2.09^{+0.03}_{-0.03}$	$6.81^{+0.42}_{-0.10}$
J1226+5457A	$27.66^{+0.03}_{-0.06}$	$0.575^{+0.017}_{-0.010}$	$0.49^{+0.00}_{-0.06}$	$0.58^{+0.04}_{-0.01}$	$1.15^{+0.22}_{-0.01}$	$7.22^{+0.21}_{-0.08}$
J1226+5457B	$27.83^{+0.03}_{-0.06}$	$0.242^{+0.009}_{-0.005}$	$0.76^{+0.01}_{-0.01}$	$0.50^{+0.03}_{-0.01}$	$3.55^{+0.04}_{-0.04}$	$6.79^{+0.07}_{-0.06}$
J1529+4015	$24.77^{+0.02}_{-0.02}$	$0.567^{+0.011}_{-0.006}$	$0.48^{+0.01}_{-0.01}$	$8.50^{+0.17}_{-0.19}$	$17.57^{+0.19}_{-0.13}$	$39.36^{+0.59}_{-0.38}$
J2228+1205	$26.66^{+0.03}_{-0.03}$	$0.279^{+0.014}_{-0.006}$	$0.49^{+0.01}_{-0.02}$	$1.50^{+0.04}_{-0.04}$	$12.41^{+0.21}_{-0.28}$	$24.69^{+0.77}_{-0.24}$
J2342−0120	$27.71^{+0.05}_{-0.02}$	$0.866^{+0.002}_{-0.003}$	$0.34^{+0.00}_{-0.00}$	$0.49^{+0.01}_{-0.02}$	$0.62^{+0.01}_{-0.03}$	$4.68^{+0.04}_{-0.28}$
mean	$26.13^{+0.06}_{-0.05}$	$0.649^{+0.028}_{-0.032}$	$0.48^{+0.01}_{-0.02}$	$0.86^{+0.07}_{-0.08}$	$2.04^{+0.13}_{-0.11}$	$10.54^{+0.45}_{-0.44}$
median	$26.66^{+0.35}_{-0.03}$	$0.561^{+0.013}_{-0.110}$	$0.51^{+0.01}_{-0.01}$	$1.37^{+0.06}_{-0.07}$	$3.51^{+0.07}_{-0.05}$	$10.1^{+0.45}_{-0.44}$

with an estimated merger fraction of just 10 to 30 percent, and so direct mergers are not thought to be the dominant mechanism for triggering star-formation in these galaxies (Shibuya et al. 2014). From our reconstructed surface brightness distributions, we find that in more than half of the cases, the UV-continuum emission is made up of multiple compact components. Therefore, even if there is a well defined size for the H II regions within LAEs, there are multiple sites of star-formation that would appear to be a single marginally resolved component if these were non-lensed cases. Unfortunately, as we do not have resolved kinematic information, it is not possible to determine if these connected multiple components are part of a merging system or not (although, as we argue below, we believe that except for a few cases, they are part of disk systems, as opposed to kinematically independent components). However, we do find that one to two sources out of sixteen in our sample also show evidence of compact components that appear unconnected and are separated by up to 4 kpc, which is consistent with the observed merger rate of non-lensed LAEs.

The gravitational lensing magnification provides higher intrinsic resolution for our reconstructed sources, and we find that the sample has a median size of 561^{+13}_{-110} pc, which is comparable to the lower limit on the size of the non-lensed samples of LAEs studied so far. However, we find that six sources in our sample have sizes below 0.5 kpc. The results from our analysis of the size scale of the UV-continuum are also consistent with the findings from studies of other lensed LAEs at high redshift, albeit with much smaller sample sizes. For example, Leclercq et al. (2017), expanding the sample analysed by Wisotzki et al. (2016), have found the minumim and maximum exponential scale-length of the UV continuum to be 0.11 kpc and 1.58 kpc respectively, in agreement with what previously found by Wisotzki et al. (2016) for the smaller sample. Patrício et al. (2016) carried out an analysis of a lensed star-forming galaxy at $z = 3.5$ and estimated a size of 0.34 kpc for the UV-continuum. Unfortunately, we cannot directly compare our results with theirs as we have used a different definition of size. This suggests that previous studies of non-lensed LAEs may have been biased by the angular resolution of the data and therefore it is not clear whether there really is limited size evolution with redshift for the UV-continuum emission of LAEs.

The size and structure of the UV-continuum is also thought to be related to the observed Lyman-α emission in these galaxies. Overall, there is evidence that the Lyman-α is more extended than the UV-continuum by factors of a few, and there is evidence for Lyman-α haloes that are both offset from the UV-continuum and extended by a few to 10 kpc (Momose et al. 2014). For example, Leclercq et al. (2017) found that Lyman-α haloes have sizes from 4 to 20 times bigger than the UV continuum scale-length, with a median size ratio of 10.8, in agreement with Wisotzki et al. (2016). The implications for this are that either the surface brightness of any extended UV-continuum is too low to be detected, relative to the Lyα, or that the compact star-forming regions traced by the UV-continuum are ionising the surrounding gas up to several kpc away. Detecting any low surface brightness continuum emission would also determine whether there is diffuse ongoing star-formation over a larger extent than thought, as opposed to there being a few compact regions of intense star-formation that may or not be related to the Lyman-α sources; the latter would again suggest that the star-forming galaxy and the LAE are independent systems that are interacting. Again, our reconstructed surface brightness distributions show compact and diffuse (and lower surface brightness) UV-emission, which would favour the

interpretation that we are observing extended star-forming galaxies with multiple compact H II regions that are ionising the surrounding gas and therefore Lyman Continuum Leakers. This result is in agreement with what found by Wisotzki et al. (2016), Hashimoto et al. (2017) and Leclercq et al. (2017). Resolved imaging of the Lyman-α emission will be needed to confirm this conclusion.

Also, it has been suggested that the Lyman-α equivalent width (EW) is connected to the morphology and size of the UV-continuum, with more optically compact LAEs having a much larger EW (Law et al. 2012). This has been interpreted as evidence for the galaxy morphology having an impact on whether Lyman-α is produced and whether it is able to escape from the host galaxy inter-galactic medium. However, it has also been reported that there is no correlation between the half-light radius and the EW (Wisotzki et al. 2016; Hashimoto et al. 2017; Leclercq et al. 2017), which may be due to the LAEs having a diverse set of host galaxy properties (Bond et al. 2012), or from the observational biases associated with narrowband observations of the EW from such compact sources (Oyarzún et al. 2017). There is also evidence for an anti-correlation between the ellipticity of the UV-continuum and the EW (Shibuya et al. 2014), and a correlation between the ellipticity and size of the UV-continuum and the detection of Lyman-α (Kobayashi et al. 2016; Hagen et al. 2016).

The implication of such observations is that the Lyman-α escape fraction is not a function of the ellipticity, and hence, the inclination angle of the star-forming disk, contrary to radiative transfer models in hydrodynamical galaxy formation simulations that predict an anisotropic escape path for the Lyman-α (Verhamme et al. 2012). Such models require the line-of-sight through the star-forming disk to be optically thick, with the Lyman-α emission being preferentially seen perpendicular to the star-forming disk (i.e. face-on objects that are characterised with a low ellipticity). Instead, the current observational data for non-lensed samples of LAEs favour a clumpy model for the star-forming regions, where the sight-lines for Lyman-α to escape are distributed randomly within a galaxy (Gronke & Dijkstra 2014). Therefore the importance of ellipticity for the Lyman-α escape fraction is still unclear and debated, with the data suggesting the absence of any correlation among the two.

The morphology of our reconstructed LAEs support the results found at lower angular resolution for the non-lensed samples. There is a clear positive correlation between the size and the ellipticity of the UV-continuum emission (see Fig. 2.7), at least for $\epsilon > 0.2$. In addition, the sources are also found to be highly elliptical, with more than half of the sample having axis-ratios less than 0.6, which is consistent with disk-like morphologies. Therefore, our data are consistent with the expectations from the clumpy model for the Lyman-α escape sight-lines. Unfortunately, there is no available imaging for the full Lyman-α emission for this sample. Therefore, we cannot currently measure the total Lyman$-\alpha$ fluxes and EWs, without making assumptions on the spectral slope and the total extension of the Lyman-α relative to the continuum.

2.5.2 Star formation rate

Many efforts have been made to estimate the SFR intensities of LAEs at different redshifts, as this is needed to understand their role in the build up of galaxies over cosmic time. Several samples consisting of hundreds of LAEs at $z \sim 2$ to 4 have been analysed via stacking methods, finding a

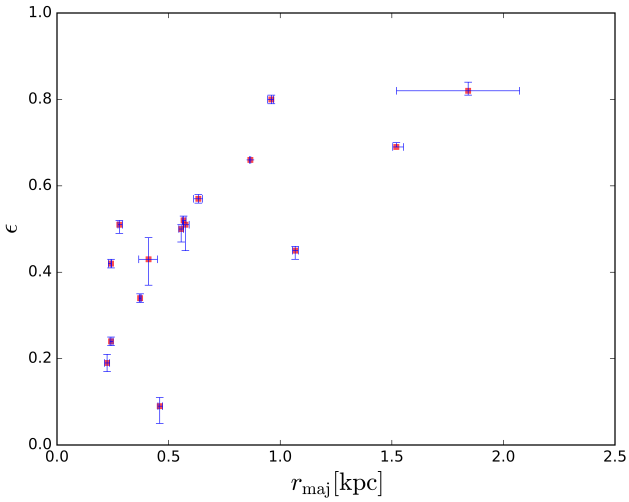

Figure 2.7: The size of the reconstrcuted sources in the sample against their ellipticity ($\epsilon = 1 - q$, where q is reported in Table 2.6).

range of SFR of 1.5 up to 11 $M_\odot$ yr^{-1} based on the luminosity of the UV-continuum of various samples (Blanc et al. 2011; Nakajima et al. 2012; Alavi et al. 2014; Kusakabe et al. 2015). The largest uncertainty in these analyses is determining the dust extinction, which requires multiple broad band filters to measure the reddening and is also sensitive to the assumptions about the extinction law for these galaxies, although the effect of dust is expected to decrease substantially for $z > 2$ (Smith et al. 2018). However, it is expected that the reddening is between $E(B-V) = 0$ to 0.5 (Blanc et al. 2011; Matthee et al. 2016), with a typical attenuation of about 3 for $\beta = -1.5$ and assuming a Calzetti et al. (2000) extinction law. For consistency, we compare our results to the non-dust corrected SFRs of these samples of non-lensed LAEs, but they are likely around 3 times higher than stated here when the dust attenuation is taken into account.

Overall, we find that the median SFR of the galaxies in the lensed sample of LAEs studied here is lower, but certainly comparable, to those obtained from the stacking techniques, with a median SFR of 1.4 $M_\odot$ yr^{-1}. Such stacking methods can be biased by outliers, however, we find that from the direct measurement of the SFR of individual lensed galaxies that the median SFR is similar and therefore, the stacking methods are likely tracing the general properties of LAEs.

2.6 Conclusions

We have analysed the first statistically significant sample of LAEs at $z \sim 2.5$ that are gravitationally lensed by massive foreground galaxies at $z \sim 0.5$. By studying LAEs that are intrinsically extended, the gravitational lensing signature typically consists of extended arcs and Einstein rings, which give a large number of constraints to the lensing mass model and allow the effect of the PSF to be de-convolved and the intrinsic source structures to be obtained.

We have modelled the gravitational potential of all of the systems in the sample using a

power-law mass distribution and an external shear, with additional small-scale corrections to the potential where required, and simultaneously inferred the surface brightness distribution for the lensing galaxies. This modelling is more sophisticated than has been carried out so far and provides the most robust inferences of the reconstructed sources. We have found that most of the deflectors are well described by a power-law mass-density profile, which is close to being isothermal with $< \gamma' >= 2.00 \pm 0.01$. Except for a few cases where significant residuals are present in correspondence of the lensing galaxy, the light distribution is well represented by one or two Sérsic components. All of our models, except for a few peaks in the brightness of the lensed images, have residuals which are at the noise level. Most of our lens-mass models agree with those reported by S16, but often present a lower level of image residuals, which in part is likely due to the way the source is solved for with our technique, but is also due to subtle differences in the lens macro-model.

We have studied the intrinsic properties of the UV-continuum of the reconstructed LAEs at $z \sim 2.5$, finding that they have a median integrated SFR of $1.4^{+0.06}_{-0.07}$ $M_\odot$ yr^{-1} and a peak SFR intensity between 2.1 to 54.1 $M_\odot$ yr^{-1} kpc^{-2}. These galaxies are quite compact with a range of radii from 0.2 to 1.8 kpc and a median size of 561^{+13}_{-110} pc (semi-major axis), and complex morphologies with several compact and diffuse components separated by 0.4 to 4 kpc (see also Cornachione et al. 2018). Our lower limit to the intrinsic size is about a factor of two smaller than that found for non-lensed LAEs, which highlights the power of gravitational lensing and sophisticated lens modelling techniques for resolving such objects in the high redshift Universe. Most importantly, we find that the LAEs are quite elliptical, with a median axial-ratio of 0.51 ± 0.01. This morphology is consistent with disk-like structures of star-formation for 76 percent of the sample, which would rule out models where the Lyman-α emission is only seen perpendicular to the disk, and favours those clumpy models for the escape lines-of-sight for Lyα. This is in agreement with the results for non-lensed LAEs studied at similar redshifts, but is more robust given the improved angular resolution of the our analysis. We also find that 14 percent of the sample have off-axis components that may be associated with mergers, which is again consistent with the analysis of non-lensed LAEs. Overall, the morphologies of the LAEs in our sample agree quite well with the results in the literature, where the effective angular resolution is less and stacking techniques are needed.

Resolved kinematical information will be needed to confirm the disk-like nature and possible merger scenario for the LAEs in the sample, and to study the distribution of the ionised gas with respect to the UV-continuum sources. Such observations will also allow a robust resolved study of the Lyman-α escape fraction for these objects, as the current low resolution data from SDSS are limited by slit-losses. Also, as the UV-continuum and the Lyman-α are expected to be offset, it is not possible to use the magnifications derived here to probe the intrinsic luminosity of the Lyman-α emission. Generally, our analysis further demonstrates gravitational lensing as a powerful tool to analyse and resolve the detailed structure of high-redshift galaxies, allowing the study of their physical and morphological properties at a resolution otherwise only achievable with nearby targets.

Chapter 3

On the recoverability of complex mass and source brightness distributions with gravitational lensing

To be submitted to MNRAS as:
Ritondale, E., Vegetti S., McKean J. P., Auger, M. W., Rizzo F. (in prep), 'On the recoverability of complex mass and source brightness distributions with gravitational lensing'.

3.1 Introduction

Strong gravitational lensing is a powerful tool with a diverse set of cosmological and astrophysical applications. In recent years, it has been used for many purposes, such as studying the baryonic and dark matter distribution in galaxies (e.g. Treu & Koopmans 2002; Oldham & Auger 2018) and galaxy clusters (e.g. Postman et al. 2012; Zitrin et al. 2011), investigate the resolved properties of high-redshift galaxies (e.g. Leethochawalit et al. 2016; Patrício et al. 2016; Ritondale et al. 2019a), measure the Hubble constant (e.g. Suyu et al. 2017), as well as to map the dark matter distribution on sub-galactic scales (Dalal & Kochanek 2002b; Vegetti et al. 2010b, 2012; Nierenberg et al. 2014; Hezaveh et al. 2016; Vegetti et al. 2018; Ritondale et al. 2019b).

However, all of these analyzes require a precise modelling of the central lensing potential. Most often, at galaxy scales, the main gravitational lens is described by a single elliptical power-law mass density distribution with the contribution of an external shear component (however, see Saha & Williams 2004 for a complete model-free approach and Nightingale et al. 2018 for a decomposed mass model). Indeed, Koopmans et al. (2006) and Auger et al. (2010) have shown that the large sample of lens galaxies from the Sloan Lens ACS Survey (SLACS) have an average mass density profile that is nearly consistent with, although slightly steeper than, an isothermal mass distribution.

Mao & Schneider (1998) were the first to suggest that departures from simple assumptions on the macro-model, as revealed by the presence of flux-ratio and astrometric anomalies in gravitationally lensed quasars, could be related to the presence of a significant population of dark-matter

subhaloes. Later on, Chiba (2002), Xu et al. (2009); Xu et al. (2010), He et al. (2017), Li et al. (2017) and Despali et al. (2018) have extended this concept, and quantified the relative lensing effect (on the multiple images of both lensed quasars and galaxies) of dark-matter subhaloes, globular clusters, luminous dwarf satellites and dark-matter haloes along the line of sight. From these studies, it was concluded that line-of-sight haloes and subhaloes within the main lens are the dominant sources of astrometric and flux-ratio anomalies, though Xu et al. (2015) pointed out that stellar structures in the lensing galaxies could also be the cause of large flux-ratio anomalies. Looking at the effect of structures at larger scales, Möller et al. (2003) and Quadri et al. (2003) have studied the influence of disc-like mass components on the flux ratios of multiply imaged quasars and concluded that their observational signatures are not negligible, and measurably affect 10 to 30 per cent of lenses that produce quadruply-imaged quasars. Similarly, Hsueh et al. (2016, 2017) have shown that the observed flux-ratio anomaly of the lensed radio-sources CLASS B1555+375 and CLASS B0712+472, which had been attributed to a significant fraction of dark matter subhaloes, can instead be largely explained by the gravitational effect of a previously unmodelled edge-on disc. From an analysis of the Illustris simulation (Vogelsberger et al. 2014), Hsueh et al. (2018) found that because of baryonic structures and discs, the probability of finding large flux-ratio anomalies increases to about 8 per cent for early-type lenses and to between 10 to 20 per cent for late-type lenses. They have also found that baryonic effects induce astrometric anomalies in 13 per cent of the mock lenses studied. Gilman et al. (2017) have obtained a similar result from the analysis of simulated lens systems, based on *Hubble Space Telescope* (*HST*) observations of low-redshift galaxies. These studies indicate the importance of deep-imaging observations and detailed lens modelling for a correct quantification of dark matter (sub)structure.

So far, most analyzes of realistic lensing potentials have mainly focused on the effect of observed features in the stellar mass distribution, such as discs, which can be revealed by deep imaging observations. However, a study of an elliptical galaxy produced by *N*-body simulations of galaxy mergers has also identified low level perturbations to the overall mass model that cannot be reproduced by a simple smooth elliptical power-law mass distribution (Barnabè et al. 2009). Therefore, smaller-scale mass structures within the main lens will also effect the overall structure of the observed lensed images. In this chapter, we present the example of SDSS J0755+3445, where the complexity of the lensing potential is detected via a pixellated gravitational imaging technique (Vegetti & Koopmans 2009). In particular, we detect the presence of a non-visible extra mass component, whose nature is at present unclear, but may be related to the formation history of the main lens or a complex line of sight. We find that a failure to take this extra mass component into account as part of the lens model can lead to an overestimation of the number of dark matter subhaloes detected from this system, and prevent the correct reconstruction of the background source surface-brightness distribution and the derived physical properties.

The chapter is organized as follows. In Section 3.2, we briefly describe the *HST* imaging data for SDSS J0755+3445 that we used for our analysis. In Section 3.3, we present the results of the lens modelling with increasing macro-model complexity, and its implication on the inference of subhaloes and the derived source properties. Our results are then discussed and summarized in Section 3.4.

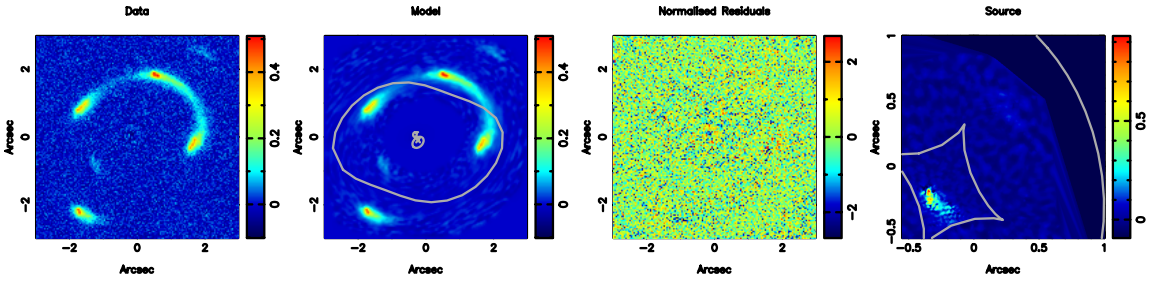

Figure 3.1: *HST* WFC3-UVIS F606W imaging of SDSS J0755+3445, showing the main lensing galaxy at $z_l = 0.722$ in the centre and the extended four images of the LAE at $z_s = 2.634$, and a faint doubly-imaged component.

3.2 Data

SDSS J0755+3445 is a Lyα emitting galaxy (LAE) at $z_s = 2.634$ that is gravitationally lensed by a massive foreground lensing galaxy at $z_l = 0.722$. The system was found as part of the BELLS–GALLERY survey (Shu et al. 2016a), which consisted of twenty-one LAEs that were likely to be gravitationally lensed by massive foreground ellipticals. This sample was observed with the *HST* (GO: 14189; PI: Bolton) using the WFC3-UVIS camera and the F606W filter. Out of the twenty-one candidates, seventeen have been confirmed as genuine strong gravitational lens systems with a clear classification of the deflector morphology. These systems were independently modelled by Shu et al. (2016b) and Ritondale et al. (2019a) (see Chapter 2), using a variety of lens and source parameterizations. An inference of the properties of dark-matter from the same sample was presented by Ritondale et al. (2019b) and in Chapter 4. It is from this latter analysis that the peculiar mass properties of the lensing potential for SDSS J0755+3445 were first identified, which we investigate in detail here.

The data for SDSS J0755+3445 were retrieved from the *HST* archive and processed using the ASTRODRIZZLE task that is part of the DRIZZLEPAC package. The resulting image for the system is presented in Fig. 3.1, which shows the main lensing galaxy at the centre, as well as the four extended images of the LAE and a fainter doubly-imaged component. The similar maximum image separation between the quadruply and doubly imaged sources implies that they are at the same redshift. In addition, there are two galaxies to the north- and south-west of the main lensing galaxy. There is currently no redshift information for these objects.

3.3 Lens modelling and source reconstruction

In this section, we investigate mass models with increasing complexity for SDSS J0755+3445, and quantify the implications that these mass models have on our ability to detect low mass subhaloes within the lens and haloes along the line of sight, and on our ability to characterize the

properties of the reconstructed source.

3.3.1 The lens models

In this subsection, we describe the main results of this analysis and the steps that have led to the gravitational detection of an otherwise unobserved extended and complex mass distribution. The gravitational lens mass modelling was carried out with an updated version of the lens modelling code developed by Vegetti & Koopmans (2009). We refer to Ritondale et al. (2019a) and Chapter 2 for a detailed description of the new features of the method and Vegetti & Koopmans (2009) for the original technique. We have modelled the data under several assumptions for the lens galaxy mass distribution, where the underlying elliptical power-law model is described as,

$$\kappa(x, y) = \frac{\kappa_0 \left(2 - \frac{\gamma}{2}\right) q^{\gamma - 3/2}}{2 \left(q^2 \left(x^2 + r_c^2\right) + y^2\right)^{(\gamma-1)/2}}. \tag{3.1}$$

Here, $\kappa(x, y)$ is the surface mass density at position x and y, κ_0 is the normalization of the surface mass density, γ is the radial mass-density slope, q is the axis ratio and r_c is the core-radius. In addition, the standard parametric model has an external shear component given by Γ at a position angle of Γ_θ. The parameters for the various lens models tested here are presented in Table 3.1.

An elliptical power-law with an external shear

As a first step, we have modelled the data assuming a single elliptical power-law model plus an external shear for the lens mass distribution and one Sérsic component for its light distribution. This assumption is a standard one for the description of galaxy-scale strong gravitational lenses. We refer to this model as Model I for the rest of the chapter. Here, both the quadruply and doubly imaged source components are modelled simultaneously with a single source regularization constant (e.g., see Vegetti & Koopmans 2009). The details of the reconstruction are given in Ritondale et al. (2019a), but to summarise, we have found the observed morphology of the lensed emission to be well described by a lensing mass distribution with a power-law slope of $\gamma = 1.86 \pm 0.01$ and a significant external shear component of strength $\Gamma = 0.232 \pm 0.001$ that is orientated in the south-west direction towards a massive, luminous galaxy (see Fig. 3.1). We note that the power-law slope is at the shallow end of the distribution for massive elliptical lensing galaxies and that the shear is very large (e.g. Koopmans et al. 2009), both of which indicate that the mass distribution of lens may be complex. In addition, the model is highly elliptical, with an axis-ratio of $q = 0.531 \pm 0.002$, but with a position angle that is around 75 deg from that of the shear position angle, suggesting a boxy mass distribution for the lens.

As can be seen from Fig. 3.2, this model provides a good description of the data, with minimal normalized image residuals. However, we also see that this model leads to a source for the quadruply imaged component that has an extended low surface-brightness tail with a positive and negative brightness, which indicates an under-focusing in the source-plane (i.e., the model does not properly converge the observed image-plane surface brightness to the same location in the source plane). From Fig. 3.3 it is also evident that the size of the source changes considerably

according to the contour levels we choose to compute its size. The positive and negative beating of the tail is the part of the source that is much more extended when considering negative contours and it is therefore the one responsible for its change in size. In fact, using contours set at 10 or 15 per cent of the peak brightness causes a difference in the computed size of 0.04 arcsec, on average, when using the same reconstruction method (see Fig. 3.3).

Two elliptical power-laws with an external shear for the main lens and the south-west galaxy

We have also explicitly included the galaxy to the south-west as an extra elliptical power-law mass component to investigate the cause of the large external shear, which we refer to as Model II. Again, including nearby galaxies as parametric models, such as the elliptical power-law model considered here, is a standard method for taking the contribution of any complexity in the environment into account. We find that including the second mass component in this way has only a minor effect on the mass distribution of the main lens. The mass density profile becomes steeper by about 8 percent, to $\gamma = 1.98 \pm 0.01$ as the mass distribution is now able to be more centrally concentrated. A similar result was recently reported for the main lensing galaxy in the gravitational lens system MG J0751+2716, when additional confirmed group members were taken into account (Spingola et al. 2018). We note that the mass density profile of the second mass component is super-iothermal, with $\gamma = 2.52 \pm 0.01$, which is likely not physical. The overall mass ellipticity of the main lens and the external shear remain high ($q = 0.457 \pm 0.002$ and $\Gamma = 0.185 \pm 0.001$). Therefore, adding the second mass component to the south-west does not result in a more realistic mass model for the main lens. In addition, the resulting source surface brightness distribution (not shown here) does not improve from that found for Model I. Therefore, the contribution to the lensing potential given by the south-west galaxy does not have any significant effect on the quality of the lens model and the morphology of the source, when it is included as a secondary elliptical power-law mass model.

An elliptical power-law with an external shear and pixellated potential corrections

As a third step, we have modelled the data as an elliptical power-law with an external shear, but we now apply the *gravitational imaging* technique. We refer to Vegetti & Koopmans (2009), Ritondale et al. (2019b) and Chapter 4 for a more detailed description of this method. Briefly, this technique allows for extra complexity in the lensing mass distribution by introducing pixellated and regularized potential corrections to the otherwise smooth underlying mass model. The technique was initially developed by Vegetti & Koopmans (2009) to detect subhaloes within the main lensing potential. However, thanks to its agnostic nature, it allows us to capture any general departure from our parametric assumption on the lens macro-model, independent of its nature (e.g. Barnabè et al. 2009). For this, we have kept the parameters for the elliptical power-law with an external shear model from Model I fixed, and added the potential corrections to the data.

The resulting mass model is presented in Fig. 3.4, where we see that for the specific case of SDSS J0755+3445, the gravitational imaging analysis does not lead to a localized positive peak in the convergence map (the signature of a subhalo; e.g. Vegetti et al. 2010a,b, 2012), but

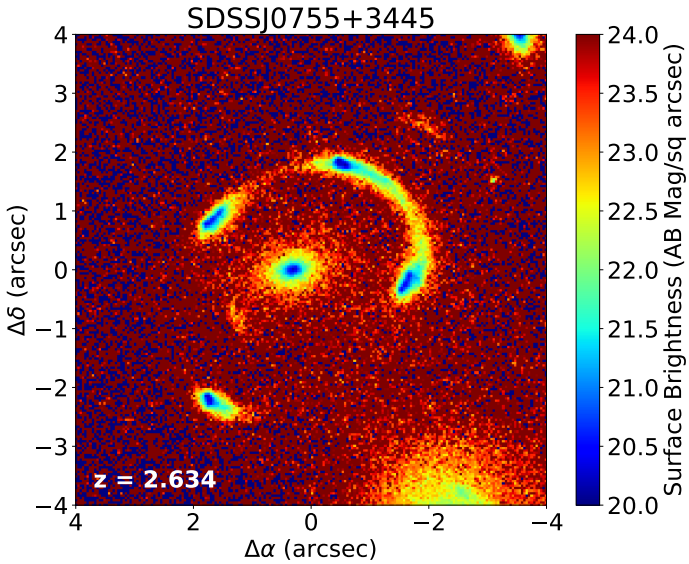

Figure 3.2: The mass model and source reconstruction for an elliptical power-law mass distribution with an external shear. From left to right, the input *HST* WFC-UVIS F606W imaging data (with the lensing galaxy light subtracted for clarity), the reconstructed model for the lens-plane surface brightness distribution, the normalized image residuals in units of σ, and the reconstructed surface brightness distribution of the LAE galaxy. Critical curves and caustics are plotted in grey for the lens- and source-plane, respectively.

rather a diffuse correction spread across the lens plane, with a strong negative component in the potential and convergence maps to the south-west of the lensed images. This analysis reveals the presence of a complex mass distribution that is not fully captured when a single elliptical power-law plus an external shear mass model is used, but that is also unlikely to be due to localized perturbations from subhaloes within the lens or haloes along the line of sight. Given the position and strength of the large negative component, we find that this is most likely due to the secondary galaxy towards the south not being correctly accounted for by the simple parametric model. Interestingly, this significantly affects the inferred morphology of the background source, which is now more focused and has a less pronounced tail [see Fig. 3.3, panels (a) and (d)], and significantly improves the normalized residuals, which are now at the noise level (see Fig. 3.4).

Separated image sets

To further investigate the nature of the diffuse positive density component seen in Fig. 3.4, we have modelled the two sets of lensed sources in the data independently, each with a single elliptical power-law plus an external shear mass distribution and their own source regularization. We call this Model IV. This choice is motivated by the relatively large radius probed by the fainter doubly-imaged source and the independent information that is provided by having two sets of lensed images. We find that the lens model parameters are almost equivalent to those of Model I, for both datasets. However, the power-law slope changes from a shallower value of

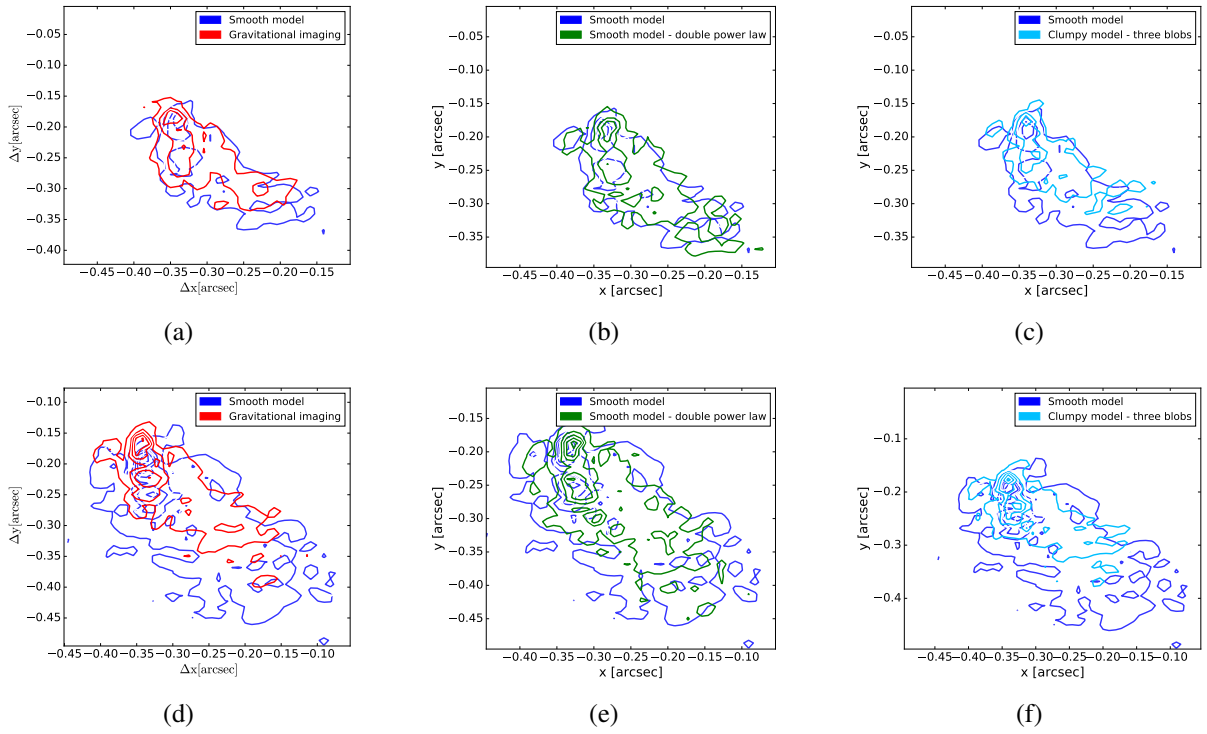

Figure 3.3: Reconstructed source surface brightness distributions for SDSS J0755+3445 from different types of mass modelling. The upper row shows the 10 per cent peak brightness iso-contours while the bottom row shows the 15 per cent peak brightness iso-contours of the respective reconstructed sources. In each panel the contours increase by a factor of 2. In all of the panels, the blue contours show the source structure inferred under the assumption of a single elliptical power-law mass distribution for the lensing galaxy with an external shear. For panels (a) and (d), the red contours show the reconstructed source when low-level diffuse pixellated potential corrections are added to the single elliptical power-law model with an external shear. For panels (b) and (e), the green contours show the reconstructed source when we use a double elliptical power-law model with an external shear. For panels (c) and (f), the light blue contours show the reconstructed source when three analytical clumps are added to the single elliptical power-law model with an external shear.

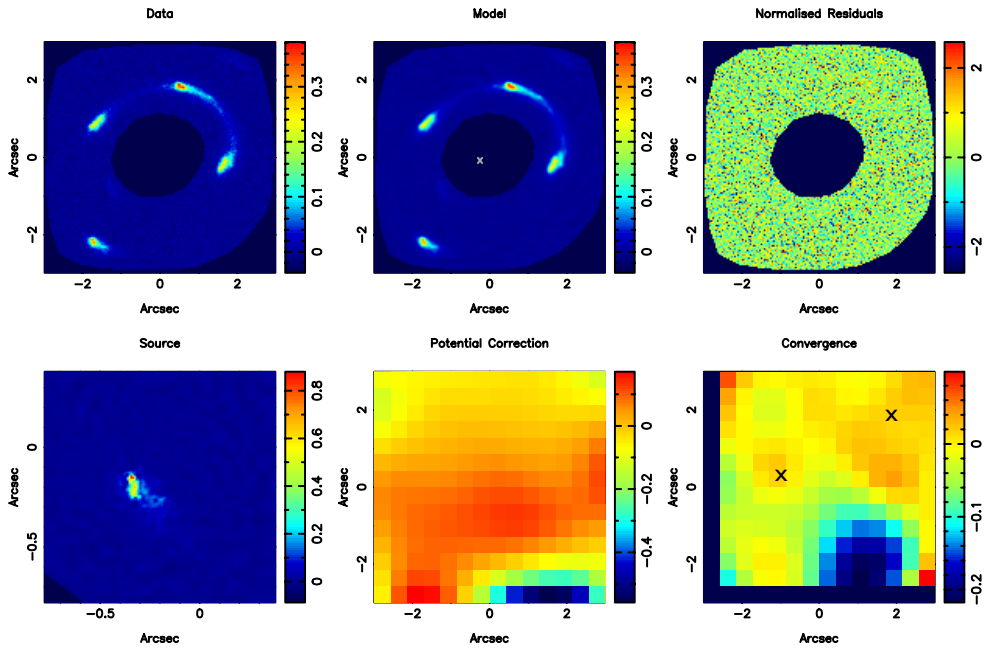

Figure 3.4: The mass model and source reconstruction for an elliptical power-law mass distribution with an external shear and including pixellated potential corrections. From left to right, (upper) the input *HST* WFC-UVIS F606W imaging data (with the lensing galaxy light subtracted and masked for clarity), the reconstructed model for the lens-plane surface brightness distribution, the normalized image residuals in units of σ, (lower) the reconstructed surface brightness distribution of the LAE galaxy, the pixellated potential corrections and the resulting convergence map (the Laplacian of the potential corrections). The position of the lensing galaxy is given by the grey $\times$ and the positions of the parametric subhaloes are given by the black $\times$.

$\gamma_q = 1.84 \pm 0.01$ for the set of quadruple images, to a steeper one of $\gamma_d = 2.08 \pm 0.03$ when only the fainter double set of images are used.

A double elliptical power-law with an external shear

Based on the results from Model IV, we then modelled both the quadruply and doubly lensed-images simultaneously, as in Model I, but now we use two elliptical power-law mass components to provide additional complexity, which we call Model V. As above, all of the model parameters are left free, although we start with an initial guess where both elliptical power-law mass components are co-spatial, at the position of the main lensing galaxy. The best-fitting model is characterized by two power-laws with similar geometrical parameters, except for the mass normalisations and the mass-density slopes. These are $\kappa_{0,I} = 1.77 \pm 0.01$ and $\gamma_I = 1.82 \pm 0.01$ for the dominant mass component, and $\kappa_{0,II} = 0.071 \pm 0.004$ and $\gamma_{II} = 2.02 \pm 0.04$ for the secondary mass component, respectively. The main mass component is consistent within 5 per cent of the results found for Model I. Given that the mass normalization of the secondary mass component is so low, Model V essentially reduces to what has been found for Model I, and therefore, adding complexity with a double power-law model has no major effect.

To understand how the different reconstructed surface brightness distributions compare to each other, we compute the 10 and 15 percent isocontours of the pixellated source surface brightness reconstructed with the best fitting models, as above. The contours of the double power-law reconstructed source are shown in green in panels (b) and (e) of Fig. 3.3. We find that the source is less extended than in the case that used a single elliptical power-law model (blue contours). Nevertheless, the tail is still more pronounced than for the source inferred from the gravitational imaging analysis, whose contours are shown in red in panels (a) and (d) of Fig. 3.3. This suggests that a more complex model allows for a better fit to the data and a better representation of the underlying mass distribution causing the lensing, as would be expected. However, the best focused source was obtained when no assumption was made on the latter, that is, via the gravitational imaging methodology.

A test on the assumed source structure

In order to confirm that the required complexity in the mass model is not due to some simplistic assumptions on the source model, we attempted two different priors on the source surface brightness distribution other than the one based on a single Gaussian random field. To this end, we used the technique developed by Rizzo et al. (2018) to simultaneously model the two sets of images (quadruple and double) with the same mass model, but reconstructing them independently as two different source models. This allows for different levels of source regularization, which takes into account the different signal-to-noise ratios of the two sets of lensed images. For a detailed description of the technique, we refer to Rizzo et al. (2018). The modelling is performed using a smooth mass model (an elliptical power-law with an external shear; Model I). Moreover, we also attempted the source reconstruction using a different hyper-prior, where each source is described with a Sérsic component. None of these further tests significantly reduced the positive-negative beating in the smooth source and again, the underlying mass distribution

Table 3.1: The parameters of the different lens mass models tested during the analysis of SDSS J0755+3445. Note that for Model III, the model parameters are held fixed to those obtained from Model I and pixellated potential corrections are added using the gravitational imaging technique.

Model (number) Component	κ_0	θ	q	γ	Γ	Γ_θ
Single power law(I)	1.86 ± 0.01	104.94 ± 0.05	0.531 ± 0.002	1.83 ± 0.01	0.232 ± 0.001	30.18 ± 0.1
S-W galaxy included (II)						
main	1.92 ± 0.01	107.17 ± 0.14	0.457 ± 0.002	1.98 ± 0.01	0.185 ± 0.001	31.94 ± 0.2
S-W galaxy	1.29 ± 0.02	140.79 ± 0.05	0.970 ± 0.002	2.52 ± 0.01		
Separate images (IV)						
quad	1.86 ± 0.01	104.05 ± 0.14	0.521 ± 0.002	1.84 ± 0.01	0.235 ± 0.001	29.5 ± 0.2
double	2.04 ± 0.03	102.3 ± 1.9	0.52 ± 0.02	2.08 ± 0.03	0.23 ± 0.01	35.1 ± 1.4
Double power law (V)						
I	1.77 ± 0.01	104.12 ± 0.12	0.518 ± 0.002	1.82 ± 0.01	0.237 ± 0.001	29.5 ± 0.1
II	0.071 ± 0.004	112.7 ± 3.0	0.53 ± 0.02	2.02 ± 0.04		
3 blobs (VI)	1.82 ± 0.004	106.99 ± 0.05	0.572 ± 0.001	1.814 ± 0.002	0.218 ± 0.0004	31.7 ± 0.1

causing the lensing is not fully captured by these macromodel assumptions.

3.3.2 Implications for subhalo detection

Our analysis thus far has found that various forms of mass complexity in the lens macro-model does not result in a satisfactory fit for data that also results in a well-determined source structure, except when large-scale diffuse potential corrections are added to the a smooth elliptical power law (Model III). In the absence of the latter, it is commonly assumed that any deviation from a smooth model requires additional small-scale mass structure in the form of subhaloes. A widely used alternative approach to the gravitational imaging technique for the detection of subhaloes is to instead describe the extra mass components with analytical functions, where the mass and position are the only free parameters. These analytic subhaloes can be added as single or multiple objects to the mass model, where the significance can be quantified via a χ^2 term or the Bayesian evidence. The advantage of this approach, relative to the pixellated one from the gravitational imaging method, is that the number of degrees of freedom is significantly reduced, given the analytical form that is assumed for the subhaloes. One is then able to quickly explore the parameter space and compare different models (i.e. a smooth model with one that includes subhaloes). One disadvantage is that this method requires a priori assumptions on the number and shape of subhaloes. The other main disadvantage is that the only complexity added to the lensing potential is in the form of subhaloes, which may not be an accurate representation of the correction required, that is, when there is a galaxy-scale disc. The pixellated gravitational imaging technique, instead, allows for a more general mass structure that may or may not result in a localized correction that is only offered by including analytic subhaloes.

To test thus, we use the specific case of SDSS J0755+3445 to determine whether a purely analytical description of subhaloes is prone to false detections of subhaloes in the presence of complex mass components that are not explicitly accounted for. To this end, we focus on our best-fit single elliptical power-law model (ModelI). We then consider alternative models where an increasing number of subhaloes (1, 2 and 3), described as spherical NFW profiles (Navarro et al. 1997), are added to the lensing potential. The probability of these models relative to a model with no subhaloes is then quantified via $\sigma = \sqrt{2 \times \Delta \log \mathcal{E}}$, where the Bayes factor $\Delta \log \mathcal{E}$ is obtained by marginalizing over all model parameters. The latter include the macro model geometrical parameters, the external shear strength and position angle, level of regularization and the subhalo masses and positions.

We find that as the number of subhaloes increases, the Bayesian evidence also increases in favour of the clumpy models. For example, a clumpy model with only one subhalo is more probable than a model with no subhalo by a Bayes factor of $\Delta \log \mathcal{E} = 46$ (to first order corresponding to a 10σ difference), and models with two or three subhaloes have a Bayes factor of $\Delta \log \mathcal{E} = 104$ and $\Delta \log \mathcal{E} = 99$ (roughly a 14σ difference), respectively. We call the model with three sub-hales Model VI for reference. We also find that the inferred subhalo positions are such that they populate the region on the lens plane where the pixellated analysis found positive diffuse convergence corrections. Moreover, the source appears significantly more compact and with a less extended tail when compared to the source obtained with a single or double elliptical power-law model, as shown by the light blue contours in Fig. 3.3 (see panels c and f).

To further disentangle the effect of the different mass components found by adding pixellated potential corrections, we create two sets of mock data. Starting from the source reconstructed with the single power-law smooth model, we use the lensing equation to create two sets of new lensed data; the first containing the two subhaloes within the lens maximising the Bayesian evidence, and the second containing two line-of-sight haloes in the foreground and in the background of the main lens. The masses of the latter are rescaled according to the mass-redshift relation derived by Despali et al. (2018), which given the redshift and the mass of the subhaloes, determines the mass of the line-of-sight haloes causing an equivalent perturbation on the lensed images. The results of the gravitational imaging analysis on these mock data are shown in Fig. 3.4. The two panels show how different the potential corrections are depending on the nature of the mass component generating them. In particular, the difference among the convergence corrections due to small mass clumps and other underlying mass structure can be noticed comparing panels a and b with those seen Fig. 3.4.

Indeed, the consistency between the analytical and pixellated analysis regarding the perturber position (and mass) is one of the criteria introduced by Vegetti et al. (2014) to identify positive low-mass halo detections. Moreover, as already discussed by Vegetti et al. (2014), and as demonstrated more robustly here, the nature of the pixellated convergence corrections provides critical information in disentangling the presence of subhaloes (localized positive corrections, as in e.g. Vegetti et al. 2012) from extra complexity in the macro-model (e.g. diffuse corrections as shown for example in Fig. 3.4). In the specific case considered here, the underlying complexity of the mass distribution is clearly not fully represented by the standard assumptions that are usually made for lens galaxies (i.e. elliptical power-law mass distributions with analytical subhaloes). Deeper exposure data may provide important information to constrain its nature.

3.3.3 Implication for the analysis of lensed galaxies

One of the key applications of gravitational lensing is studying the high redshift Universe, and the robustness of such analyzes will be dependent on how well the distortions from the gravitational lens can be corrected for. Indeed, this is seen for the case of SDSS J0755+3445 by comparing the reconstructed source surface brightness distribution for the single and double elliptical power-law models investigated here, and for those that are more complex on smaller mass-scales (gravitational imaging and those with clumpy mass models), as shown in Fig. 3.3.

We quantify the impact of the macro-model reconstruction on the physical and morphological properties inferred for the background source by fitting ellipses and using the semi-major axis to quantify the size. Here, we consider the size for both the 10 and 15 per cent peak surface brightness contours, as shown in Fig. 3.3. For the source obtained via gravitational imaging, which is also the one including the highest level of complexity in the macro-model, we obtain a semi-major axis of $r_{\rm maj} = 1.1$ kpc and a star-formation rate of SFR $= 10$ M$_\odot$ yr^{-1}. The sources inferred from the single, and double elliptical power-law models, have a size that is 20 and 27 per cent larger than in the gravitational imaging case, respectively, and the estimated SFRs are higher by ~ 9 per cent. By adding three analytical clumps to the main smooth potential, we obtain a source with a size comparable to the gravitational imaging case, but the resulting SFR is a factor of 22 per cent lower. These results demonstrate the importance of accurately reproducing the

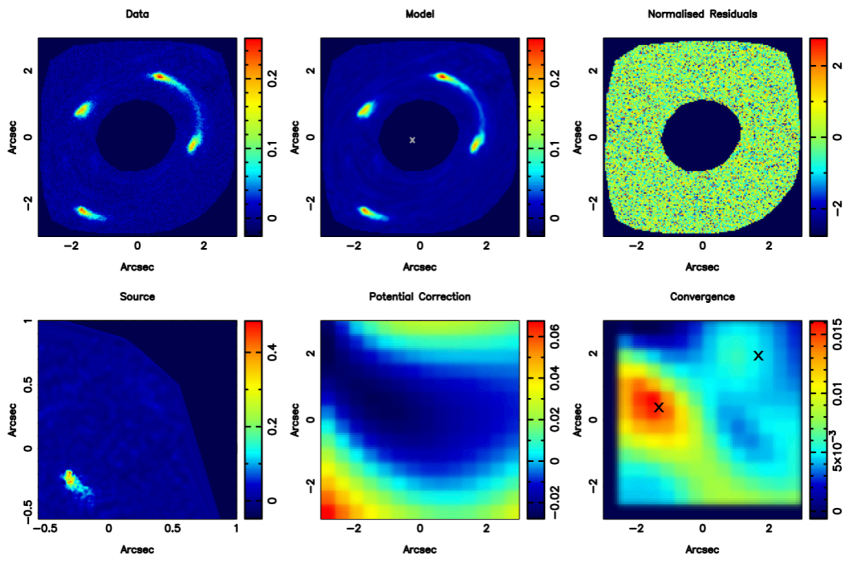

(a)

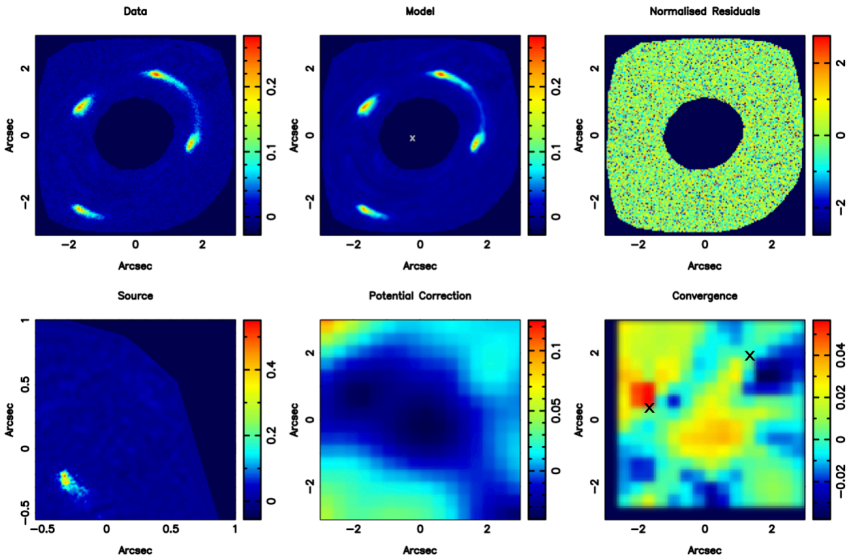

(b)

Figure 3.5: The results of the gravitational imaging analysis for two mock datasets with subhaloes within the lensing galaxy (panel a) and along the line of sight (panel b). From left to right, (upper) the input *HST* WFC-UVIS F606W imaging data (with the lensing galaxy light subtracted and masked for clarity), the reconstructed model for the lens-plane surface brightness distribution, the normalized image residuals in units of σ, (lower) the reconstructed surface brightness distribution of the LAE galaxy, the pixellated potential corrections and the resulting convergence map (the Laplacian of the potential corrections). The position of the lensing galaxy is given by the grey $\times$ and the positions of the parametric subhaloes are given by the black $\times$.

macro-model to infer the physical properties of lensed galaxies correctly.

3.4 Discussion & conclusions

We have tested models for the gravitational lens system SDSS J0755+3445 using different lens-galaxy mass distributions of increasing complexity. We have found that analytical parameterisations, both in the form of single and double elliptical power-law models, with an external shear component, lead to image residuals that are at the noise level. However, each of these models also result (at different levels) in an unfocused source morphology that is characterized by a long tail of positive and negative beating, which suggests a problem with the lens macro-model. When dark-matter subhaloes, in the form of spherical NFW mass components, are added to the main lensing potential, we find a significant statistical preference, which increases with the number of subhaloes that are included in the model. In fact, the Bayes factor is higher for a model that includes two subhaloes when the main lens is described by a single, rather than a double elliptical power-law model. However, a gravitational imaging analysis, in which linear pixellated potential corrections are added to the single elliptical power-law model, reveals the presence of a diffuse and complex mass distribution in addition to the assumed smooth model. The nature of this diffuse mass component is currently unclear and further multi-band observations will be needed to investigate its origin further. Interestingly, the inclusion of this additional structure results in a more realistic and better focused morphology for the background source, and the strongest peaks in the relative convergence corrections are located at the same positions inferred by including the NFW subhaloes.

Our findings indicate that complex mass structure can mimic the effect of subhaloes and lead to an overestimation of the abundance of low-mass structure; this can have an adverse effect in determining the properties of dark matter from this method. These results are in line with those obtained by Hsueh et al. (2016, 2017, 2018), who have shown that the inclusion of an inclined disc can explain the flux-ratio anomalies in the gravitational lens systems CLASS B0712+472 and CLASS B1555+375, without the need for additional dark subhaloes, and who also found from simulations that in 13 per cent of the cases, baryonic effects can cause astrometric anomalies in an analogous way to low-mass dark-matter haloes. Our results further confirm that by considering low-mass haloes to be the only explanation for observed astrometric and flux-ratio anomalies could be misleading and eventually lead to false detections (see also the discussion by Ritondale et al. 2019b in the cases of low signal-to-noise data). While deep-imaging observations may provide important clues on the properties of the macro-model, these are not always available. Therefore, alternative explanations should be taken into account and explicitly tested to determine the actual cause of the observed anomalies. In this respect, the gravitational imaging technique with its pixellated corrections represents an independent test to address this issue, though other parametrisations are certainly possible.

Finally, we have shown that a sound knowledge of the lensing potential is fundamental not only to make a proper inference on the dark subhalo population, but also on the morphological and physical properties of the gravitationally lensed background source. This is particularly important given current and future observing facilities that provide mas-scale resolution imaging

of the gravitationally lensed high redshift Universe. For the specific case of SDSS J0755+3445, we have found that the source focusing is significantly improved when the complexity of the macro-model is progressively increased. We find that the estimated morphological and physical properties of the reconstructed source can change by up to 22 per cent in this case due to inaccuracies in the assumed form of the macro-model. Indeed, here we have demonstrated that the inferred source morphology can provide additional useful information that may help in identifying issues with the assumed form of the macro-model parameterization, which may be better than the image residuals. However, at present it is unclear if this result can be easily generalized and more systematically quantified, as more complicated intrinsic source morphologies may lend themselves less readily to a by-eye identification of defocusing.

Chapter 4

Low-mass halo perturbations in strong gravitational lenses at redshift z~0.5 are consistent with CDM

Published on MNRAS as:
Ritondale, E., Vegetti S., Despali G., Auger, M. W., Koopmans L. V. E., McKean J. P. (2019), 'Low-mass halo perturbations in strong gravitational lenses at redshift z~0.5 are consistent with CDM', *MNRAS* 485, 2179 - 2193.

4.1 Introduction

In this chapter, we apply the *gravitational imaging* technique developed by Koopmans (2005) and Vegetti & Koopmans (2009) to a sample of 17 gravitational lenses from the BOSS Emission-Line Lens Survey (BELLS) for GALaxy-Lyα EmitteR sYstems (BELLS GALLERY) (Shu et al. 2016a). We combine the detections and non-detections of low-mass haloes to derive new statistical constraints on the dark matter mass function and compare our results with predictions from CDM and different sterile neutrino dark matter models. This chapter is structured as follows: in Section 4.2 we describe the data and in Section 4.3 we present an overview of the adopted analysis scheme and summarise the gravitational imaging method. In Section 4.4, we present the statistical approach used to infer the parameter of the subhalo and halo mass functions and the free-streaming properties of dark matter. We give our results in Sections 4.5 and 4.6, and present our conclusions in Section 4.7.

4.2 Data

Our sample is described in detail in Chapter 2 and consists of 17 Lyman-α emitting galaxies at redshifts from 2.1 to 2.8 that are gravitationally lensed by massive early-type galaxies at a mean redshift of 0.5. For more details about the sample we refer to Table 4.1, Chapter 3 and

Table 4.1: Summary of the details of the gravitational lens systems analysed here. For each system we list here the SDSS name, the lens and source redshifts, the rest-frame wavelength of the UV emission observed through the F606W filter, the observation exposure time and the Einstein radius from Ritondale et al. (2019a). For lens systems with multiple lenses we list the Einstein radius for each deflector.

Name (SDSS)	z_{lens}	z_{src}	λ_{rest} [Å]	Exp. Time [s]	R_{ein} [arcsec]
J0029 + 2544	0.587	2.450	1706	2504	1.295
J0113 + 0250	0.623	2.609	1631	2484	1.226
					0.065
					0.172
J0201 + 3228	0.396	2.821	1540	2520	1.650
J0237 − 0641	0.486	2.249	1812	2488	0.687
J0742 + 3341	0.494	2.363	1751	2520	1.197
J0755 + 3445	0.722	2.634	1620	2520	1.926
J0856 + 2010	0.507	2.233	1821	2496	0.960
J0918 + 4518	0.581	2.344	1730	2676	0.444
					0.409
J0918 + 5104	0.581	2.404	1730	2676	1.600
J1110 + 2808	0.607	2.399	1732	2504	0.992
J1110 + 3649	0.733	2.502	1682	2540	1.152
J1141 + 2216	0.586	2.762	1565	2496	1.281
J1201 + 4743	0.563	2.126	1883	2624	1.139
J1226 + 5457	0.498	2.732	1578	2676	1.351
J1529 + 4015	0.531	2.792	1553	2580	2.233
J2228 + 1205	0.530	2.832	1536	2492	1.291
J2342 − 0120	0.527	2.265	1803	2484	1.033

Shu et al. (2016a). Images of the lensed emission are shown in Fig. 4.1. Gravitational lens models, under the assumption of a smooth elliptical power-law lensing potential, and Sérsic parameters for the lens surface brightness distribution for all 17 systems are respectively reported in Table 2.4 and Table 2.5. More details can be found in Section 4.3.2 and Chapter 2. Briefly, the analysis in Chapter 2 revealed that these Lyman-α emitting sources are qualitatively very structured with extremely inhomogeneous surface brightness distributions. They often consist of multiple components that sometimes appear to be connected or merging, while in other cases, they appear as clearly separated components in the sky (see Fig. 4.2). Their intrinsic sizes vary quite widely, from 0.2 kpc to 1.8 kpc in radius and they have a relatively low median integrated star formation rate of 1.4 $M_\odot$ yr^{-1}, on average.

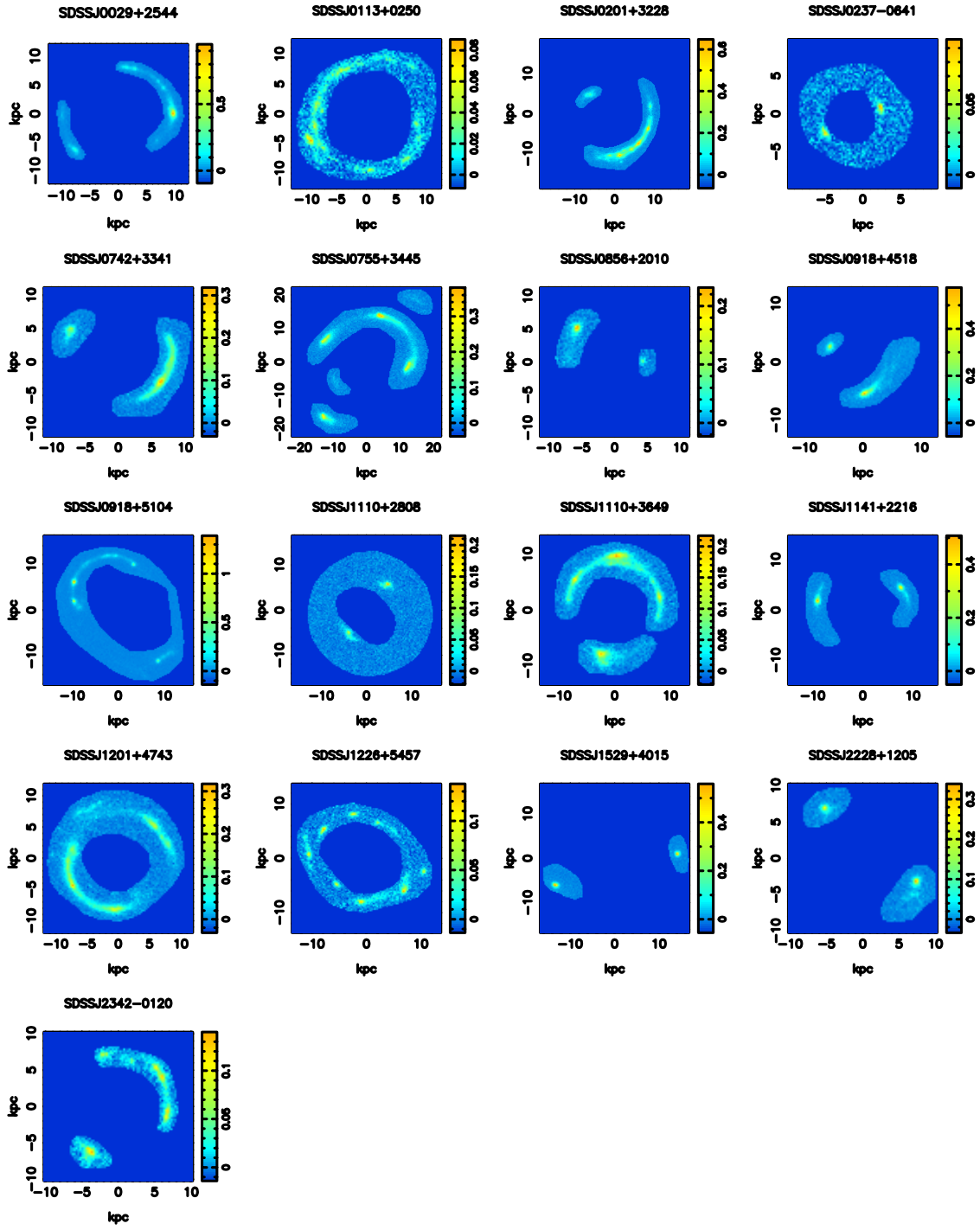

Figure 4.1: The surface brightness distributions of the lensed images within a selected region on the sky plane used to reconstruct the background sources. The colour scale is in units of electron s^{-1} and the projected areas shown are at the redshift of the lens.

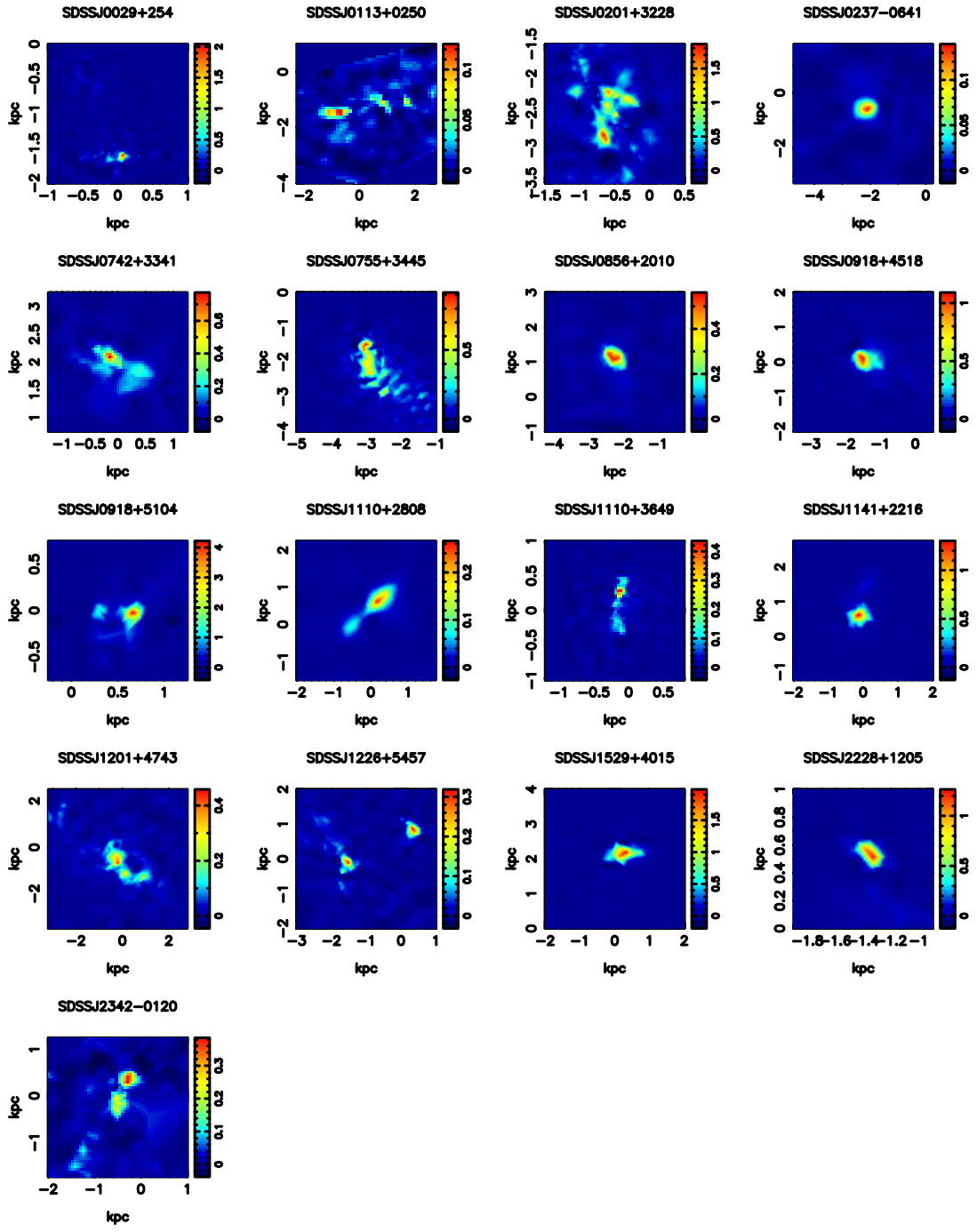

Figure 4.2: The surface brightness of each background LAE, based on the pixelated source reconstructions from the gravitational lens modelling. The colour scale is in units of electron s^{-1} and the projected areas shown are at the redshift of the source.

4.3 Lens modelling

Each of the gravitational lens systems in the sample has been analysed with an updated version of the grid-based fully Bayesian modelling method developed by Vegetti & Koopmans (2009) and described in Chapter 2. This technique simultaneously optimises for the surface brightness of the background source and the brightness and mass distribution of the foreground lens galaxy. Our lens modelling procedure is carried out in two subsequent steps. First, we find the best mass and light model for the main lensing galaxies under the assumption of a relatively smooth mass distribution, meaning that we do not allow for the presence of any subhalo or line-of-sight halo. We have reported the results of this analysis in Capter 2. Then, we look for the gravitational signature of dark-matter subhaloes and line-of-sight haloes (collectively referred to as haloes for the rest of the chapter) on the surface brightness distribution of the lensed images, and use their number and inferred masses to derive constraints on the dark matter properties. In this Section, we review the methodology, giving a summary of what described in Chapter 2, in order to introduce the grid-based potential corrections in the following section (Vegetti & Koopmans 2009).

4.3.1 Lens mass and light distribution model

The mass distribution of each lens galaxy is parametrized as a cored elliptical power-law with normalised surface mass density κ expressed as

$$\kappa(x,y) = \frac{\kappa_0 \left(2 - \frac{\gamma}{2}\right) q^{\gamma-3/2}}{2\left(q^2\left(x^2 + r_c^2\right) + y^2\right)^{(\gamma-1)/2}}\,, \tag{4.1}$$

while its light distribution is parametrized by one or a sum of elliptical Sérsic profiles, with each component given by

$$S_h(x,y) = I_h \exp\left[-a_h\left(\left(\frac{\sqrt{q_{l,h}^2 x^2 + y^2}}{R_{e,h}}\right)^{1/n_h} - 1.0\right)\right] = I_h\, \Sigma_h(x,y)\ . \tag{4.2}$$

In equation (4.1), κ_0 is the surface mass density normalization, γ is the radial mass-density slope, q is the axis ratio and r_c the core-radius. The normalization of the density $\kappa(x,y)$ is chosen such that the mass within the Einstein radius is independent of the axis ratio q. The contribution of an external shear component is parametrized by its strength Γ and positional angle Γ_θ, while in equation (4.2) I_h is the normalization, $a_h = 1.9992 \times n_h - 0.3271$ (Capaccioli 1989), $q_{l,h}$ the axis ratio, $R_{e,h}$ the effective radius and n_h the Sérsic index.

Given one lens system of n lenses and N Sérsic components, we refer to the free parameters of the mass and the light distributions respectively as $\boldsymbol{\eta}_m = \{\boldsymbol{\eta}_{m,j}\}_{j=1}^{n}$ and $\boldsymbol{\eta}_l = \{\boldsymbol{\eta}_{l,\{j,h\}}\}_{j,h=1}^{n,N}$, with $\boldsymbol{\eta}_{m,j} = \{k_{0,j}, \theta_j, q_j, x_j, y_j, r_{c,j}, \gamma_j, \Gamma_j, \Gamma_{\theta,j}\}$ and $\boldsymbol{\eta}_{l,\{j,h\}} = \{R_{e,\{j,h\}}, n_{\{j,h\}}, x_{l,\{j,h\}}, y_{l,\{j,h\}}, q_{l,\{j,h\}}, \theta_{l,\{j,h\}}\}$. They are all simultaneously optimized, except for r_c, which we keep fixed at 0.1 mas and each lens j is independently modelled. As the background source is also unknown, the other free parameters

of the model are the source surface brightness distribution at each pixel on the source plane and regularisation level λ_s that sets the *smoothness* of the source model (see Vegetti & Koopmans 2009, for more details).

4.3.2 Grid-based source model

The surface brightness distribution of each pixel in the lens plane $\mathbf{d}$ is given by the sum of the lensed emission $\boldsymbol{d_s}$ of the background source $\boldsymbol{s}$ and the foreground lens brightness distribution $\mathbf{d}_l$. The positions of the pixels on the lens- and source-planes are related to each other by the lensing potential $\psi_s(\mathbf{x}, \boldsymbol{\eta}_m)$ via the lens equation, where we consider one lens and one source plane respectively. The effect of the line-of-sight haloes is projected onto the main lens plane, using the mass-redshift relation by Despali et al. (2018) (see also Section 4.3.4), which takes into account the non-linear effects due to the multi-plane lens configuration. The conservation of surface brightness by gravitational lensing then leads to the following set of linear equations

$$\mathbf{B}\left[\mathbf{L}(\psi, \boldsymbol{\eta}_m) \mid (\boldsymbol{\Sigma}_0 \ldots \boldsymbol{\Sigma}_N) \mid \mathbf{1}\right] \begin{pmatrix} \boldsymbol{s} \\ I_0 \\ . \\ . \\ . \\ I_N \\ b \end{pmatrix} + \boldsymbol{n} = \boldsymbol{d_s} + \boldsymbol{d_l} = \mathbf{d}\,, \tag{4.3}$$

where $\mathbf{B}$ is the blurring operator, which represents the effect of the point spread function, $\mathbf{L}$ is the lensing operator, $\boldsymbol{\Sigma_h}$ is the surface brightness at each pixel of the hth Sérsic component, $\boldsymbol{n}$ is the noise vector and $\mathbf{1}$ is a vector with as many entries as the number of pixels in the lens plane, all equal to one. $I_0, ..., I_N$ are the unknown Sérsic component normalizations and b is the pedestal which is a constant accounting for the sky background. These are computed at each iteration by solving equation (4.6) for a given set of the parameters $\boldsymbol{\eta}_m$ and $\boldsymbol{\eta}_l$. Under the assumption of Gaussian noise, the maximum a posteriori (MAP) parameters $\boldsymbol{\eta}_m$, λ_s and $\boldsymbol{\eta}_l$ can be inferred by maximizing the penalty function

$$P(\mathbf{r}, \boldsymbol{\eta}_m, \boldsymbol{\eta}_l, \lambda_s \mid \mathbf{d}, \mathbf{H}_s) \propto ||\mathbf{Mr} - \mathbf{d}||_2^2 + \lambda_s^2 ||\mathbf{H}_s \mathbf{r}||_2^2\,, \tag{4.4}$$

where we have introduced the vector $\mathbf{r}^\intercal = (\boldsymbol{s}, I_0 ... I_n, b)$ and rephrased equation (4.3) as

$$\mathbf{Mr} + \mathbf{n} = \mathbf{d}\,, \tag{4.5}$$

with $\mathbf{M}$ the product of the blurring operator with the lensing operator and foreground surface brightness matrix. The first term of the penalty function represents the χ^2 difference between the data and the model, while the second term includes a priori information on the smoothness of the source surface brightness distribution encoded by the level and form of the regularization λ_s and $\mathbf{H}_s$. The latter is set to zero in the entries multiplying the Sérsic component normalizations. For

each choice of the non-linear parameters $\boldsymbol{\eta}_m$, $\boldsymbol{\eta}_l$ and λ_s, the corresponding value for $\mathbf{r}$ is obtained by solving the linear system

$$\left(\mathbf{M}^T \mathbf{C}_d^{-1} \mathbf{M} + \lambda_s^2 \, \mathbf{H}_s^T \mathbf{H}_s\right) \mathbf{r} = \mathbf{M}^T \mathbf{C}_d^{-1} \mathbf{d} \,, \tag{4.6}$$

where $\mathbf{C}_d$ is the data covariance matrix and is assumed to be diagonal, that is, we ignore any correlation among data pixels. In fact the only non-zero correlation term is due to drizzling, which is as low as 0.2 between adjacent pixels and effectively zero up to the second neighbouring pixel (Bayer et al. 2018).

4.3.3 Grid-based Potential Corrections

At this stage of the lens modelling, we gravitationally image low-mass subhaloes by describing them as linear localized pixellated corrections $\delta\psi(\mathbf{x})$ to the main lensing potential. In practice, at each position $\mathbf{x}$ on the main lens plane, we redefine the lensing potential as $\psi(\mathbf{x}, \boldsymbol{\eta}_m) = \psi_s(\mathbf{x}, \boldsymbol{\eta}_m) + \delta\psi(\mathbf{x})$. Where $\psi_s(\mathbf{x}, \boldsymbol{\eta}_m)$ is the parametric smooth potential introduced in the previous section. Following the formalism developed by Koopmans (2005) and Vegetti & Koopmans (2009), we then introduce a new linear system relating the image and the source planes, which at each iteration n reads as

$$\mathbf{M}\left(\boldsymbol{\eta}_m, \boldsymbol{\eta}_l, \psi_{n-1}, \boldsymbol{s}_{n-1}\right) \mathbf{r}_n + \mathbf{n} = \mathbf{d} \,, \tag{4.7}$$

with

$$\mathbf{M} = \mathbf{B}\left[\mathbf{L}\left(\boldsymbol{\eta}_m, \psi_{n-1}\right) \mid -\mathbf{D}_s(s_{n-1})\mathbf{D}_\psi \mid \boldsymbol{\Sigma_i} \mid \mathbf{1}\right] \tag{4.8}$$

and

$$\mathbf{r}_n^{\intercal} = \left(\boldsymbol{s}, I_0 ... I_n, b, \delta\boldsymbol{\psi}_n\right) . \tag{4.9}$$

Here, $\mathbf{D}_s(s_{n-1})$ is a sparse matrix whose entries depend on the surface brightness gradient of the best source at the $n-1$ iteration and $\mathbf{D}_\psi$ is a matrix that determines the gradient of $\delta\boldsymbol{\psi}_n$ (see Koopmans 2005, for more details). Introducing $\mathbf{H}_{\delta\psi}$ and $\lambda_{\delta\psi}$ as the form and level of regularization for the potential corrections $\delta\boldsymbol{\psi}_n$, we can now write a new penalty function as

$$P\left(\mathbf{r}_n \mid \mathbf{d}, \boldsymbol{\eta}_m, \boldsymbol{\eta}_l, \lambda_s, \lambda_{\delta\psi}, \boldsymbol{s}_{n-1}, \mathbf{H}_s, \mathbf{H}_{\delta\psi}\right) \propto ||\mathbf{M}\mathbf{r}_n - \mathbf{d}||_2^2 + \lambda_s^2 ||\mathbf{H}_s \boldsymbol{s}_n||_2^2 + \lambda_{\delta\psi}^2 ||\mathbf{H}_{\delta\psi}\delta\boldsymbol{\psi}_n||_2^2 \,. \tag{4.10}$$

We can further define $\mathbf{R}$ as the diagonal block matrix that contains the regularization level parameters λ_s and $\lambda_{\delta\psi}$, and combines the source and potential regularization operators $\mathbf{H}_s$ and $\mathbf{H}_{\delta\psi}$. Maximising the penalty function with respect to $\mathbf{r}$ leads to the following set of equations for $\mathbf{r}_n$

$$\left(\mathbf{M}^T \mathbf{C}_d^{-1} \mathbf{M} + \mathbf{R}\right) \mathbf{r}_n = \mathbf{M}^T \mathbf{C}_d^{-1} \mathbf{d}. \tag{4.11}$$

The solution of this linear system can be found using an iterative technique; in particular, we solve equation (4.11) and then add the correction $\delta\boldsymbol{\psi}_n$ to the best potential of the previous iteration $\boldsymbol{\psi}_{n-1}$. While iterating this procedure, both the source and the potential should converge to the maximum of the penalty function, given by equation (4.10), following a Gauss-Newton scheme. At every step of this procedure, the matrix $\mathbf{M}$ has to be recalculated for the new updated potential $\boldsymbol{\psi}_n$ and source $\boldsymbol{s}_n$. While the potential grid points are kept spatially fixed in the image

plane, a Delaunay tessellation grid for the source is rebuilt at every iteration to ensure that the number of degrees of freedom is kept constant during the entire optimization process. Pixellated convergence corrections can be derived from the corresponding potential corrections by applying the Laplace operator. At this stage of the analysis, the non-linear parameters $\boldsymbol{\eta}_m$, $\boldsymbol{\eta}_l$ and λ_s are kept fixed at the MAP parameters inferred in Section 4.3.2. This has two effects: (i) $\delta\psi$ has both positive and negative peaks in oder to conserve the total mass; (ii) $\delta\psi$ includes corrections due to subhaloes as well as any departures from the macro-model assumptions. The latter is an important aspect of this technique that allows us to distinguish between genuine and spurious subhalo detections, as shown in Chapter 3. However, a systematic quantification of the interplay and degeneracy between complex mass distribution and the properties of substructure and of the background source has not been studied yet and we plan to address this issue in the future.

4.3.4 Small mass haloes as analytical mass components

The main advantage of describing subhaloes as pixellated potential corrections is that it does not require any prior assumption on their number and mass density profile. However, the non-linear parameters describing the main lensing potential are fixed at the best smooth values and the number of degrees of freedom defined by the potential correction grid can be relatively large. Therefore, the *gravitational imaging* alone does not allow the degeneracy between the properties of the main lens and those of the subhalo to be straightforwardly quantified nor to be used to statistically compare models (Vegetti & Koopmans 2009).

To this end, we follow our pixellated analysis with an analytical description of the mass density profile of the low-mass haloes. At this stage of the analysis, we assume that all of the haloes are at the same redshift of the lens, that is subhaloes. Using the mass-redshift relation from Despali et al. (2018), we then derive the mass that these haloes should have had in order to generate the most similar lensing effect if they were located at a different redshift, that is, along the line of sight. In this procedure, we take into account the non-linear effects due to the multi-plane lens configuration. At this step, the haloes are parametrized by a spherically symmetric NFW profile (Navarro et al. 1996) with the concentration-mass relation of Duffy et al. (2008). While this mass density profile is a good description for the line-of-sight haloes, it is only an approximation for the subhaloes that have been accreted by the halo of the lens galaxy, and have therefore experienced events of tidal disruption. At a fixed virial mass, this results in a higher concentration that is mildly dependent on the subhalo distance from the host centre. However, Despali et al. (2018) have shown that assuming a constant mass-concentration relation from Duffy et al. (2008) plays only a secondary effect and leads to an error on the inferred mass of 5 per cent for subhaloes with masses of $10^{5-6} M_\odot$ and 20 per cent for masses of $10^9 M_\odot$. These errors are significantly smaller than the de-projection errors on the total mass of pseudo-Jaffe profiles (Minor et al. 2017; Despali et al. 2018) and it leads to an error on the expected number of subhaloes of the order of 10 per cent.

At this stage of the analysis, the free parameters of the model are: the non-linear parameters describing the main lens mass and light distribution, the source surface brightness distribution in each pixel and its regularization, the NFW virial mass and the projected position of each halo.

4.3.5 Bayesian evidence and model comparison

In order to determine the statistical significance of a subhalo detection, we compare the marginalised Bayesian evidence of the smooth and perturbed analytical models to determine which of the two is preferred by the data. For each system, the Bayesian evidence is computed using MultiNest (Feroz et al. 2013) as the following integral

$$\mathcal{E} = P(\mathbf{d}|\mathbf{M}, \mathbf{H}_s) = \int P(\mathbf{d}|\lambda_s, \boldsymbol{\eta}_m, \boldsymbol{\eta}_l, m, \mathbf{x}, \mathbf{M}, \mathbf{H}_s)\, P(\lambda_s, \boldsymbol{\eta}_m, \boldsymbol{\eta}_l, m, \mathbf{x})\, d\lambda_s d\boldsymbol{\eta}_m d\boldsymbol{\eta}_l dm d\mathbf{x}\,, \quad (4.12)$$

where, $P(\lambda_s, \boldsymbol{\eta}_m, \boldsymbol{\eta}_l, m, \mathbf{x})$ is the normalized prior probability density distribution on the model parameters, and is chosen as follows: for the non-linear parameters $\boldsymbol{\eta}_m$, $\boldsymbol{\eta}_l$ and λ_s, we choose uniform priors within an interval centred on the MAP value derived in Section 4.3 and as large as 10, 20 or 40 per cent of this value, with priors always consistent between the smooth and the perturbed model for each lens [1]. For the source regularization level λ_s, the prior is uniform in logarithmic space. Both the prior on the model parameters and the likelihood are properly normalized to have integrals of unity. At this stage, subhaloes are described analytically (as discussed in Section 4.3.4). Their masses m have a uniform prior in logarithmic space, while their positions $\mathbf{x}$ are equally probable at any location on the plane of the lensed images.

Detection criteria

As demonstrated by McKean et al. (2007), Gilman et al. (2017) and Hsueh et al. (2016, 2017, 2018), assuming that all departures from a smooth power-law elliptical potential are due to the presence of dark subhaloes and line-of-sight haloes can lead to the false detection of haloes with a high statistical significance. Indeed, a complex lensing potential, as for example in the form of edge-on discs, can affect the lensed observables in a way which is degenerate with a large number of low-mass haloes. In this respect, the pixellated gravitational imaging technique, described in Section 4.3.3, represents a clear advantage as it allows for the identification and quantification of all departures from a simple power-law macro model, independently of their origin. To obtain a reliable set of detections and non-detections, it is therefore important to combine the results of the two analyses that have been carried out in a completely independent way. Following Vegetti et al. (2014), we define a detection as robust if:

1. a positive and localized convergence correction is identified, it improves the fitting quality of the data and does not depend on the source regularization forms and levels;

2. the analysis using parametric models for the haloes in Sections 4.3.4 and 4.3.5 leads to the detection of a subhalo with the same mass and at the same location as the peak of the convergence corrections identified at the previous step;

[1] Building the prior volume based on the data is not consistent with a Bayesian approach, but we checked that this does not impact the resulting parameter values.

3. the model that includes the presence of a subhalo is preferred over the smooth model by a difference in the Bayesian evidence of $\Delta \log \mathcal{E} = \log \mathcal{E}_{\rm pert} - \log \mathcal{E}_{\rm sm} \geq 50$, corresponding roughly to a 10-σ detection at its inferred position.

Detection threshold

As described in the previous section, we choose to set our detection threshold at a Bayes factor of $\Delta \log \mathcal{E} \geq 50$. Under the assumption of statistical Gaussian errors, this corresponds to a 10σ-threshold. Using the reconstructed sources from the 10 systems with the highest number of data pixels in the lens plane, we have also tested the reliability of lower-significance cuts. In particular, from each of the 10 reconstructed sources we have created four mock lensed data sets with the same level of signal-to-noise ratio and resolution as the original data: one smooth model and three including a subhalo detectable at the 4 ($\Delta \log \mathcal{E} \geq 8$), 5 ($\Delta \log \mathcal{E} \geq 12.5$) and 6-$\sigma$ ($\Delta \log \mathcal{E} \geq 18$) level. We have then analysed these data in the same way as the real dataset and overall found a high percentage of false positive (almost 60 per cent) and false negatives (almost 40 per cent). In 30 per cent of the cases we have either recovered the correct lack of subhaloes or correctly detected the presence of an existing one. The percentage of false positives and false negatives drops from 100 per cent (40 and 60 per cent respectively) at the 4-σ level, to 90 per cent (20 and 70 per cent respectively) at the 5-σ one, and finally to 60 per cent (30 per cent for both) at the 6-σ case. We therefore conclude that these lower-significance cuts are statistically unreliable. We believe this to be related to the fact that the conversion between the Bayes factor and a simple confidence level is only valid under the approximation of Gaussian statistical errors and does not include the effects of systematics (especially in relation to the source structure). In the rest of the chapter, we therefore quote as robust our results based on the more conservative 10-σ cut, for which we recover correct results in 80 per cent of the cases (10 per cent of false positives and 10 per cent of false negatives).

4.4 Inference on dark matter

In this section, we describe how the detection and non-detection of subhaloes and line-of-sight haloes are statistically combined to constrain the free-streaming properties of dark matter.

4.4.1 Mass and position definition

In the following, we denote with $m^{\rm o}$ the observed NFW virial mass, that is the mass that one would infer from the lens modelling of the data under the substructure assumption. This mass is allowed to vary between the lowest detectable mass $M_{\rm low}^{\rm NFW}(\mathbf{x}^{\rm o})$ at each considered projected position $\mathbf{x}^{\rm o}$ (see Section 4.4.4 for a definition) and the maximum NFW virial mass $M_{\rm max}^{\rm NFW} = 10^{11}$ $\mathrm{M}_\odot$. The true NFW virial mass of a subhalo at the redshift of the lens or a line-of-sight halo at an arbitrary redshift z is referred to as m, and it is allowed to assume any value between $M_{\rm min}^{\rm NFW} = 1.0 \times 10^5$ $\mathrm{M}_\odot$ and $M_{\rm max}^{\rm NFW}$. The observed and true mass are statistically related to each other via equation (4.22). The observed and true projected position of haloes are respectively

indicated with $\mathbf{x}^{\rm o}$ and $\mathbf{x}$. The former is defined as the projected position on the lens plane where the lensed images are affected by the presence of the halo. For subhaloes, $\mathbf{x}^{\rm o}$ and $\mathbf{x}$ are related to each other by a relatively small measurement error (Despali et al. 2018). For line-of-sight haloes, the recursive nature of the lens equation needs to be taken into account.

4.4.2 Dark matter mass function

Following Schneider et al. (2012) and Lovell et al. (2014), we parametrise the subhalo and halo mass function as

$$n\left(m|M_{\rm hm},\beta\right) = n^{\rm CDM}\left(m\right)\left(1+\frac{M_{\rm hm}}{m}\right)^{\beta}, \tag{4.13}$$

where $n^{\rm CDM}\left(m\right)$ is the number density of objects with mass m in the CDM framework and the second factor expresses the suppression in the number of haloes due to the free streaming of the dark matter particles. In particular, $M_{\rm hm}$ is the mass scale at which the WDM mass power-spectrum is suppressed by one half with respect to the CDM one and β is the slope of the WDM mass function below the turn-over mass. For the subhalo CDM mass function we assume a power-law mass function given by

$$n^{\rm CDM}_{\rm sub}\left(m\right) \propto m^{-\alpha}. \tag{4.14}$$

Instead, for the CDM mass function of line-of-sight haloes, we adopt the expression by Sheth & Tormen (1999), with the best-fit parameters optimized for the Planck cosmology from Despali et al. (2016) [2].

4.4.3 Likelihood

In the following, we refer to $m^{\rm ob}_i$ and $\mathbf{x}^{\rm ob}_i$ as the bins of observed mass $m^{\rm o}$ and projected position $\mathbf{x}^{\rm o}$ that correspond to a detected halo. As in Vegetti et al. (2018), we have chosen the widths of these mass and position bins to be small enough so that the maximum number of detections per bin is one. We have also assumed a Poisson distribution for the number of haloes. Under this assumption, we can express the likelihood of detecting n objects (subhaloes plus line-of-sight haloes) with observed NFW masses $\left\{m^{\rm ob}_1,....,m^{\rm ob}_n\right\}$ at the projected positions $\left\{\mathbf{x}^{\rm ob}_1,....,\mathbf{x}^{\rm ob}_n\right\}$, and no detection in all other mass and position ranges as follows (see Vegetti et al. 2018, for a complete derivation)

$$\begin{aligned}\log P\left(\left\{m^{\rm ob}_1,....,m^{\rm ob}_n\right\},\left\{\mathbf{x}^{\rm ob}_1,....,\mathbf{x}^{\rm ob}_n\right\}|\theta\right) = \\ -\int\left[\mu_s(m^{\rm o},\mathbf{x}^{\rm o})+\mu_l(m^{\rm o},\mathbf{x}^{\rm o})\right]dm^{\rm o}d\mathbf{x}^{\rm o}+ \\ \sum_i^n \log\left[\mu_s\left(m^{\rm ob}_i,\mathbf{x}^{\rm ob}_i\right)dm^{\rm o}d\mathbf{x}^{\rm o}+\mu_l\left(m^{\rm ob}_i,\mathbf{x}^{\rm ob}_i\right)dm^{\rm o}d\mathbf{x}^{\rm o}\right],\end{aligned} \tag{4.15}$$

[2]These cosmology parameters are slightly different (<10 per cent) from the ones stated in the Introduction 1. However, this difference does not impact the formation of structures as small as the ones we are concerned with. Therefore, this difference is not important for our purposes (Despali et al. 2016).

where $\boldsymbol{\theta}$ is a vector containing the set of parameters describing the subhalo and halo mass functions (see Section 4.4.6 for an explicit definition). The above integrals are computed between the lowest detectable mass $M_{\rm low}^{\rm NFW}(\mathbf{x}^{\rm o})$ and $M_{\rm max}^{\rm NFW}$, while for the positions we consider all pixels on the lens plane used to reconstruct the background source (see Fig. 4.1). Here, $\mu_s\,(m^{\rm o}, \mathbf{x}^{\rm o})\,dm^{\rm o}d\mathbf{x}^{\rm o}$ and $\mu_l\,(m^{\rm o}, \mathbf{x}^{\rm o})\,dm^{\rm o}d\mathbf{x}^{\rm o}$ are the mean expected number of subhaloes and line-of-sight haloes, respectively, in the mass range $m^{\rm o}, m^{\rm o} + dm^{\rm o}$, and projected position range $\mathbf{x}^{\rm o}, \mathbf{x}^{\rm o} + d\mathbf{x}^{\rm o}$. These are derived in Section 4.4.5.

4.4.4 Sensitivity function

In order to derive constraints on the subhalo and halo mass function, it is necessary to calculate the sensitivity function for each lens system in the sample. The latter is defined as the lowest detectable NFW mass at the redshift of the main lens $M_{\rm low}^{\rm NFW}(\mathbf{x}^{\rm o})$ for each position in the lens plane of each system in the sample. It is computed as the smallest observed mass for which a clumpy model is preferred over the smooth one by a factor of the marginalized Bayesian evidence (see Section 4.3.5) corresponding to a 10-σ detection cut.

As demonstrated by Koopmans (2005) and Rau et al. (2014), the sensitivity function strongly depends on the complexity of the surface brightness distribution of the background source. In fact, the strength of a surface brightness anomaly (δI) due to a potential perturbation $\delta\psi$ is $\delta I = -\nabla \boldsymbol{s} \cdot \nabla\delta\psi$, that is, the inner product of the gradient of the source brightness distribution (where $\nabla \boldsymbol{s}$ is evaluated in the source plane) dotted with the gradient of the potential perturbation due to subhaloes (where $\delta\psi$ is evaluated in the image plane). Hence, mass (sub)structure can be detected more easily for sources that are highly structured (i.e. large values of $|\nabla \boldsymbol{s}|$) or, conversely, more structured sources allow for a lower mass detection threshold for a fixed signal-to-noise ratio.

The sample analyzed in this chapter consists of 17 lensed Lyman-α emitters, that are known to be very structured galaxies and characterised by a high dynamical range in their brightness distribution (Ritondale et al. 2019a). Therefore, these data could in principle be characterized by a relatively high sensitivity (i.e. low mass detection threshold). We present the actual distribution of pixels as a function of lowest-detectable mass in comparison with the SLACS lenses in Section 4.6.1.

4.4.5 Expectation values

Given the sensitivity functions, it is now possible to compute the expected total number of subhaloes and line-of-sight haloes as

$$\mu(m^{\rm o}, \mathbf{x}^{\rm o}) = \mu_0 \times \int P(I = 1|m^{\rm o}, \mathbf{x}^{\rm o}) P(m^{\rm o}|m, z) P(m, z|\boldsymbol{\theta}) P(\mathbf{x}^{\rm o}|\mathbf{x}, z) P(\mathbf{x}) P(z)\; dmdzd\mathbf{x}\,. \qquad (4.16)$$

The mass integrals are evaluated between $M_{\rm min}^{\rm NFW}$ and $M_{\rm max}^{\rm NFW}$. I is a vector that is equal to one for detectable objects and zero otherwise, so that $P(I = 1|m^{\rm o}, \mathbf{x}^{\rm o})$ encodes the sensitivity function

and is given by

$$P(I = 1|m^{\rm o}, \mathbf{x}^{\rm o}) = \begin{cases} 1 & \text{if } m^{\rm o} \geq M_{\rm low}(\mathbf{x}^{\rm o}) \\ 0 & \text{otherwise} \end{cases} . \tag{4.17}$$

$P(m, z|\theta)dmdz$ is the probability of finding one halo in the mass range $m, m + dm$ and in the redshift range $z, z + dz$. It is related to the mass functions by

$$P(m, z|\boldsymbol{\theta})dmdz = n(m, z|\boldsymbol{\theta})\frac{dV}{dz}dmdz\left[\int n(m', z'|\boldsymbol{\theta})\frac{dV}{dz'}dm'dz'\right]^{-1} , \tag{4.18}$$

and, for subhaloes, it reduces to the following expression

$$P(m|\boldsymbol{\theta})\mathbf{dm} = n(m|\boldsymbol{\theta})\mathbf{dm}\left[\int n(m'|\boldsymbol{\theta})dm'\right]^{-1} \tag{4.19}$$

with $n(m|\boldsymbol{\theta})$ given by equation (4.13).

Introducing the projected mass of the main lens $M_{\rm lens}$ and a projected total mass fraction in substructure $f_{\rm sub}$ between $M^{\rm NFW}_{\rm min}$ and $M^{\rm NFW}_{\rm max}$, we express μ_0 as follows

$$\mu_0 = f_{\rm sub}M_{\rm lens}\left[\int m' P(m'|\boldsymbol{\theta})dm'\right]^{-1} . \tag{4.20}$$

For line-of-sight haloes μ_0 is expressed instead as

$$\mu_0 = \int n(m', z'|\boldsymbol{\theta})\frac{dV(\mathbf{x}')}{dz'}dm'dz'd\mathbf{x}' . \tag{4.21}$$

As the measurement error on the halo positions is relatively small (Despali et al. 2018), we assume $P(\mathbf{x}^{\rm o}|\mathbf{x}, z) = \delta(\mathbf{x} - g(\mathbf{x}^{\rm o}, z))$, that is a delta function. For subhaloes, $g(\mathbf{x}^{\rm o}, z) \equiv \mathbf{x}^{\rm o}$, whilst for line-of-sight haloes $g(\mathbf{x}^{\rm o}, z)$ takes into account the effect of the recursive lens equation. Following the results by Xu et al. (2015) and Despali et al. (2018), we assume a uniform probability for $P(\mathbf{x})$. The redshift of line-of-sight haloes have a uniform prior between the observer and the source, excluding the region within the main lens virial radius. The latter estimated to be ~ 390 kpc and 0.0001 in redshift, assuming that the lens galaxies are typical early-types at $z \sim 0.5$ and have a mean halo mass of $\mathrm{M} = 10^{13}\ \mathrm{M}_{\odot}$. For subhaloes $P(z) = \delta\,(z - z_{\rm lens})$.

As the detection threshold $M^{\rm NFW}_{\rm low}(\mathbf{x}^{\rm o})$ and the measured mass $m^{\rm o}$ were derived under the substructure assumption, we account for the different lensing effect of line-of-sight haloes via the term

$$P(m^{\rm o}|m, z) = \frac{1}{\sqrt{2\pi}m^{\rm o}\sigma(z)}\exp\left[-\frac{\left(\log m^{\rm o} - f(m, z)\right)^2}{2\sigma^2(z)}\right]. \tag{4.22}$$

Given a line-of-sight halo of NFW virial mass m located at redshift z, $f(m, z)$ returns the NFW virial mass at the same redshift of the main lens with the most similar gravitational lensing effect, for a Duffy et al. (2008) concentration-mass relation. Here, we do not use the exact relation reported by Despali et al. (2018), but we derive a characteristic relation for each lens in our sample using mock lensed images of each of the lenses in the sample. The intrinsic scatter $\sigma(z)$

is also not the same as the one given by Despali et al. (2018), but it is a sum in quadrature of the error on the measured mass $m^{\rm o}$ and the uncertainty related to changes in the mass redshift-relation as a function of position on the image plane in a way that depends on the main lens deflection angle and the external shear. In the case of subhaloes, $f(m, z)$ reduces to m and $\sigma(z)$ reduces to the mass measurement error.

4.4.6 Prior and posterior distributions

The target parameters of the model, expressed by the vector $\boldsymbol{\theta}$, are the subhalo and halo mass function slopes, respectively α and β, the projected total dark matter fraction in subhaloes $f_{\rm sub}$, and the half-mode mass $M_{\rm hm}$. These are drawn from the following prior probabililty density distributions: (i) for α and β we assume a Gaussian prior centred at 1.9 and -1.3 and with σ of 0.2 and 0.1, respectively; (ii) we draw the values of $f_{\rm sub}$ from a uniform prior density distribution in $1/\sqrt{f_{\rm sub}}$ between 0 and 0.2; (iii) for the half-mode mass we assume a logarithmic prior distribution between 10^6 and 2×10^{12} $\mathrm{M}_\odot$. Both priors are chosen in order to allow for an even exploration of the parameter space. This range of $M_{\rm hm}$ covers the most commonly considered WDM models, including the 3.5 keV model. The lower limit $\mathrm{M_{hm}} = 10^6$ $\mathrm{M}_\odot$ is strictly speaking warmer than CDM, but in practice indistinguishable from it within the mass range probed by the sensitivity of the data (see Section 4.6.3).

The posterior probability density distribution is obtained assuming the different lens systems in the sample to be statistically independent from each other.

4.5 Lens modelling results

A complete description of the analysis and the results of the smooth modelling is provided in Ritondale et al. (2019a), along with a detailed comparison with the smooth models derived by Shu et al. (2016a). In this section, we present the results of our search for low-mass haloes.

4.5.1 subhalo search

Out of the 17 gravitational lenses in the sample, we find that 14 do not fulfil one or more of the detection criteria defined in Section 4.3.5 and, therefore, all the pixels in these systems will contribute to the statistical analysis as non-detections. In particular, in all of these 14 cases, the smooth model is always preferred by the Bayesian evidence, independently of the choice of prior. Moreover, no significant convergence corrections are identified. For the remaining three systems, namely SDSS J0742+3341, SDSS J0755+3445 and SDSS J1110+3649, we find that the Bayesian Evidence persistently prefers a model that includes the presence of one or more subhaloes, however, the potential corrections give a meaningful perturbation only in the case of SDSS J1110+3649. Below, we discuss these systems individually in more detail.

SDSS J0742+3341

The parametric analysis of Section 4.3.4, where subhaloes are described as analytical NFW mass components, shows a persistent preference for a model that includes a subhalo with a mass of $M_{\rm vir}^{\rm NFW} = (3.8 \pm 0.8) \times 10^{10} M_{\odot}$ located at $(dx, dy) = (1.14 \pm 0.04, -0.80 \pm 0.03)$ arcsec, relative to the main lens centre. However, the detection is only at the 6-σ level and therefore below our 10-σ threshold (see Section 4.3.5). Moreover, no significant and localized convergence correction is identified by the pixellated analysis of Section 4.3.3 at the same location, as shown in Fig. 4.3. We, therefore, conclude that there is no evidence for a significant detection of a mass perturbation in this system and register it as another non-detection in the sample.

SDSS J0755+3445

This system is a clear example of how a purely analytical analysis of mass substructure can lead to false detections due to a mis-modelling of the main lens macro model. We refer to Chapter 3 for an in-depth discussion of this system and related issues with the lens macro-model. Here, we provide a short summary of the results. The analytical clumpy analysis shows a consistent preference at the 12σ level (i.e. $\Delta \log \mathcal{E} = 72$) for a model using a NFW halo with a mass of $M_{\rm vir}^{\rm NFW} = (4.8 \pm 0.4) \times 10^{10}$ M$_{\odot}$ located at $(dx, dy) = (-1.76 \pm 0.02, 1.12 \pm 0.02)$ arcsec, relative to the main lens centre. However, no strong positive and localized convergence correction is identified. Low-level diffuse corrections can be seen instead (see Fig. 4.3), which allow for a better focusing of the background source and reduce the positive and negative beating otherwise seen in the low-surface brightness tail of the smooth source. This indicates that the true mass distribution of this system is probably not well described by a single power-law model and that the compactness of the gravitational imaging source is probably due to the extended convergence corrections shown in Fig. 4.3.

Moreover, we find that the Bayesian evidence further increases when adding a second analytic subhalo. The source tail is also further decreased, although we do not see evidence for this second halo in the gravitational imaging as a localized positive correction either. We have also modelled the data using a double power law model and including the contribution to the lensing potential of a galaxy observed in the south-west direction and ∼5 arcsec away from the main lens. However, in none of these cases could we reconstruct a compact source and remove the low-level diffuse potential corrections. We conclude therefore that complex mass components that remain uncaptured by the macro-model can mimic the effect of subhaloes and lead to an overestimation of the latter.

This result is in qualitative agreement with what was found by Hsueh et al. (2016, 2017), who have shown that observed flux-ratio anomalies in multiply imaged quasars can sometimes be reproduced by the lensing effect of an un-modelled edge-on disk rather than requiring dark matter (sub)haloes. Similarly, from an analysis of hydrodynamical simulations, Hsueh et al. (2018) have shown that the presence of baryonic structures and disks is responsible for an increase of flux-ratio anomalies by a factor from 8 to 20 per cent. They also found that baryonic structures can cause astrometric anomalies in 13 per cent of the studied mocks. Gilman et al. (2017) have come to the same conclusion by analysing mock data based on *HST* observations of low-

redshift galaxies. Moreover, Gomer & Williams (2018) found that astrometric anomalies can also be caused by asymmetries and inhomogeneities in the region of the lensing galaxy where the transition between dark and baryonic matter occurs.

This demonstrates that the gravitational imaging technique is important to distinguish between genuine detections and false detections due to an un-captured underlying complexity of the lensing mass distribution.

SDSS J1110+3649

The pixellated analysis for SDSS J1110+3649 shows the presence of a positive localized convergence correction at about $(dx, dy) = (-0.851, 0.628)$ relative to the main lens (Fig. 4.3). Moreover, the parametrized analysis of Section 4.3.4 gives a preference at the 4-σ level for a model with a subhalo with mass $M_{\rm vir}^{\rm NFW} = (5.4 \pm 1.5) \times 10^9 M_\odot$. This subhalo is located at $(dx, dy) = (-0.945 \pm 0.084, 0.536 \pm 0.021)$ relative to the main lens centre, consistent within 1σ with the position of the convergence correction. From the pixellated convergence corrections, we derived a model-independent projected mass for the subhalo of $M_{\rm 2D}^{\kappa}(< r_{\rm s}) = \sum_{pix} 2\,\pi\,\Sigma_c\,\kappa_i\,r_i^2 = 2.5 \times 10^9 {\rm M}_\odot$. This is consistent within 2σ with the parametric projected mass $M_{\rm 2D}^{\rm NFW}(< r_{\rm s}) = (1.7 \pm 0.7) \times 10^9 {\rm M}_\odot$.

However, given the low statistical significance and the results presented in Section 4.3.5, we conclude that multi-band data or deeper observations are required to understand the nature of this system and, at present, also in this case we do not count this as a detection.

4.6 Inference on the dark matter parameters

In this section, we combine the lens modelling results presented in Section 4.5 with the statistical formalism introduced in Section 4.4 to derive statistical constraints on the free streaming properties of dark matter. First, we compare with the expected value of detectable line-of-sight haloes from the CDM paradigm (i.e. $\alpha = 1.9$, $M_{\rm hm} = 0$, Springel et al. 2008) and then with resonantly produced sterile neutrino models (Shi & Fuller 1999) including the contribution of both subhaloes and line-of-sight haloes.

4.6.1 Sensitivity function

We firstly compute the sensitivity function for the BELLS GALLERY sample, as described in Section 4.4.4. As discussed in the same section, the high level of structure of the sources could in principle provide a high sensitivity to low-mass haloes at fixed signal-to-noise. However, this was found not to be the case: the BELLS GALLERY lenses not only have a mean sensitivity that is lower than the SLACS lenses (see Fig. 4.4), but also, as the background sources are very compact, have a smaller fraction of image plane pixels with a high sensitivity than SLACS. For this reason, this sample of lenses turned out to be less constraining than the SLACS lenses in terms of probing the halo and subhalo mass function at an interesting mass regime. Higher signal-to-noise ratio observations are required to improve the sensitivity of this sample.

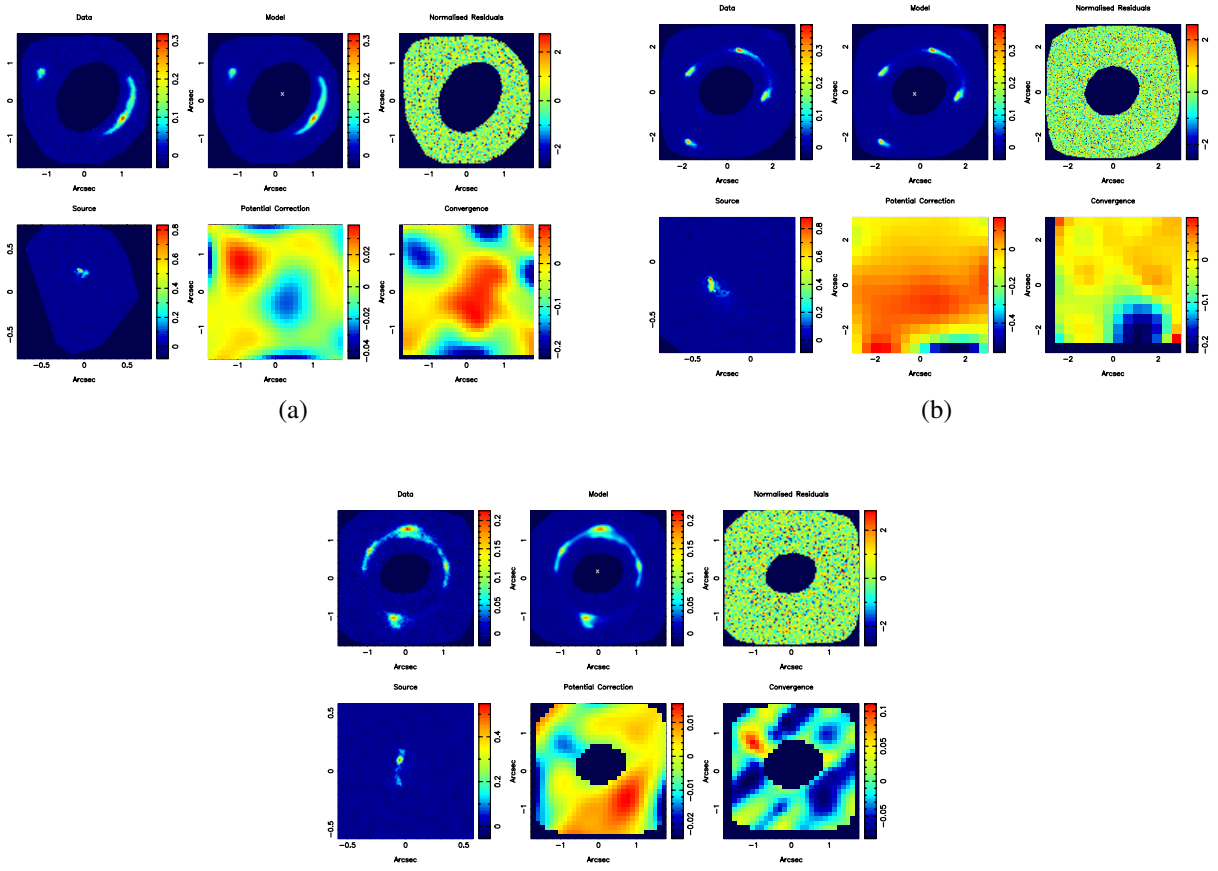

(a) (b)

(c)

Figure 4.3: Results of the gravitational imaging analysis for the lens systems SDSS J0742+3341 (Panel a), SDSS J0755+3445 (Panel b) and SDSS J1110+3649 (Panel c). For each lens, the top-row shows the data (left), the model (middle), the normalised residuals (right). The bottom-row shows, the reconstructed source (left), the pixellated potential corrections (middle) and the corresponding convergence corrections (right). In SDSS J0742+3341 the convergence corrections are in correspondence of the lens galaxy, but their low-level and wide extension suggest the absence of small size haloes. SDSS J0755+3445 also shows low-level and diffused corrections to the potential; this is a symptom of a complicated mass distribution rather than of the presence of a subhalo. In SDSS J1110+3649 we see the presence of a positive and localized potential correction, possibly indicating the tentative detection of a dark matter halo of mass $M^{\kappa}_{\rm 2D}(< r_{\rm s}) = 2.5 \times 10^{9} {\rm M}_{\odot}$. In all the panels, negative potential corrections are related to the conservation of the integral of the convergence, i.e. the mass.

4.6.2 A potential discrepancy with CDM

Assuming our reference detection threshold of 10σ and the relative sensitivity function, we compute the number of detectable line-of-sight CDM haloes to be $\mu_l = 1.17 \pm 1.08$, for the complete sample of 17 systems, in agreement with the zero detections registered for this sample. This is computed with equation (4.16) using the the lowest detectable (at the 10-σ level) mass in each pixel as the lower integration limit and summing over all 17 lenses. This result is consistent with the fact that this sample has relatively low sensitivity (i.e. large value for the lowest detectable mass) and thus the number of line-of-sight haloes per arcsec or per pixel is relatively small.

Although the tests presented in Section 4.3.5 have shown that a detection threshold cut at the 5-σ level is not reliable, it is interesting to test what happens if the sensitivity improved to the level implied by this less conservative threshold. As can be seen in the bottom panel of Fig. 4.4, the sensitivity at the 5-σ cut of the BELLS GALLERY sample is closer to the 10-σ level one of the SLACS lenses, with a tail at lower masses. As a consequence of the improved sensitivity, the number of detectable CDM line-of-sight haloes significantly rises to $\mu_l = 9.0 \pm 3.0$, while we find that also at the 5-σ level, the number of detections in the sample is still zero. The unreliability of this sensitivity cut doesn't allow us to draw robust conclusions, but the probability of registering zero detections in the CDM framework would be $\mathrm{P}^{5\sigma}_{\mathrm{CDM}}(n_{\mathrm{det}} = 0)$=0.0001. Interestingly, Vegetti et al. (2018) have found that the expected number of CDM line-of-sight haloes at the 10-σ level for the SLACS lenses is $\mu_l = 0.8 \pm 0.9$ (in agreement with the single detection reported by Vegetti et al. 2014), reflecting the lower size of the cosmological volume probed by this sample. These results indicate that deeper exposures or multi-band data, that provide improved sensitivity whilst keeping the robust 10-σ threshold, for the BELLS GALLERY sample hold significant promise to find a possible strong tension between the CDM model and the sample of lenses considered here.

4.6.3 Dark matter mass function

In the previous section, we only looked at the total expected number of line-of sight haloes, here we use the full results of the Bayesian analysis (with the 10-σ level cut) to characterize the dark matter model based on the total number of detections and non-detections and using the priors described in Sections 4.4.6. We summarize our constraints on the subhalo and line-of-sight halo mass function parameters in Table 4.2. Specifically, we report the mean, and the upper and lower limits at the 68 and 95 per cent confidence level for α and β, the 68 and 95 per cent upper limit on the dark matter mass fraction in subhaloes f_{sub}, and the 68 per cent and 95 per cent level upper and lower limits for the half-mode mass M_{hm}. The posterior probability distributions for these last two parameters obtained with the BELLS GALLERY sample are presented in Fig. 4.5. We have constrained the half-mode mass to be $\log M_{\mathrm{hm}} < 12.60$ at the 2-σ level. As expected from the calculations in Section 4.6.1, our results are in agreement with the CDM paradigm, but do not allow us to rule out alternative warmer dark matter models.

Recently, Vegetti et al. (2018) have performed a similar analysis with a sample of 11 gravitational lens systems from the SLACS survey by combining the single detection of Vegetti et al. (2010b) with the non-detections reported by Vegetti et al. (2014). The substructure mass fraction

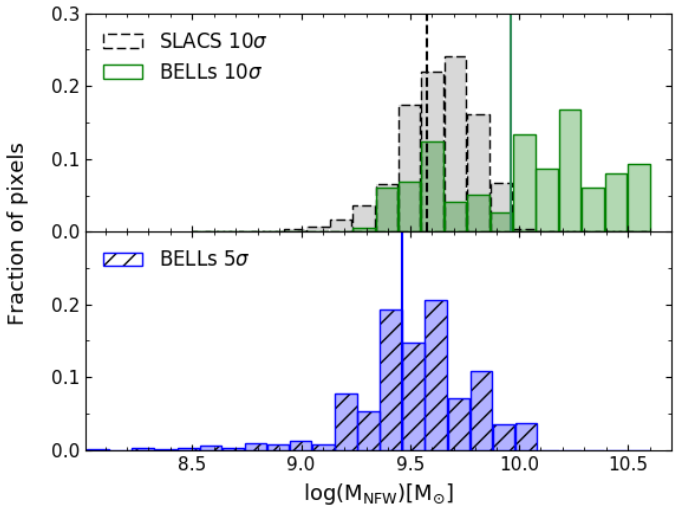

Figure 4.4: The upper panel shows the fraction of pixels with a 10-σ subhalo mass detection threshold (as defined in Section 4.4.4) for the BELLS GALLERY sample (green histogram) and for the sub-sample of SLACS lenses analysed by Vegetti et al. (2014, grey histogram). The lower panel shows the same for the BELLS GALLERY sample but with a 5-σ subhalo mass detection threshold. The vertical lines indicate the mean sensitivity values for each sample.

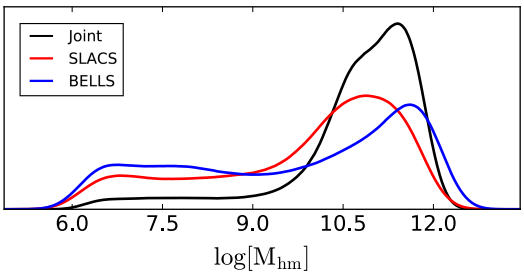

Figure 4.5: The posterior probability density distribution for the half mode mass $M_{\rm hm}$ for the joint and individual samples.

derived here is smaller than the value reported by Vegetti et al. (2018), which is contrary to what one would expect given the relative redshift of the two samples of lenses (high redshift for the BELLS GALLERY and low redshift for the SLACS sample), however this is just a reflection of the poor data sensitivity, as shown in Fig. 4.4, and the small number statistics combined with the null detection. Also, it should be noted that the definition of $f_{\rm sub}$ adopted here (total mass fraction in subhaloes) is different than the one adopted by Vegetti et al. (2014, 2018, dark matter mass fraction in subhaloes).

In Fig. 4.5, we plot the joint posterior probability distribution for $M_{\rm hm}$ derived by combing a posteriori the analysis of the two sample of lenses. It has to be noted that we do not provide a joint inference on $f_{\rm sub}$ as its definition is different for the two samples and it is expected to change with the mean lens redshift of the sample (Xu et al. 2015). In Table 4.2 we also show the 95 and 68 per cent upper and lower limits on the half-mode mass derived from the joint analysis of the SLACS and BELLS GALLERY samples. It is evident that the constraints at the lower 95 per cent confidence limits are driven by the SLACS sample, while the upper limits are driven by the BELLS GALLERY sample and are now consistent with warmer models, that is the joint 95 per cent upper limit has shifted towards larger values from what was derived using the SLACS sample only. This can be explained as follows: when combining the two samples, the number of detections is the same, that is one, while the number of non-detections significantly increases with the number of pixels in each lens system included in the analysis. The subhalo detection in the SLACS sample is also responsible for a significant change in the inference on the half-mode mass $M_{\rm hm}$. In fact, the lower limit on $M_{\rm hm}$ raises by 3 and 1 dex at the 68 and 95 per cent confidence level, respectively. This is due to the fact that the single, rather massive detection from the SLACS sample requires a cooler dark matter model, and therefore smaller values of $M_{\rm hm}$, as clearly visible in the derived posterior probability in Fig. 4.5.

In Fig. 4.6, we compare the differential line-of-sight halo mass function derived here with the one predicted by the CDM model (black solid line) and a sterile neutrino model consistent with the 3.5 keV emission line (red solid line). The latter falls within our lower and upper 95 per cent confidence limits, respectively plotted as the green and yellow solid lines. Our lower limit mass function is consistent at the 2-σ level with the CDM prediction within the mass range probed by the data. The inability to disentangle CDM and warmer models, is due to the relatively low sensitivity of the data to low-mass haloes, represented by the grey shaded region. In practice, this data can only probe the higher-mass end of the halo and subhalo mass functions, where different dark matter models do not significantly differ from one another (Despali et al. 2018). As discussed by Vegetti et al. (2018), the same sample of lenses with a sensitivity improved by one or two orders of magnitude would result in a shift of the posterior distribution of the half-mode mass towards larger values and create a tension with CDM at the 2-σ level. This clearly indicates the importance of obtaining higher-quality data for the joint sample.

In Fig. 4.7, we show how our results compare with sterile neutrino dark matter models. Sterile neutrinos are a two-parameter dark matter model whose *coolness* is determined by a combination of the level of lepton asymmetry L_6 in the early Universe and the mass of the sterile neutrino $m_{\rm s}$ (Shaposhnikov 2008; Lovell et al. 2017a). This is evident from Fig. 4.7, where $M_{\rm hm}$ oscillates with L_6 for each value of $m_{\rm s}$. On the left panel of Fig. 4.7 we plot the half-mode mass $M_{\rm hm}$ against the lepton asymmetry $\rm L_6$ for different values of the sterile neutrino particle mass. On the right

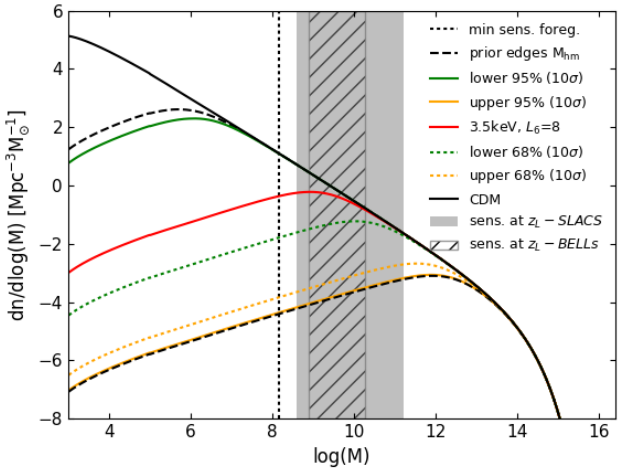

Figure 4.6: Line-of-sight mass functions derived from the joint SLACS+BELLS GALLERY dataset. The black line corresponds to the ΛCDM framework, the red to the sterile neutrino dark matter model compatible with the detection of the 3.5 keV line, and the yellow and green respectively to the upper and lower limits at the 95 (solid line) and 68 (dashed line) per cent confidence levels found here, assuming a 10-σ detection threshold. The black dashed lines correspond to the prior edges in $M_{\rm hm}$. The striped and shaded grey regions correspond to the sensitivity of the BELLS GALLERY and the SLACS samples, and the dotted line shows the lowest detectable line-of-sight halo mass with the joint sample.

panel instead, we compare our results with those derived from the observed satellites in the Milky Way (Lovell et al. 2016), X-ray decay searches from M31 (Watson et al. 2012; Horiuchi et al. 2014) and Lyman-α forest constraints (see Vegetti et al. 2018, for a detailed description). We notice that our joint lower limit constraints are not visible because they are beyond the plotting range. The upper 95 per cent confidence limit rules out sterile neutrino masses $m_{\rm s} < 0.8$ keV at any value of the lepton asymmetry L_6. As for the SLACS-only results, our exclusion regions are significantly smaller than those derived by other astrophysical probes. For the SLACS lenses, this is mainly due to the low redshift of the lenses and the sources, which results in a small contribution from the line-of-sight. For the BELLS GALLERY sample, this is instead related to the lower sensitivity of the data. Indeed, as discussed in Section 4.6.1, the same sample of lenses but with higher data quality than currently available would have led to a significantly larger number of expected line-of-sight haloes. Finally, it should be noted that, although our results are currently weaker, they are more robust than those from the Milky-Way satellite counts and the Lyman-α forest, as they are less affected by feedback processes and do not depend on the unknown thermal history of the intergalactic medium, and our limits are therefore less model dependent.

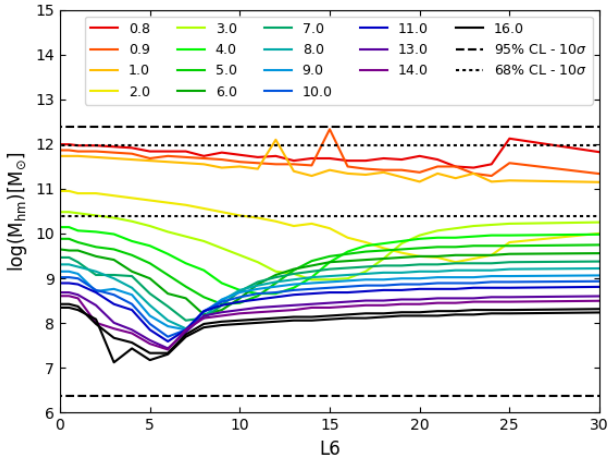

(a)

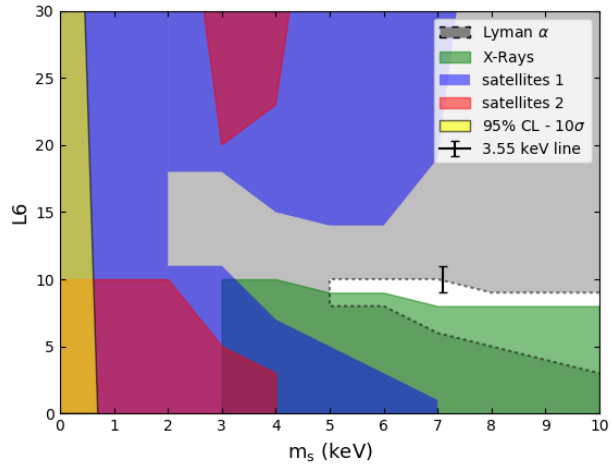

(b)

Figure 4.7: Left: Half-mode mass versus lepton asymmetry L_6 for different values of the sterile neutrino mass with upper and lower limits at the 95 and 68 per cent confidence level on the turnover mass (dashed and dotted black lines). Right: 95 per cent exclusion region in the L_6 versus sterile neutrino mass m_s plane. The grey region has been excluded by the Lyman-α forest, the green region is excluded by the missed detection of X-ray decay in Andromeda, and the blue and red regions are excluded by satellite counts in the Milky Way with two different feedback models. The yellow region is excluded at the 95 per cent confidence level by the detections and non-detections in the joint SLACS+BELLS GALLERY sample. Only our upper limit is visible, since the lower limit we set lies outside the mass range of this plot, being much higher than the masses constrained by other methods. The black error bar corresponds to the dark matter model explaining the 3.5 keV line.

Table 4.2: Inference on the dark matter parameters with the BELLS sample and the joint BELLS and SLACS samples. We report the mean and the lower and upper limit at the 68 and 95 per cent confidence level for α and β, while we only report the upper and lower limits for the half mode mass $M_{\rm hm}$ and the upper limits on the dark matter fraction in subhaloes at the 68 and 95 per cent level.

Run	Parameter	mean	σ_{68}	σ_{95}
BELLS	α	1.90	-0.19 | $+0.19$	-0.33 | $+0.37$
	β	-1.30	-0.1 | $+0.09$	-0.16 | $+0.16$
	$f_{\rm sub}$		<0.01	<0.07
	$\log M_{\rm hm}[M_\odot]$		6.52 | 12.12	5.77 | 12.60
Joint	$\log M_{\rm hm}[{\rm M}_\odot]$		10.38 | 11.85	7.27 | 12.26

4.7 Summary & conclusions

We have analysed a sample of 17 gravitational lens systems from the BELLS GALLERY survey with the aim of detecting low-mass dark matter haloes within the lensing galaxies and along their lines of sight. First, we have modelled each system in the sample with a smooth power-law elliptical mass model assuming the presence of no haloes and studied the intrinsic properties of the background sources (Ritondale et al. 2019a). In this paper, we have focused on the detection of low-mass haloes and its implication for the dark matter properties, in particular those of sterile neutrinos.

Our main results can be summarised as follows. For the entire sample of lenses, we report no significant detection of subhaloes and line-of-sight haloes. In particular, 14 systems show statistical preference for a model that does not include the presence of any halo; one system, SDSS J0742+3341, shows a small preference for a model with a subhalo, however this was not confirmed by our gravitational imaging analysis. The system SDSS J1110+3649 also shows a preference for a small-mass subhalo with a corresponding significant pixellated convergence correction. However, its statistical significance is still below our 10-σ detection threshold and we, therefore, conclude that more data is required to draw final conclusions on this system.

Hsueh et al. (2016, 2017) have shown that un-modelled edge on-disks and other baryonic structures in early-type galaxies can cause flux-ratio and astrometric anomalies in multiply imaged quasars, similarly to dark matter (sub)haloes. A similar conclusion was reached using realistic lens galaxies taken from numerical simulations and mock data based on *HST* observations of low-redshift galaxies (Hsueh et al. 2018; Gilman et al. 2017). On the same note, our analysis of the lens system SDSS J0755+3445 has shown how structure not readily visible in the imaging data might affect the lensing and therefore how complex mass distributions can potentially lead to the false detection of mass substructure. This result is particularly important to show how a

pixellated gravitational imaging analysis can be used to distinguish between the two scenarios.

Assuming a sensitivity function for the detection of subhaloes based on a 10-σ cut and applying the mass-redshift relation by Despali et al. (2018), we have derived the total expected number of CDM line-of-sight haloes for our entire sample to be $\mu_l = 1.17 \pm 1.08$, in agreement with our null detection. Our results are therefore consistent with the ΛCDM model, under our most conservative assumption on the subhalo detectability. Interestingly, if we were to relax our assumptions and adapt a 5-σ cut, the number of detectable line-of-sight haloes raises significantly to $\mu_l^{5\sigma} = 9.04 \pm 3.01$, that would potentially be in strong tension with our results that point to zero detections also at this sensitivity cut. However, we have extensively tested our detections and non-detections at the 5-σ confidence level and we have found a high percentage of false positive and false negatives. We conclude therefore that the currently available data for this sample does not allow us to draw robust conclusions at the 5-σ level. Therefore, deeper exposure (we note that the sensitivity improves non linearly with the data quality) or multi-band data are required to improve the sensitivity whilst keeping the robust 10-σ threshold and consequently to find a potential strong discrepancy with the standard cosmological model.

We have used the BELLS GALLERY lenses to infer the dark matter mass function and constrained the half-mode mass to be $\log M_{\rm hm} < 12.60$ at the 2-σ level. If we combine our results with those derived by Vegetti et al. (2018) from a subsample of the SLACS lenses, our constraints drop to $\log M_{\rm hm} < 12.26$ at the same confidence level. An interesting result is the significant change in the inference on the dark matter model parameters when even just one detection is included. In fact, we register a shift of 3 dex on the 68 per cent lower limit for $M_{\rm hm}$ after combining the two samples. More sensitive data is necessary to significantly improve the constraints at the 95 per cent confidence level.

Assuming that the dark matter is composed by resonantly produced sterile neutrinos, we have then derived a 95 per cent confidence level exclusion region for the sterile neutrino mass and the lepton asymmetry in the early Universe, which is significantly smaller than the constraints obtained with other astrophysical probes, such as the number of Milky Way satellites and the Lyman-α forest. Specifically, our current results are consistent with the CDM paradigm, but do not allow us to rule out alternative warmer dark models. This is due to the limited sensitivity of the current data, which only allows us to probe the high-mass end of the dark matter mass function, where different dark matter models predict a similar number density of subhaloes and line-of-sight haloes.

In the future, observations of strong gravitational lens systems with a redshift distribution similar to the BELLS GALLERY sample considered here, but with a higher data quality (i.e. higher signal-to-noise ratio) will allow us to set tighter and robust constraints on the nature of dark matter.

Chapter 5

Conclusions and future prospects

5.1 Thesis highlights

Strong gravitational lensing is a powerful tool to study the detailed properties of high-redshift galaxies and, at the same time, constrain the properties of dark matter. In this thesis, we have presented the results of a lens modelling analysis of a sample of seventeen gravitational lens systems from high-quality HST data. The main goal of this study was two-fold. First, we have investigated the detailed physical properties of the background Lyman-alpha emitters on sub-kpc scales. We have found these galaxies to be very compact, with an inferred median half-major axis of 561^{+13}_{-110} pc, and characterised by potentially very small SFRs, i.e. median non-dust-corrected SFR of 1.4 $M_{\odot} yr^{-1}$. We expect a dust corrected value that is from 4 to 6 times larger, in agreement with what has been derived by studies of non-lensed Lyman Alpha emitters. Our inferred median size is comparable to the lower-limit found by non-lensed studies and in general, shows that these objects are even more compact than what found to date. Their morphology is even more interesting, suggesting that these objects present clumpy regions of high star formation activity and, in some cases, are composed of two objects potentially merging.
The second goal of this thesis was to deliver robust constraints on the halo mass function in the mass regime probed by the data and thereby constrain the properties of dark matter. We have found the data to be consistent with the lack of low-mass haloes with masses between 10^8 and 10^{11} $M_{\odot}$, in agreement with expectations from the CDM paradigm. We have also found that higher quality data are required to probe the halo mass function at lower halo-masses where predictions from CDM and WDM sterile neutrinos differ the most. In particular, an improvement of the signal-to-noise ratio by a factor of 2, would lead to a probability of the CDM model of $P_{CDM}(n_{det} = 0)$=0.0001, if our current lack of detections were to be confirmed.
Below, we summarise the main results of our work in more details.

5.1.1 Constraints on the Lyman-α emitting sources

We have analysed seventeen gravitational lens systems from the BELLS GALLERY sample (Bolton et al. 2006). This is the first statistically significant sample of LAEs at $z \sim 2.5$, gravita-

tionally lensed by massive early-type galaxies at $z \sim 0.5$.

We have modelled the gravitational potential of all of the systems in the sample using a power-law mass distribution plus external shear and simultaneously inferred the surface brightness distribution for the lensing galaxies. We have found that most of the deflectors are well described by a power-law mass-density profile, which is close to being isothermal with $< \gamma' >= 2.00 \pm 0.01$ and consistent with previous studies of ETG lenses in different samples such as the SLACS, the SL2S and BELLS (Auger et al. 2010; Ruff et al. 2011; Bolton et al. 2012; Sonnenfeld et al. 2013). We have studied the intrinsic properties of the UV-continuum of the reconstructed LAEs at $z \sim 2.5$, finding that they have a median integrated SFR of $1.4^{+0.06}_{-0.07}$ $M_\odot$ yr^{-1} and a peak SFR intensity between 2.1 to 54.1 $M_\odot$ yr^{-1} kpc^{-2}. We find that these objects are quite compact with a median semi-major axis of 561^{+13}_{-110} pc and distribution ranging from a minimum of 0.2 to a maximum of 1.8 kpc. In many cases, they present complex morphologies with multiple compact components well separated in the sky by 0.4 to 4 kpc (see also Cornachione et al. 2018). *The rate of detection of these multiple component objects is less than 30% in the literature of non-lensed studies, while more than 50% of the reconstructed sources in our sample show this kind of structure. Moreover, our lower limit to the intrinsic size is about a factor of two smaller than that found for non-lensed LAEs. Both these results highlight the power of gravitational lensing and sophisticated lens modelling techniques for resolving such objects in the high redshift Universe. Most importantly, we find that the LAEs are quite elliptical, with a median axial-ratio of* 0.51 ± 0.01. *This morphology is consistent with disk-like structures of star-formation for nearly 80 per cent of the sample, which would rule out models where the Lyman-α emission is only seen perpendicular to the disk, and favours clumpy models for the escape lines-of-sight for Lyα (Rivera-Thorsen et al. 2015).* This result is in agreement with the findings of non-lensed LAEs studied at similar redshifts but is more robust, given the improved angular resolution of our analysis. We also find that 14 per cent of the sample has off-axis components that may be associated with mergers, which is again consistent with the study of non-lensed LAEs. Overall, the morphologies of the LAEs in our sample agree quite well with other published results, where the effective angular resolution is lower and stacking techniques are needed.

5.1.2 Complexity of the lensing mass distribution and its consequences

In the second part of this thesis, we have investigated the complex nature of real galaxies compared to the standard simplifying assumptions which are generally made when modelling the mass distribution of lens galaxies and its degeneracy with the presence of subhaloes.
The analysis of the gravitational lens system SDSS J0755+3445 with a simple parametric lensing mass, either in the form of a single or double power-law model with external shear, has lead to a high-quality reconstruction of the observed surface brightness distribution, with image residuals which are at the noise level. However, in both cases, the reconstructed source has an unfocused morphology and presents an elongated surface brightness tail of positive and negative beating, indicating that our best lens model is not correctly reproducing the true lensing potential. From a gravitational imaging analysis, i.e. adding linear pixellated corrections to the main potential, reveals the presence of a diffuse and complex mass distribution, of unclear nature. Interestingly, the inclusion of this additional structure allows us to obtain a more compact and focused source mor-

phology with a much less pronounced tail. On the other hand, when extra complexity is added to the model in the form of spherical NFW subhaloes, we find a strong statistical preference for these updated models with a marginalised Bayesian evidence that increases with the number of included subhaloes, and with inferred positions of the NFW haloes which are consistent with the strongest peaks of the pixellated convergence reconstruction. However, the inclusion of these subhaloes still leads to a non-properly focused source. Moreover, their presence is actually excluded from the fact that they would lead to strong and localized convergence corrections rather than low-level diffuse ones as observed for this system. *Our findings indicate that complexity in the mass distribution of the lensing galaxy can mimic the effect of low-mass dark matter haloes and can lead to false detections at a high statistical level.* These results are in agreement with those by Hsueh et al. (2016, 2017, 2018), who have shown that the presence of an inclined disc can explain the flux-ratio anomalies in the gravitational lens systems CLASS B0712+472 and CLASS B1555+375, without the need for additional dark matter subhaloes. Analogous results are also found from simulations, where in 13 per cent of the cases baryonic effects can mimic astrometric anomalies caused by low-mass dark-matter haloes.
Finally, we have also found that failure to include higher-order complexity in the lensing potential also leads to an overestimation of the reconstructed source sizes by a factor of 20 to 27% and of their SFRs by a factor of 10%. *Our results clearly demonstrate the importance of pixellated corrections not only in differentiating between different sources of complexity in the lensing potential (i.e. baryonic structures vs dark matter substructure), but also to obtain a reliable reconstruction of the background source galaxies.*

5.1.3 Inference on the nature of dark matter

In the last chapter of this thesis, we have proceeded with a gravitational imaging analysis of the BELLS GALLERY sample to search for the presence low-mass dark-matter haloes within the lensing galaxies and along their lines of sight. Successively, we have derived the implications for the dark matter properties, in particular, those of sterile neutrino dark matter models.

For the entire sample of lenses, we report no significant detection of subhaloes and line-of-sight haloes. We firstly assume a sensitivity function for the detection of subhaloes based on a marginalised Bayes difference of 50 in logarithmic scale. Under the assumption of statistical Gaussian errors this corresponds to a 10-σ detection threshold. By applying the mass-redshift relation by Despali et al. (2018), we have derived the total expected number of detectable CDM line-of-sight haloes for our entire sample to be $\mu_l = 1.17 \pm 1.08$, which is in agreement with our null detection. *Therefore our results are consistent with the ΛCDM framework.* If we relax our assumptions on the subhalo detectability and adopt a marginalised Bayes difference of 12 (corresponding to about a 5-σ cut), the number of expected detectable CDM line-of-sight haloes raises significantly to $\mu_l^{5\sigma} = 9.04 \pm 3.01$. *In case our null detection would be confirmed at this sensitivity cut, our results would potentially be in strong tension with the predictions from the CDM model and in particular, the latter would have a probability of $P^{5\sigma}_{\rm CDM}(n_{\rm det} = 0)$=0.0001.* However, we have extensively tested our detections and non-detections at the 5-σ confidence level, and we have found that the currently available data for this sample does not allow us to draw robust conclusions at this sensitivity cut. Therefore, we have concluded that either deeper-

exposure (we note that the sensitivity improves non-linearly with the data quality) or multi-band data are required to improve the sensitivity while keeping the robust 10-σ threshold.

We have then inferred the dark matter mass function with the BELLS GALLERY sample and constrained the half-mode mass to be $\log M_{\rm hm} < 12.60$ at the 2-σ level. We also combine our results with those derived by Vegetti et al. (2018) from a sample of 11 SLACS lenses including a detection of a subhalo of mass $M_{\rm sub} = (3.51 \pm 0.15) \times 10^9$ $M_\odot$. The joint constraints drop to $\log M_{\rm hm} < 12.26$ at the same confidence level. *Interestingly, we register a significant change in the inference on the dark matter model parameters when even just one detection is included*. In fact, we find a shift of 3 dex on the 68 per cent lower limit for $M_{\rm hm}$ after combining the two samples. More sensitive data is necessary to significantly improve the constraints at the 95 per cent confidence level.

Assuming that dark matter is made of resonantly produced sterile neutrinos, we have then derived a 95 per cent confidence level exclusion region for the sterile neutrino mass and the lepton asymmetry in the early Universe. *Our current results are consistent with the CDM paradigm, but do not allow us to rule out alternative warmer dark models. This is due to the limited sensitivity of the current data, which only allows us to probe the high-mass end of the halo mass function, where different dark matter models predict a similar number density of subhaloes and line-of-sight haloes*.

5.2 Future prospects

Based on the main conclusions of this thesis, our goals for the immediate future is to obtain higher quality data for the BELLS GALLERY sample considered here as well as high-quality observations of new strong gravitational lens systems with a similar redshift distribution. The high redshift distribution of the sources is fundamental to significantly increase the number of potential detectable line-of-sight haloes. Moreover, an improved signal-to-noise ratio of the data, as well as a better angular resolution, both guarantee a higher sensitivity and therefore capability to detect lower mass objects when present. Equipped with these new and high-quality data-sets, we will be able to derive the following improved constraints:

- we will be able to even better resolve the structure of the background lensed LAEs in the BELLS GALLERY sample and verify the nature of the detected clumpy star formation regions. Having access to the detailed spectroscopical features of the Lyman-α line and its flux, we will include the study of the properties of the Lyman-α escape fraction and equivalent width, as well as study the morphology of the extended Lyman-α halo. Moreover, colour information will allow us to identify the present merging objects in the sample and possibly study the kinematics of these sources. These results would not only improve the current constraints on these sources but could give further insights on the role that similar galaxies at higher redshift have had in reionising the Universe.

- The colour information and the higher signal to noise will allow us to further constrain the complexity in the lensing mass distribution for the lensing system SSDSS J0755+3445 of the BELLS GALLERY sample. In particular, once the origin of the diffuse and complex

mass component will be clear, a robust analysis of the content of small mass haloes of this system will be performed.

- the improved sensitivity will allow us to detect much lower masses at the $\Delta \log E = 10$ detection threshold. In case the null detection in the sample will be confirmed, this will rule out the CDM framework at a strong statistical level, i.e. $P^{10\sigma}_{\rm CDM}(n_{\rm det} = 0)$=0.0001.

In the near future, we will be focusing on data from the Strong Lensing at High Angular Resolution Program (SHARP Lagattuta et al. 2012), which is based on Keck-II Adaptive Optics observations. These data have an improved angular resolution, which is two times better than provided by the HST, and they span a wide redshift range: respectively $0.2 < z_l < 0.8$ for the lenses and $0.5 < z_s < 3$ for the sources. The combination of these two factors will result in a significantly improved sensitivity of the data to haloes with a mass as low as M~$10^8 M_\odot$ and a large probed cosmological volume.

Over the course of the next five to ten years, strong gravitational lensing will undergo a significant development thanks to upcoming large surveys that will cover areas of a few 10^4 deg^2 and will significantly increase the number of known strong lensing systems. Euclid and Large Synoptic Survey Telescope (LSST), in paritcular, will deliver optical samples consisting of ~10^5 objects (LSST Science Collaboration et al. 2009) and the same order of magnitude of radio data is expected to come from observations with Square Kilometre Array (SKA McKean et al. 2015). Ongoing surveys, as the Kilo Degree Survey (KiDS) and the Dark Energy Survey will provide samples of slightly lower size, consisting of $\sim 10^3$ lens systems (de Jong et al. 2015). These numbers of objects are substantially higher than what is currently available. For example, the current largest homogeneous sample of gravitational lens systems, the SLACS sample (Sloan Lens ACS Survey), only consists of ~100 lenses (Bolton et al. 2008), and the total number of known galaxy-scale lenses is lower than 10^3. Such a dramatic increase in the samples size will allows us to collect information over a wide range of galaxy masses, redshifts and environment. This unprecedented abundance of data will give us the possibility to carry out significantly advanced studies in many fields. Among these, it will be possible to test hierarchical galaxy formation and dark matter models by increasing the sensitivity to the luminous and dark content of galaxy haloes, and more precisely to low-mass dark haloes, both with flux ratio anomalies in quadruply imaged quasars (Oguri & Marshall 2010) and astrometric perturbations in highly magnified Einstein rings (Collett 2015). Follow-up observations with telescopes such as the James Webb Space Telescope (JWST) and the Extremely Large Telescope (E-ELT) will provide high-resolution observations of lens systems with source redshift up to z~5, allowing us not only to study the detailed properties of high-redshift galaxies but also to potentially detect the large number of low-mass line-of-sight haloes that are predicted by the CDM paradigm.

Finally, high expectations in terms of constraints on the dark matter halo mass functions lie on Very Long Baseline Interferometry (VLBI) radio data. Observations of radio-loud extended sources at cm-wavelengths provide us with an exquisite angular resolution and allow us to resolve the lensed images with a precision of few milli-arcseconds. This extremely high resolution is proven to be especially useful in testing the smoothness of the mass distribution of the lensing galaxy haloes, allowing the detection of small mass dark matter haloes down to masses of 10^6 $M_\odot$ (Li et al. 2016; Spingola et al. 2018).

Bibliography

Ahlen, S. P., Avignone, F. T., Brodzinski, R. L., et al. 1987, Phys. Lett., B195, 603, [,URL(1987)]

Alavi, A., Siana, B., Richard, J., et al. 2014, Astrophysical Journal, 780, 143

Atwood, W. B., Abdo, A. A., Ackermann, M., et al. 2009, Astrophysical Journal, 697, 1071

Auger, M. W., Treu, T., Bolton, A. S., et al. 2009, Astrophysical Journal, 705, 1099

Auger, M. W., Treu, T., Bolton, A. S., et al. 2010, Astrophysical Journal, 724, 511

Baer, H., Choi, K.-Y., Kim, J. E., & Roszkowski, L. 2015, Physics Reports, 555, 1

Barkana, R. & Loeb, A. 2001, Physics Reports, 349, 125

Barnabè, M., Nipoti, C., Koopmans, L. V. E., Vegetti, S., & Ciotti, L. 2009, MNRAS, 393, 1114

Bartelmann, M. & Schneider, P. 2001, Physics Reports, 340, 291

Bayer, D., Chatterjee, S., Koopmans, L. V. E., et al. 2018, ArXiv e-prints

Bernabei, R., Belli, P., Bussolotti, A., et al. 2008, Nuclear Instruments and Methods in Physics Research A, 592, 297

Blanc, G. A., Adams, J. J., Gebhardt, K., et al. 2011, Astrophysical Journal, 736, 31

Bolton, A. S., Brownstein, J. R., Kochanek, C. S., et al. 2012, Astrophysical Journal, 757, 82

Bolton, A. S., Burles, S., Koopmans, L. V. E., et al. 2008, Astrophysical Journal, 682, 964

Bolton, A. S., Burles, S., Koopmans, L. V. E., Treu, T., & Moustakas, L. A. 2006, Astrophysical Journal, 638, 703

Bond, I. A., Udalski, A., Jaroszyński, M., et al. 2004, Astrophysical Journal Letters, 606, L155

Bond, N. A., Gawiser, E., Guaita, L., et al. 2012, Astrophysical Journal, 753, 95

Bosma, A. 1981, Astronomical Journal, 86, 1825

Bouwens, R. J., Illingworth, G. D., Franx, M., et al. 2009, Astrophysical Journal, 705, 936

Boyarsky, A., Franse, J., Iakubovskyi, D., & Ruchayskiy, O. 2015, Physical Review Letters, 115, 161301

Boyarsky, A., Iakubovskyi, D., & Ruchayskiy, O. 2012, Physics of the Dark Universe, 1, 136

Boyarsky, A., Ruchayskiy, O., Iakubovskyi, D., & Franse, J. 2014, Physical Review Letters, 113, 251301

Boyarsky, A., Ruchayskiy, O., & Shaposhnikov, M. 2009, Annual Review of Nuclear and Particle Science, 59, 191

Bradač, M., Schneider, P., Steinmetz, M., et al. 2002, Astronomy and Astrophysics, 388, 373

Broadhurst, T. 1995, arXiv e-prints, astro

Bulbul, E., Markevitch, M., Foster, A., et al. 2014, The Astrophysical Journal, 789, 13

Calzetti, D., Armus, L., Bohlin, R. C., et al. 2000, Astrophysical Journal, 533, 682

Capaccioli, M. 1989, in World of Galaxies (Le Monde des Galaxies), ed. H. G. Corwin, Jr. & L. Bottinelli, 208–227

CDMS Collaboration, Agnese, R., Ahmed, Z., et al. 2013, arXiv e-prints, arXiv:1304.4279

Chen, J., Kravtsov, A. V., & Keeton, C. R. 2003, Astrophysical Journal, 592, 24

Chiba, M. 2002, Astrophysical Journal, 565, 17

Christensen, L., Laursen, P., Richard, J., et al. 2012, MNRAS, 427, 1973

Ciardi, B. & Ferrara, A. 2005, Space Science Reviews, 116, 625

Clowe, D., Bradač, M., Gonzalez, A. H., et al. 2006, Astrophysical Journal, 648, L109

Collett, T. E. 2015, Astrophysical Journal, 811, 20

Cornachione, M. A., Bolton, A. S., Shu, Y., et al. 2018, Astrophysical Journal, 853, 148

Dalal, N. & Kochanek, C. S. 2002a, Astrophysical Journal, 572, 25

Dalal, N. & Kochanek, C. S. 2002b, Astrophysical Journal, 572, 25

Davis, M., Huchra, J., Latham, D. W., & Tonry, J. 1982, Astrophysical Journal, 253, 423

de Jong, J. T. A., Verdoes Kleijn, G. A., Boxhoorn, D. R., et al. 2015, Astronomy and Astrophysics, 582, A62

Despali, G., Giocoli, C., Angulo, R. E., et al. 2016, MNRAS, 456, 2486

Despali, G., Vegetti, S., White, S. D. M., Giocoli, C., & van den Bosch, F. C. 2018, MNRAS, 475, 5424

Duffy, A. R., Schaye, J., Kay, S. T., & Dalla Vecchia, C. 2008, MNRAS, 390, L64

Einstein, A. 1916, Annalen der Physik, 354, 769

Einstein, A. 1936, Science, 84, 506

Eisenstein, D. J., Zehavi, I., Hogg, D. W., et al. 2005, Astrophysical Journal, 633, 560

Erb, D. K., Pettini, M., Steidel, C. C., et al. 2016, Astrophysical Journal, 830, 52

Erb, D. K., Steidel, C. C., Trainor, R. F., et al. 2014, Astrophysical Journal, 795, 33

Feroz, F., Hobson, M. P., Cameron, E., & Pettitt, A. N. 2013, ArXiv e-prints

Fields, B. D. 2011, Annual Review of Nuclear and Particle Science, 61, 47

Frenk, C. S. & White, S. D. M. 2012, Annalen der Physik, 524, 507

Furlanetto, S. R. & Oh, S. P. 2016, MNRAS, 457, 1813

Gaskins, J. M. 2016, Contemporary Physics, 57, 496

Gawiser, E., van Dokkum, P. G., Gronwall, C., et al. 2006, Astrophysical Journal Letters, 642, L13

Gilman, D., Agnello, A., Treu, T., Keeton, C. R., & Nierenberg, A. M. 2017, MNRAS, 467, 3970

Gilman, D., Birrer, S., Treu, T., Nierenberg, A., & Benson, A. 2019, arXiv e-prints, arXiv:1901.11031

Giocoli, C., Meneghetti, M., Metcalf, R. B., Ettori, S., & Moscardini, L. 2014, Monthly Notices of the Royal Astronomical Society, 440, 1899

Gomer, M. R. & Williams, L. L. R. 2018, Monthly Notices of the Royal Astronomical Society, 475, 1987

Gronke, M. & Dijkstra, M. 2014, MNRAS, 444, 1095

Guaita, L., Gawiser, E., Padilla, N., et al. 2010, Astrophysical Journal, 714, 255

Hagen, A., Zeimann, G. R., Behrens, C., et al. 2016, Astrophysical Journal, 817, 79

Hainline, K. N., Shapley, A. E., Kornei, K. A., et al. 2009, Astrophysical Journal, 701, 52

Harvey, D., Massey, R., Kitching, T., Taylor, A., & Tittley, E. 2015, Science, 347, 1462

Hashimoto, T., Garel, T., Guiderdoni, B., et al. 2017, A & A, 608, A10

He, Q., Li, R., Lim, S., et al. 2017, ArXiv e-prints

Hezaveh, Y. D., Dalal, N., Marrone, D. P., et al. 2016, Astrophysical Journal, 823, 37

Hoekstra, H., Mahdavi, A., Babul, A., & Bildfell, C. 2012, MNRAS, 427, 1298

Horiuchi, S., Humphrey, P. J., Oñorbe, J., et al. 2014, Physical Review D, 89, 025017

Hsueh, J.-W., Despali, G., Vegetti, S., et al. 2018, MNRAS, 475, 2438

Hsueh, J.-W., Enzi, W., Vegetti, S., et al. 2019, arXiv e-prints, arXiv:1905.04182

Hsueh, J.-W., Fassnacht, C. D., Vegetti, S., et al. 2016, MNRAS, 463, L51

Hsueh, J.-W., Oldham, L., Spingola, C., et al. 2017, MNRAS, 469, 3713

Inoue, K. T. & Takahashi, R. 2012, Monthly Notices of the Royal Astronomical Society, 426, 2978

Iršič, V., Viel, M., Haehnelt, M. G., et al. 2017, Physical Review D, 96, 023522

Kahlhoefer, F. 2017, International Journal of Modern Physics A, 32, 1730006

Kahn, F. D. & Woltjer, L. 1959, Astrophysical Journal, 130, 705

Kobayashi, M. A. R., Murata, K. L., Koekemoer, A. M., et al. 2016, Astrophysical Journal, 819, 25

Kochanek, C. S. & Dalal, N. 2004, Astrophysical Joournal, 610, 69

Koopmans, L. V. E. 2005, MNRAS, 363, 1136

Koopmans, L. V. E., Bolton, A., Treu, T., et al. 2009, Astrophysical Journal Letters, 703, L51

Koopmans, L. V. E., Treu, T., Bolton, A. S., Burles, S., & Moustakas, L. A. 2006, The Astrophysical Journal, 649, 599

Kusakabe, H., Shimasaku, K., Nakajima, K., & Ouchi, M. 2015, Astrophysical Journal Letters, 800, L29

Lagattuta, D. J., Vegetti, S., Fassnacht, C. D., et al. 2012, MNRAS, 424, 2800

Law, D. R., Steidel, C. C., Shapley, A. E., et al. 2012, Astrophysical Journal, 759, 29

Leclercq, F., Bacon, R., Wisotzki, L., et al. 2017, A & A, 608, A8

Leethochawalit, N., Jones, T. A., Ellis, R. S., et al. 2016, Astrophysical Journal, 820, 84

Leitherer, C. & Heckman, T. M. 1995, Astrophysical Journals, 96, 9

Li, R., Frenk, C. S., Cole, S., et al. 2016, Monthly Notices of the Royal Astronomical Society, 460, 363

Li, R., Frenk, C. S., Cole, S., Wang, Q., & Gao, L. 2017, MNRAS, 468, 1426

Lovell, M. R., Bose, S., Boyarsky, A., et al. 2016, MNRAS, 461, 60

Lovell, M. R., Bose, S., Boyarsky, A., et al. 2017a, MNRAS, 468, 4285

Lovell, M. R., Frenk, C. S., Eke, V. R., et al. 2014, MNRAS, 439, 300

Lovell, M. R., Gonzalez-Perez, V., Bose, S., et al. 2017b, MNRAS, 468, 2836

LSST Science Collaboration, Abell, P. A., Allison, J., et al. 2009, arXiv e-prints

Madau, P. & Dickinson, M. 2014, Annual Review of Astronomy and Astrophysics, 52, 415

Malhotra, S., Rhoads, J. E., Finkelstein, S. L., et al. 2012, Astrophysical Journal Letters, 750, L36

Mao, S. & Paczynski, B. 1991, Astrophysical Journal, Letters, 374, L37

Mao, S. & Schneider, P. 1998, MNRAS, 295, 587

Matthee, J., Sobral, D., Oteo, I., et al. 2016, MNRAS, 458, 449

McKean, J., Jackson, N., Vegetti, S., et al. 2015, in Advancing Astrophysics with the Square Kilometre Array (AASKA14), 84

McKean, J. P., Koopmans, L. V. E., Flack, C. E., et al. 2007, MNRAS, 378, 109

Meneghetti, M., Rasia, E., Merten, J., et al. 2010, Astronomy and Astrophysics, 514, A93

Metcalf, R. B. 2005, The Astrophysical Journal, 622, 72

Minor, Q. E., Kaplinghat, M., & Li, N. 2017, Astrophysical Journal, 845, 118

Möller, O., Hewett, P., & Blain, A. W. 2003, MNRAS, 345, 1

Momose, R., Ouchi, M., Nakajima, K., et al. 2014, MNRAS, 442, 110

Nakajima, K., Fletcher, T., Ellis, R. S., Robertson, B. E., & Iwata, I. 2018, MNRAS, 477, 2098

Nakajima, K., Ouchi, M., Shimasaku, K., et al. 2012, Astrophysical Journal, 745, 12

Navarro, J. F., Frenk, C. S., & White, S. D. M. 1996, Astrophysical Journal, 462, 563

Navarro, J. F., Frenk, C. S., & White, S. D. M. 1997, Astrophysical Journal, 490, 493

Nierenberg, A. M., Treu, T., Wright, S. A., Fassnacht, C. D., & Auger, M. W. 2014, Monthly Notices of the Royal Astronomical Society, 442, 2434

Nightingale, J. W., Dye, S., & Massey, R. J. 2018, MNRAS, 478, 4738

Nikolaus, K. S. & Hundertmark, M. 2018, arXiv e-prints, arXiv:1804.10136

Nilles, H. 1984, Physics Reports, 110, 1

Nilsson, K. K., Tapken, C., Møller, P., et al. 2009, A & A, 498, 13

Oguri, M. & Marshall, P. J. 2010, MNRAS, 405, 2579

Oldham, L. J. & Auger, M. W. 2018, MNRAS, 476, 133

Oyarzún, G. A., Blanc, G. A., González, V., Mateo, M., & Bailey, III, J. I. 2017, Astrophysical Journal, 843, 133

Patrício, V., Richard, J., Verhamme, A., et al. 2016, MNRAS, 456, 4191

Paulino-Afonso, A., Sobral, D., Ribeiro, B., et al. 2018, MNRAS, 476, 5479

Percival, W. J., Baugh, C. M., Bland-Hawthorn, J., et al. 2001, Monthly Notices of the Royal Astronomical Society, 327, 1297

Planck Collaboration, Ade, P. A. R., Aghanim, N., et al. 2016, A & A, 594, A13

Planck Collaboration, Aghanim, N., Akrami, Y., et al. 2018, arXiv e-prints, arXiv:1807.06209

Planck Collaboration, Aghanim, N., Akrami, Y., et al. 2017, A & A, 607, A95

Postman, M., Coe, D., Benítez, N., et al. 2012, Astrophysical Journal Supplement, 199, 25

Quadri, R., Möller, O., & Natarajan, P. 2003, The Astrophysical Journal, 597, 659

Rau, S., Vegetti, S., & White, S. D. M. 2014, MNRAS, 443, 957

Rhoads, J. E., Malhotra, S., Allam, S., et al. 2014, Astrophysical Journal, 787, 8

Ringwald, A. 2016, in Proceedings of the Neutrino Oscillation Workshop (NOW2016). 4 - 11 September, 2016. Otranto (Lecce, Italy)., 81

Ritondale, E., Auger, M. W., Vegetti, S., & McKean, J. P. 2019a, MNRAS, 482, 4744

Ritondale, E., Vegetti, S., Despali, G., et al. 2019b, MNRAS, 485, 2179

Rivera-Thorsen, T. E., Hayes, M., Östlin, G., et al. 2015, Astrophysical Journal, 805, 14

Rizzo, F., Vegetti, S., Fraternali, F., & Di Teodoro, E. 2018, MNRAS, 481, 5606

Robles, V. H., Bullock, J. S., Elbert, O. D., et al. 2017, MNRAS, 472, 2945

Roszkowski, L., Sessolo, E. M., & Trojanowski, S. 2018, Reports on Progress in Physics, 81, 066201

Rubin, V. C., Burstein, D., Ford, Jr., W. K., & Thonnard, N. 1985, Astrophysical Journal, 289, 81

Rubin, V. C., Ford, Jr., W. K., & Thonnard, N. 1978, Astrophysical Journal Letters, 225, L107

Ruff, A. J., Gavazzi, R., Marshall, P. J., et al. 2011, Astrophysical Journal, 727, 96

Saha, P. & Williams, L. L. R. 2004, The Astronomical Journal, 127, 2604

Schneider, A., Smith, R. E., Macciò, A. V., & Moore, B. 2012, MNRAS, 424, 684

Schneider, P. 2005, arXiv e-prints, astro

Servant, G. 2015, Modern Physics Letters A, 30, 1540011

Shaposhnikov, M. 2008, in Journal of Physics Conference Series, Vol. 136

Sheth, R. K. & Tormen, G. 1999, MNRAS, 308, 119

Shi, X. & Fuller, G. M. 1999, Physical Review Letters, 82, 2832

Shibuya, T., Ouchi, M., Nakajima, K., et al. 2014, Astrophysical Journal, 788, 74

Shimakawa, R., Kodama, T., Shibuya, T., et al. 2017, MNRAS, 468, 1123

Shu, Y., Bolton, A. S., Kochanek, C. S., et al. 2016a, Astrophysical Journal, 824, 86

Shu, Y., Bolton, A. S., Mao, S., et al. 2016b, Astrophysical Journal, 833, 264

Smith, B. M., Windhorst, R. A., Jansen, R. A., et al. 2018, Astrophysical Journal, 853, 191

Sonnenfeld, A., Treu, T., Gavazzi, R., et al. 2013, Astrophysical Journal, 777, 98

Spingola, C., McKean, J. P., Auger, M. W., et al. 2018, MNRAS, 478, 4816

Spingola, C., McKean, J. P., Vegetti, S., et al. 2019, arXiv e-prints, arXiv:1905.06363

Springel, V. 2005, MNRAS, 364, 1105

Springel, V., Wang, J., Vogelsberger, M., et al. 2008, MNRAS, 391, 1685

Stark, D. P., Auger, M., Belokurov, V., et al. 2013, MNRAS, 436, 1040

Steffen, F. D. 2006, Journal of Cosmology and Astro-Particle Physics, 2006, 001

Stoughton, C., Lupton, R. H., Bernardi, M., et al. 2002, Astrophysical Journal, 123, 485

Suyu, S. H., Bonvin, V., Courbin, F., et al. 2017, MNRAS, 468, 2590

Suyu, S. H., Chang, T.-C., Courbin, F., & Okumura, T. 2018, Space Science Reviews, 214, 91

Suyu, S. H., Marshall, P. J., Hobson, M. P., & Blandford, R. D. 2006, MNRAS, 371, 983

Swinbank, A. M., Webb, T. M., Richard, J., et al. 2009, MNRAS, 400, 1121

Thompson, D. J., Bertsch, D. L., Fichtel, C. E., et al. 1993, Astrophysical Journal Supplement, 86, 629

Trainor, R. F., Steidel, C. C., Strom, A. L., & Rudie, G. C. 2015, Astrophysical Journal, 809, 89

Trainor, R. F., Strom, A. L., Steidel, C. C., & Rudie, G. C. 2016, Astrophysical Journal, 832, 171

Treu, T. & Koopmans, L. V. E. 2002, ArXiv Astrophysics e-prints

Vanzella, E., de Barros, S., Vasei, K., et al. 2016, Astrophysical Journal, 825, 41

Vegetti, S., Czoske, O., & Koopmans, L. V. E. 2010a, MNRAS, 407, 225

Vegetti, S., Despali, G., Lovell, M. R., & Enzi, W. 2018, MNRAS, 481, 3661

Vegetti, S. & Koopmans, L. V. E. 2009, MNRAS, 392, 945

Vegetti, S., Koopmans, L. V. E., Auger, M. W., Treu, T., & Bolton, A. S. 2014, MNRAS, 442, 2017

Vegetti, S., Koopmans, L. V. E., Bolton, A., Treu, T., & Gavazzi, R. 2010b, MNRAS, 408, 1969

Vegetti, S., Lagattuta, D. J., McKean, J. P., et al. 2012, Nature, 481, 341

Venemans, B. P., Röttgering, H. J. A., Miley, G. K., et al. 2005, A & A, 431, 793

Verhamme, A., Dubois, Y., Blaizot, J., et al. 2012, A & A, 546, A111

Vogelsberger, M., Genel, S., Springel, V., et al. 2014, MNRAS, 444, 1518

Walsh, D., Carswell, R. F., & Weymann, R. J. 1979, Nature, 279, 381

Watson, C. R., Li, Z., & Polley, N. K. 2012, Journal of Cosmology and Astroparticle Physics, 3, 018

White, S. D. M., Frenk, C. S., & Davis, M. 1983, Astrophysical Journal Letters, 274, L1

Wisotzki, L., Bacon, R., Blaizot, J., et al. 2016, A & A, 587, A98

Xu, D., Sluse, D., Gao, L., et al. 2015, MNRAS, 447, 3189

Xu, D. D., Mao, S., Cooper, A. P., et al. 2012, MNRAS, 421, 2553

Xu, D. D., Mao, S., Cooper, A. P., et al. 2010, MNRAS, 408, 1721

Xu, D. D., Mao, S., Wang, J., et al. 2009, MNRAS, 398, 1235

Xu, Y., Yue, B., Su, M., Fan, Z., & Chen, X. 2014, Astrophysical Journal, 781, 97

Zhang, H., Abdukerim, A., Chen, W., et al. 2019, Science China Physics, Mechanics, and Astronomy, 62, 31011

Zitrin, A., Broadhurst, T., Coe, D., et al. 2011, Astrophysical Journal, 742, 117

Zwicky, F. 1933, Helvetica Physica Acta, 6, 110

Zwicky, F. 1937, Phys. Rev., 51, 290

Acknowledgements

I would first of all and anybody, thank my supervisor Simona. She has been stubborn for me when I wasn't and believed in me when I didn't. I will always be grateful to her for being the most supportive supervisor I could ever hope for. Despite our different personalities, I have loved the work we have done together, and I have a high regard for her because I genuinely think she is a great scientist. With her, I owe a huge thank you to the rest of our group, thank you Giulia, thank you, Francesca, and thank you, Devon, for helping me remove the obstacles I got stuck with and being patient when I was running into problems. A special shout out to Wolfgang who was SO kind to translate the abstract of this thesis in German, DANKE!!

They say that friends are the family you choose for yourself and it could not be truer for the amazing people I call friends and me. I met these guys while travelling for study and work and they have gifted me with the best luggage I could ever hope to bring back with me: love and friendship. First of all, thank you Shreeya for always finding a way to come and see my crazy family and me, you know you are a second daughter to mama and papa and a sister for me. I always think of you as the Sun, for the shiny happiness and joy you bring whenever you are around, and I am sure you will never let this change. Yì qióng, so far but so close! Thank you for always making me laugh and ordering me to sleep even if we are 8950 kilometres apart. You have been precious, always bringing a smile on my face with your coffee vegetable and "I am fuuuuuuul!". Kate, I miss our every-day coffees at the roof of the Kevin building so much, but I am grateful that we still get the chance to have one from time to time.
How could I not mention my mathematician family? You guys are the craziest and most amazing people I have ever met in my life. Mavi, Nicole and Anna, I would like to thank especially you, for supporting me in very tough times. It is also thanks to you if I made it until now. Zio Baffo, Zio Puddu, Fabio, Annaré, Davidello, Patrick, thank you for sharing with me the craziness and the fun in these years! You all guys have been my "chiave di volta"!
Davide, I could not be happier to have you back. I had forgotten how easy and spontaneous a friendship can be, and you just reminded me that everything is simple when you genuinely care for someone. Thank you for supporting me in this very stressful time and motivating me together with our mad and clumsy Sid. It is a pleasure always running after you and getting a reply after ages!
Munich has really given me a lot. Despite the mixed feelings I have for this city and Germany in general, how couldn't I be IMMENSELY GRATEFUL for my Bonone? Giulia, Elena, Jessica, Marisa, Deborah and Maria. Thank you for making Munich my little Italy and a place I am

always happy to come back to because I know my Bone are there waiting for their Ammamma. And also a huge thank you to my lovely Caterina and Linda. I guess you are the only people with whom I need to set up doodles to find a date to meet but, it is totally worth it! You are another piece of Munich I will always keep in my heart.
I really have to mention you separately, Giulia. I know I have found a soul sister in you, someone I will travel anywhere in the world to see, and that will always be one of my closest friends, no matter distance and time. I am sure I will never lose you, and I guess you know that you and the Belve have been the starting point for a new life for me. They won't be able to understand but Iris and Blu, I just wanted to say thank you for your unconditional and special love, me fate taglià! You three are mostly the reason why I am happy today, and I will never forget this, in the same way as I will always remember the majesty power of the Dark Mater. Also, I am looking forward to starting off with our Cats-café and bridal gown shop in Firenze. Not to mention Grandezza, one day it is gonna be ours! E poi.. Come dici tu, eh ma poi se vai da sola, senza di me come fai?

E ora passiamo ai ringraziamenti in italiano perché non verrebbero altrimenti capiti (o non avrebbero senso in inglese).
Quando ho deciso di cominciare il dottorato, mi sono lasciata convincere da qualcuno che ci credeva più di me che effettivamente, avrei potuto farcela. Ora che ci sono quasi riuscita, è difficile per me non esprimere la più profonda gratitudine e il più grande affetto per chi non è più accanto a me tutti i giorni ma sarà sempre nel mio cuore. Un grazie altrttanto grande va a una coppia meravigliosa che per me rimane uno degli esempi di amore più profondo e solido che conosca. È anche un po' frutto del vostro incoraggiamento se oggi sono qui.
The beautiful people, so anni che mi rompete le scatole, soprattutto tu Panighetti, visto che hai preteso che il tuo nome fosse scritto qui. A parte gli scherzi, anche se ci vediamo poco vi sono grata per ricordarvi sempre di me, anche quando io me ne scordo, tipo ora che io scrivo i ringraziamenti e voi mi fate coraggio.. Grazie veciiiiii! Erica ed Elisa, siete preziose per me, sappiatelo.
Erica e Radu, grazie per avermi dato supporto e convinzione quando sono stata in dubbio durante questo percorso. Erica in particolare, siamo lontane chilometri ma non penso che siamo mai state cosi' vicine. Grazie per pensare sempre a me ed essere sempre positiva e dolce, e pure paziente per quante cose mi scordo. Non penso tu sappia quanto significhi per me averti come amica, ma so che è una mia responsabilità perchè non lo dimostro mai abbastanza. Ti voglio un mondo di bene shorellina hippie, grazie per rendere questa distanza inesistente. Ci sei sempre stata e so che sempre ci sarai <3
Lo scudo dell'ignoranza, ragazzi occupate nel mio cuore un posto speciale. In particolare voi Giulia, Federico e Giorgio.. Come faccio a spiegarvi che senza di voi la mia adolescenza e la mia giovinezza sarebbe stata infinitamente più triste? Si, Fede, la GIOVINEZZA perchè sono ancora giovane IO! Fede e Gio, non so quante volte mi avete fatto piangere dal ridere e non riesco nemmeno a pensare a tutto quello che abbiamo vissuto assieme perchè siete come fratelli e siete essenziali nello stesso modo. Siamo cresciuti insieme e non riesco nemmeno a immaginarmi una vita senza Urriu! Grazie per esserci stati nei momenti più brutti, ognuno a suo modo, e soprattutto per esserci sempre nei più belli (se non venite a Monaco per la discussione vi spacco le gambe). Grazie per l'Arcadia quando avevo 15 anni, grazie per avermi sempre protetta dalla mia fissa

per uomini di dubbia maturità (o per lo meno per averci tentato) e grazie per aver rischiato risse per passare una sera con me. Grazie per esservi sorbiti viaggi, concerti, trentini e tedeschi per venire a passare un po' di tempo assieme e grazie anche per tutte le polemiche e le discussioni perchè penso che se ancora non ci siamo mandati a quel paese.. è solo perché ci vogliamo un MUCCHIO di bene. Giulia.. Non so nemmeno da dove cominciare. Non ricordo un singolo momento della mia vita che tu non abbia vissuto con me in tutto e per tutto. Secondo me se cerco sul dizionario (sai che io ne ho uno tutto mio), come definizione di migliore amica trovo solo il tuo nome. Se ripenso alle canne ascetiche, all'omino, a Bombax e Trombax, al patacchio, alle varie stupidere, alle stelline appese in classe, i ceri accesi alla madonna da atea quale sei perchè non capivi la matematica, ai diari della comix che sono più delle enciclopedie, ai Red Hot, a Trento e al convitto delle suore in cui tu non potevi entrare, alla sera prima che partissi per Glasgow e al sole e alla luna, ai selfie orribili (ma veramente orribili), al caffelatte, alle birre io e te al lago, alle sorprese che ti ho fatto e agli infarti che ti ho fatto prendere, alle ore infinite di chiacchierate anche telefoniche.. In tutto questo siamo cresciute e ora tu hai una meraviglia di bambina che e' stupenda e che porta gioia nel cuore ovunque va e io mi sto dottorando. Siamo diventate donne intanto e senza accorgercene e a chilometri di distanza abbiamo lasciato crescere questa amicizia che ora io non riesco a vedere se non come una sorellanza. Sei fondamentale e so che se c'è una costante nella mia vita, quella sei tu. Grazie di tutto quello che mi hai dato e che ancora mi darai <3

Infine, il ringraziamento più grande va alla mia famiglia, a famiglia du Vettappruzz (pa, l'ho scritto bene?) e con loro, anche e soprattutto all'intramontabile nonno Pietro. Si è girato Brescia e la Germania e noi tutti, io in particolare, stiamo seguendo il suo esempio. Siamo Ritondale e siamo tutti 'spiert grazie a lui. Se non fosse per le orme che voi avete lasciato e che io mi sforzo di percorrere altrettanto bene, non sarei mai arrivata qui. Grazie per avermi indicato sempre la strada, la migliore che potessi seguire e per la fiducia smisurata che avete sempre dimostrato di avere in me e che non è mai vacillata, nemmeno per un istante. Il vostro amore incondizionato e il vostro supporto è quanto di più prezioso una figlia o una sorella possano chiedere. Ciò che rende il vostro amore speciale è che non è scontato, ma è spontaneo, voluto e coltivato, giorno per giorno, come si coltiva un giardino prezioso. Quello che sono, umanamente, prima che professionalmente, lo devo a voi mamma, papà, Pier e Chiara. Le opportunità che mi avete offerto non sono da tutti e vi sono immensamente riconoscente. E voi due trappetani, so che sono insopportabile, nelle nuvole, sclerata e a volte anche parecchio disorganizzata, quindi volevo ringraziarvi per l'enorme pazienza che portate con me e anche dirvi grazie perchè so che nonostante questo, mi adorate. Siete la mia ragione di vita, i miei primi amori e il mio esempio quotidiano. GRAZIE!

Ora che questi ringraziamenti sono diventati quasi più lunghi dell'abstract di questa tesi, volevo semplicemente dire che sono infinitamente grata a chiunque, chi con un piccolo contributo, chi con uno grande, mi abbia aiutato ad arrivare fino a qui. Sono una ragazza fortunata ma la fortuna non è soltanto un dono, si costruisce circondandosi d'amore e di bellezza d'animo delle persone. Non è un caso che in tedesco per esprimere i concetti di felicità e fortuna si usi la stessa parola, una è parte fondamentale dell'altra e in molti casi coincidono. E io posso veramente dire di sentirmi avvolta dalla fortuna e dalla felicità.